
Study of populations of low-mass X-ray binaries in elliptical galaxies

Zhongli Zhang



München 2012

Study of populations of low-mass X-ray binaries in elliptical galaxies

Zhongli Zhang

Dissertation
an der Fakultät für Physik
der Ludwig-Maximilians-Universität
München

vorgelegt von
Zhongli Zhang
aus Wuhan, China

München, den 31. 01. 2012

Erstgutachter: Prof. Dr. Rashid Sunyaev
Zweitgutachter: Prof. Dr. Joachim Trümper
Tag der mündlichen Prüfung: 13. 01. 2012

Summary

The aim of this thesis is to study the environmental dependence of populations of low-mass X-ray binaries (LMXBs) in early-type galaxies. The dissertation is mainly based on archival data of the *Chandra* observatory whose unprecedented sub-arcsec angular resolution made it possible to resolve individual compact sources in nearby galaxies. The *Chandra* data is complemented by the infrared data of the *Spitzer* observatory as well as by the results of the Hubble Space Telescope and ground based optical observations. The dissertation investigates the dependence of LMXB populations on the stellar density, velocity dispersion and the age of the stellar population.

To investigate the LMXB dependence on the stellar density and velocity dispersion, we studied different sub populations of low-mass X-ray binaries – dynamically formed systems in globular clusters and in the nucleus of M31, and presumably primordial X-ray binaries in the fields of galaxies. Our sample includes seven nearby galaxies (M31, Maffei1, Centaurus A, M81, NGC 3379, NGC 4697 and NGC 4278) and the Milky Way, which together provide relatively uniform coverage down to the unprecedented luminosity limit of 10^{35} erg/s. In total we have detected 185 LMXBs associated with globular clusters, 35 X-ray sources in the nucleus of M31 and 998 field sources of which ~ 365 are expected to be background active galactic nuclei. We combine these data, taking special care of accurate incompleteness correction and removal of background contamination, and produce luminosity distributions of X-ray binaries in different environments to far greater accuracy than have been previously obtained. We found that the luminosity distributions of globular cluster and field LMXBs differ throughout the entire luminosity range. The fraction of faint ($\log(L_X) < 37$) sources in globular clusters is ~ 4 times smaller than in the field population. This may present a challenge for the models suggesting that the entire LMXB population was formed dynamically in globular clusters and then expelled to the field due to dynamical interactions or as globular clusters dissolve. The luminosity function of dynamically formed sources in the nucleus of M31 is similar to that of globular cluster sources at the faint end but differs at the bright end, that the M31 nucleus hosting significantly fewer bright sources than globular clusters (and field population). The difference between their luminosity distributions is likely caused by the factor of $\sim 10 - 20$ difference in stellar velocities in globular clusters and galactic nuclei, which leads to different dynamical formation channels.

In order to investigate the LMXB dependence on the stellar age we collected a sample of 20 nearby massive E/S0 galaxies covering a broad range of stellar ages from ~ 1 to > 10 Gyrs. To produce a statistically meaningful sample of

X-ray binaries in each galaxy, we required the point source detection sensitivity of *Chandra* data better than $5 \cdot 10^{37}$ erg/s. We found statistically significant correlation of the specific frequency of LMXBs (number per unit stellar mass) with the age of the host galaxy and its globular cluster content. Overall, older galaxies tend to have more X-ray binaries per unit stellar mass than the younger ones. This can be explained as a combined effect of two factors. On one hand, there appears to be an intrinsic correlation of the specific number of low-mass X-ray binaries in the field with the age of the stellar population. On the other hand, the older galaxies tend to have richer globular cluster population and therefore a larger number of dynamically formed X-ray sources associated with them. We also found a significant difference in the luminosity functions of low-mass X-ray binaries in younger and older galaxies, with the former having a flatter luminosity distribution and hosting more bright sources. This behavior is unrelated to the difference between luminosity distributions of the globular cluster and field sources and reflects the intrinsic age dependence of the LMXB populations.

These results are discussed in the context of the theory of binary evolution. As an important product of this investigation we produced high quality luminosity distributions of low-mass X-ray binaries in different stellar environments in order to provide input for verification of population synthesis models.

Zusammenfassung

Ziel dieser Arbeit ist es, die Abhängigkeit von Populationen von Röntgendoppelsternen mit Begleitsternen geringer Masse (engl. *low-mass X-ray binaries*, LMXBs) von ihrer Umgebung in Galaxien frühen Hubble-Typs zu untersuchen. Dies geschieht hier vorwiegend auf Grundlage von Archivdaten des Chandra-Röntgenobservatoriums, dessen unerreicht hohe Winkelauflösung (unterhalb einer Bogensekunde) die Detektion einzelner kompakter Quellen in nahen Galaxien erst möglich gemacht hat. Ergänzt werden die verwendeten Chandra-Daten durch Daten des Spitzer-Observatoriums im infraroten Spektralbereich und Beobachtungen des Hubble-Weltraumteleskops und erdgebundener Teleskope im optischen Spektralbereich. In dieser Dissertation wird untersucht, wie LMXB-Populationen von der Anzahldichte und der Geschwindigkeitsdispersion der umgebenden Sterne und dem Alter der Sternpopulation abhängen.

Um die Abhängigkeit der LMXBs von der umgebenden Sternanzahldichte und Geschwindigkeitsdispersion zu studieren, wurden in dieser Arbeit verschiedene Unterpopulationen von LMXBs betrachtet. Dazu wurden dynamisch gebildete LMXBs in Kugelsternhaufen oder dem Kern von M31 mit solchen verglichen, die in weniger dichten Bereichen von Galaxien im Rahmen von Sternentwicklungsprozessen entstehen. Der verwendete Datensatz umfasst sieben Galaxien in unserer Nachbarschaft (M31, Maffei1, Centaurus A, M81, NGC 3379, NGC 4697 and NGC 4278) sowie die Milchstraße. Dieser Datensatz erlaubt eine relativ gleichmäßige Untersuchung von LMXBs bis zu einer bislang unerreichten minimalen Leuchtkraft von 10^{35} erg/s. Insgesamt wurden 185 LMXBs in Kugelsternhaufen und 35 Röntgenquellen im Kern von M31 gefunden. Weitere 998 Röntgenquellen wurden in den weniger dichten Bereichen der Galaxien unseres Referenzdatensatzes detektiert, wobei wir davon ausgehen, dass ~ 365 hiervon aktive Galaxienkerne im Hintergrund sind. Nach sorgfältigem Abzug deskosmischen Röntgenhintergrunds und einer Korrektur auf Unvollständigkeit des Datensatzes wurden alle Daten kombiniert. Daraus wurde die Helligkeitsverteilung von LMXBs in unterschiedlichen Umgebungen mit bislang unerreichter Genauigkeit abgeleitet. Wir stellen fest, dass die Leuchtkraftverteilung von LMXBs in Kugelsternhaufen und jene von LMXBs in weniger dichten Bereichen von Galaxien über die gesamte Leuchtkraft-Skala voneinander abweichen. Der Anteil dunkler ($\log L_X < 37$) Quellen in Kugelsternhaufen ist ungefähr vier mal kleiner als in den weniger dichten Bereichen der Galaxien. Dies könnte ein Problem darstellen für Modelle, die vorschlagen, dass die gesamte LMXB-Population dynamisch in Kugelsternhaufen gebildet wird und dann entweder durch dynamische Interaktionen oder durch die Auflösung von Kugelsternhaufen in die weniger dichten Bereiche der Galaxien gelangt. Die

Leuchtkraftfunktion von dynamisch im Kern von M31 gebildeten Quellen gleicht im Bereich geringer Leuchtkraft in etwa der von Kugelsternhaufen. Am hellen Ende der Verteilung hat der Kern von M31 allerdings signifikant weniger Quellen als die Kugelsternhaufen (und die Population in den weniger dichten Bereichen der Galaxien). Dieser Unterschied zwischen den Leuchtkraftverteilungen ist wahrscheinlich durch die um einen Faktor ~ 10 – 20 verschiedenen stellaren Geschwindigkeiten in Kugelsternhaufen und galaktischen Kernen begründet, was zu unterschiedlichen dynamischen Formationskanälen führt.

Für die Untersuchung der Abhängigkeit von LMXBs vom Alter der Sternpopulation haben wir einen Datensatz mit 20 nahen massereichen E/S0-Galaxien, deren Alter über einen großen Bereich von ~ 1 bis >10 Billionen Jahren verteilt sind, erstellt. Um eine statistisch aussagekräftige Anzahl an Röntgendoppelsternen für jede einzelne Galaxie zu erhalten, haben wir eine minimale Leuchtkraft von 10^{35} erg/s für die Chandra-Beobachtungen angesetzt. Wir haben eine statistisch signifikante Korrelation der spezifischen Häufigkeit von LMXBs (Anzahl pro stellare Masseneinheit) mit dem Alter der beherbergenden Galaxie und deren Anzahl an Kugelsternhaufen gefunden. Wir stellen fest, dass ältere Galaxien dazu neigen, mehr Röntgendoppelsterne pro stellarer Masseneinheit zu haben als jüngere Galaxien. Dies lässt sich als Kombination von zwei Effekten erklären. Auf der einen Seite scheint es eine intrinsische Korrelation zwischen der spezifischen Häufigkeit von LMXBs aus dem weniger dichten Bereich der Galaxie und dem Alter der Galaxie zu geben. Auf der anderen Seite scheinen ältere Galaxien mehr Kugelsternhaufen und somit eine größere Anzahl an dynamisch gebildeten Röntgenquellen zu beherbergen. Des Weiteren haben wir einen deutlichen Unterschied der Leuchtkraftfunktionen von LMXBs zwischen jungen und älteren Galaxien feststellen können, wobei erstgenannte eine flachere Verteilung der Leuchtkraft haben und mehr leuchtstarke Quellen enthalten. Dieses Verhalten spiegelt die intrinsische Abhängigkeit der LMXB-Populationen vom Alter der Galaxie wieder und steht in keinem Zusammenhang mit den unterschiedlichen Leuchtkraftfunktionen von Quellen in Kugelsternhaufen und in weniger dichten Bereichen der beherbergenden Galaxie.

Die erhaltenen Resultate werden im Bezug auf theoretische Modelle der Doppelsternentwicklung diskutiert. Ein wichtiges Ergebnis unserer Arbeit ist die Erstellung von Leuchtkraftfunktionen hoher Genauigkeit für LMXBs in unterschiedlichen stellaren Umgebungen. Diese bilden die Grundlage zur Überprüfung von Populationssynthese-Modellen.

Contents

Summary	v
Zusammenfassung	vii
1 Introduction	1
1.1 Low-mass X-ray binaries	2
1.1.1 Accretion and X-ray emission	2
1.1.2 Formation channels of LMXBs	4
1.1.3 Evolution of LMXBs	5
1.2 X-ray observations of LMXBs	5
1.2.1 <i>Chandra</i> X-ray telescope	6
1.2.2 Luminosity functions of LMXBs	7
1.2.3 LMXBs in globular clusters	8
1.2.4 A stellar mass indicator	8
1.3 Outline	9
2 X-ray and near-infrared data analysis	11
2.1 <i>Chandra</i> data analysis	11
2.1.1 Data preparation	11
2.1.2 Point source detection	11
2.1.3 Source count and luminosity	12
2.1.4 Contribution of CXB sources	12
2.1.5 X-ray incompleteness function	13
2.2 Near-infrared data and the stellar mass	14
3 LMXB dependence on the stellar density and velocity dispersion	15
3.1 Introduction	15
3.2 The sample	16
3.3 Data analysis	17
3.4 Statistics of X-ray sources	20
3.4.1 Resolved LMXBs and CXB	20
3.4.2 GC-LMXB identification	24
3.4.3 Incompleteness of GCs	26
3.4.4 The Milky Way Sources	28
3.5 XLFs of different LMXB populations	29
3.5.1 X-ray incompleteness function	29
3.5.2 Combined LF of GC-LMXBs	31

Contents

3.5.3	Combined LF of field LMXBs	32
3.5.4	LF of sources in the nucleus of M31	33
3.6	Results	35
3.7	Caveats	37
3.7.1	Incompleteness of GCs	37
3.7.2	Variability of GC-LMXBs in the Milky Way	38
3.7.3	Transient sources in M31	39
3.7.4	Multiplicity of X-ray sources in GCs	40
3.7.5	Other caveats	40
3.8	Conclusions	41
4	LMXB dependence on the stellar age	49
4.1	Introduction	49
4.2	The sample	50
4.2.1	The stellar age	53
4.2.2	The globular cluster content	55
4.3	Data analysis	55
4.3.1	Data preparation and source detection	55
4.3.2	The cosmic X-ray background sources	55
4.3.3	X-ray incompleteness correction	57
4.3.4	Near-infrared data analysis	57
4.4	The X-ray luminosity function of LMXBs	57
4.4.1	CXB contribution	57
4.4.2	Corrected luminosity functions	60
4.4.3	Young and old galaxies	63
4.4.4	Galaxies with high and low GC content	65
4.5	The nature of the luminous X-ray sources	65
4.6	The LMXB – stellar mass relation	69
4.6.1	Correlation of LMXBs with the age and the GC content . .	70
4.7	Discussion	72
5	Conclusions	75
	Bibliography	77
	Acknowledgements	82
	Curriculum Vitae	85

1 Introduction

The majority of bright X-ray sources ($\gtrsim 10^{36}$ erg/s) in galaxies are X-ray binaries powered by accretion of matter from the donor star onto the compact object – a stellar mass black hole or a neutron star, in a close binary systems.

Depending on the mass of the donor star, X-ray binaries are divided into two main categories: the high-mass X-ray binaries (HMXBs) and the low-mass X-ray binaries (LMXBs). HMXBs are predominantly powered by the stellar winds from a young massive O or B stars (in a few cases, like Cen X-3, the companion star may fill its Roche lobe), thus they are associated with late-type galaxies and star formation. LMXBs are systems in which the companion has a mass $\lesssim 1M_{\odot}$ providing material through Roche lobe (RL) overflow. They are usually found in early-type galaxies and globular clusters (GCs) with old stellar populations. Populations of X-ray binaries trace the star formation and evolution history of the host galaxy. In particular, the population of HMXBs in a galaxy scales with its star-formation rate (Grimm et al. 2003), while the population of LMXBs is proportional to its stellar mass (Gilfanov 2004).

X-ray binaries in our Galaxy were studied extensively with X-ray satellites since the first days of X-ray astronomy. An incomplete list of the orbital X-ray observatories includes *UHURU*, *ARIEL V*, *EXOSAT*, *Tenma*, *Einstein*, *Ginga*, *ASCA*, *ROSAT*, *MIR-KVANT*, *GRANAT*, and *RXTE* satellites. Thus ~ 300 sources were discovered, among which ~ 150 are LMXBs with 13 found in GCs. At earlier times the sensitivity and angular resolutions of X-ray telescope was mostly insufficient to study X-ray binaries in external galaxies. This has changed with the launch of *Einstein*, *ASCA*, and *ROSAT* observatories. Even more significant progress was made in the end of 1990s with the launch of *Chandra*, *XMM-NEWTON*, and *Suzaku* observatories. With *Chandra*, thanks to its superior angular resolution ($\sim 0.5''$) the X-ray binary systems can be resolved individually within a distance of $\sim 20 - 30$ Mpc. Thus systematic studies of populations of X-ray binaries in hundreds of nearby early- and late-type galaxies became possible and have produced large amount of data and results.

This dissertation is focusing on the populations of LMXBs in nearby galaxies. Theoretical modeling of the evolution of LMXBs is difficult, therefore observations of LMXB populations in different environments provide a valuable input for tests and calibration of the population synthesis models. In this introduction we will overview the emission mechanism, formation channels and the evolution of LMXBs, and then describe the most important recent observational results focusing on the environmental dependence of the LMXB population.

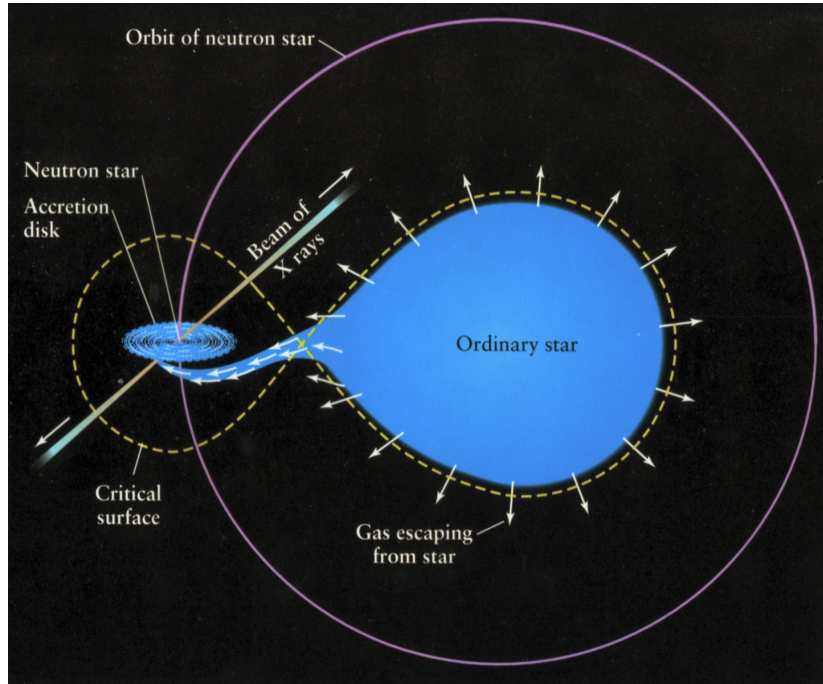


Figure 1.1: An example of the structure of an LMXB with NS accretor and a normal donor. Credit: <http://crab0.astr.nthu.edu.tw>.

1.1 Low-mass X-ray binaries

LMXBs are binary systems consisting of a neutron star (NS) or a black hole (BH) accreting matter from a low-mass ($\lesssim 1M_{\odot}$) donor star. The donor star fills its Roche lobe. The majority of LMXBs are detected in the luminosity range of $\sim 10^{35}$ to 10^{39} erg/s, with fewer sources found below 10^{37} erg/s, due to sensitivity limitations. Properties of LMXBs depend on the nature of the compact object as well as of the donor star. Besides the dichotomy between NS and BH systems, the donor star can be either a main sequence star, an evolved giant star or even a white dwarf (WD). LMXBs with WD donors are called ultra-compact X-ray binaries (UCXBs), and have apparently different formation paths from the ones with non-degenerate donors. The properties of X-ray emission depend on a number of parameters, including the masses of the two stars, the binary separation and orbital period, the type of the donor star and chemical composition of the accreted material.

1.1.1 Accretion and X-ray emission

The accretion in an LMXB with a circular orbit is set by the mechanism of Roche lobe overflow. The Roche lobe is the region of space around a star in a binary

system within which orbiting material is gravitationally bound to that star. It is the region inside a critical gravitational equipotential line, as is shown with the yellow dashed line in Fig. 1.1. Material flows from the donor to the accretor through the inner Lagrangian point L_1 (the cross point of the yellow line). In an LMXB where the mass of donor star is smaller than the accretor, the radius of a star starting the RL-overflow can be described as (Paczynski 1971):

$$\left(\frac{R_d}{a}\right)^3 = (0.46)^3 \frac{M_d}{M_d + M_a}, \quad (1.1)$$

where R_d is the radius of the donor star, a the separation of the binary, M_d the mass of the donor and M_a the mass of the accretor. The equation illustrates that the RL-overflow happens when the donor star expands, or the orbit shrinks.

The accreted material forms a disk around the compact object. The gravitational energy of the accreting material is radiated away in the form of electromagnetic radiation, which can be in the X-ray band if the temperature of the disk is high enough. This depends on the distance to the compact object and the mass accretion rate (\dot{M}). The disk will be stable above a certain \dot{M} in which case LMXBs are persistent X-ray sources. At lower \dot{M} the LMXB is observed as a transient source, emitting X-rays only during short time intervals called outbursts. This critical value of mass accretion rate can be calculated with the equation (Dubus et al. 1999):

$$\dot{M}_{crit} \simeq 3.2 \cdot 10^{-8} \left(\frac{M_a}{M_\odot}\right)^{0.5} \left(\frac{M_d}{M_\odot}\right)^{-0.2} P_{hr}^{1.4} \left(\frac{C}{5 \cdot 10^{-4}}\right)^{-0.5} M_\odot/yr, \quad (1.2)$$

where the constant C has a typical value of $5 \cdot 10^{-4}$ and P_{hr} is the orbital period in hours. We notice that \dot{M}_{crit} is higher with higher M_a , thus most of the BH binaries are transient sources. It is not very sensitive to the mass of the donor star, however very sensitive to the orbital period.

The luminosity of an accretion powered source is limited by the critical luminosity at which the radiation pressure is equal to the gravitational attraction. At higher luminosities the matter will be pushed away rather than accreted. This limiting luminosity is called the Eddington critical luminosity and for spherically symmetric accretion it is given by:

$$L_{Edd} = \frac{4\pi G M_a m_p c}{\sigma_T}, \quad (1.3)$$

where G is the gravitational constant, m_p the mass of proton, c the speed of light and σ_T the Thomson cross-section. For a $1.4 M_\odot$ NS the Eddington luminosity is $\sim 2 \cdot 10^{38}$ erg/s.

1.1.2 Formation channels of LMXBs

The formation of LMXBs occurs under special conditions which makes them rare objects. There are mainly two formation channels: the “primordial” formation through the evolution of a primordial binary system, and the “dynamical” formation through the two-body interactions of stars and binaries in the environments with high stellar density (globular clusters and galactic nuclei).

For the primordial channel, there are two scenarios of the formation of a NS (BH) - MS binary (van den Heuvel 1992): 1) the standard scenario starts with a massive star and a low-mass star in a wide binary system. The massive star evolves off the main-sequence quickly and expands. The low-mass star orbits into the expanded envelope (hence it is called the common envelope (CE)) and transfers energy into the envelope. Then the envelope is expelled, leaving a helium (HE) core and the low-mass star orbiting around each other in a tight orbit. After a while the HE star explodes as a supernova and a NS or BH forms. 2) An accretion induced collapse model with a binary consisting of two low-mass stars. The more massive star evolves off the MS first, expands and transfers mass to the less massive one. After all the hydrogen is transferred the donor turns into a WD. Thereafter the second mass transfer happens, however in the opposite direction, from the previous accretor to the previous donor. When the mass of the WD exceeds the Chandrasekhar mass limit, an accretion induced collapse may happen and an NS formed. If the binary is not destroyed when the supernova explodes, the kick velocity the NS obtained from the asymmetry of the explosion sometimes results in the binary to become tighter bounded and an LMXB forms directly. However, in most cases subsequent evolution is still required, before the donor star fills its Roche lobe. This may happen due to the expansion of the donor star, or the decay of the orbit through gravitational radiation and magnetic braking. The properties of the newly formed LMXB depend on the properties of the donor star. It can be a long-lived MS LMXB, or a short-lived RGB LMXB. In rare case the mass transfer begins only after the donor star evolved into a WD, and an ultra-compact X-ray binary is formed.

As only the binary evolution is relevant, the primordial formation channel is independent of the stellar environment. This is the case when the stellar densities are low and the binary is not influenced by the environment. However in the case of a high stellar density the chance of a multi-body interaction increases dramatically, and the dynamical formation channels start to become important. This explains the much higher specific frequency of LMXBs found in GCs (Clark 1975) and the M31 nucleus (Voss & Gilfanov 2007a). The three most important formation channels are: 1) Tidal capture of a NS by a main sequence star (Fabian et al. 1975). 2) The collision between a NS and an evolved star. The envelope of the single star is then expelled, leaving a white/brown dwarf or a helium star as the donor (Verbunt 1987). 3) An NS exchanges place with a star in a pre-existing binary (Hills 1976). Which scenario plays the dominant role depends on the local stellar density and velocity dispersion. It was found in Voss & Gilfanov (2007b)

that in GCs the exchange reactions dominates and collisions with evolved stars dominate, while in galactic nuclei, characterized by higher velocity dispersion, tidal captures of low-mass MS stars of mass $< 0.3 - 0.4M_{\odot}$ are more important.

1.1.3 Evolution of LMXBs

The evolution of LMXBs may follow different paths depending on the masses of stars and binary separation. The most important scenarios are briefly described below.

For an LMXB with a MS donor and a NS accretor, the source emits bright X-rays persistently since it starts with a relatively low critical mass transfer rate. This period lasts \sim few hundred Myrs. As the donor loses its mass, the mass transfer rate and the X-ray luminosity decreases as well. At some point the MS star runs out of thermal equilibrium, causing its radius to increase, and the mass transfer rate drops significantly. This may cause a quiescent period of the LMXB until thermal equilibrium of the star is regained. However, since the mass accretion rate is now much lower, the LMXB stays as a transient for \sim few hundred Myrs (or even few Gyrs). When the donor consumes all the hydrogen and becomes a brown dwarf with a mass under $\sim 0.1M_{\odot}$, the LMXB might be persistent again with low luminosity for another few hundred Myrs, and then fades away in a very short time. Hence the life of the LMXB is ended. With a BH accretor the evolution path is very similar to the NS accretor. However, since the critical mass transfer rate is high in the beginning, BH LMXBs are transient during most of their life time.

For LMXBs with evolved donors, which can be subgiant, red giant branch (RGB) or the asymptotic giant branch (AGB) stars, the hydrogen envelope was lost in the beginning. Due to the ~ 4 times higher ionization temperature of He and large binary separation, such systems have ~ 20 times higher critical mass accretion rate and therefore are usually not observed as persistent sources at low luminosities. For UCXBs which have WD donors, they start with a very small orbital separation and an orbital period of \sim few minutes. The X-ray luminosity is $\sim 10^{38}$ erg/s. For degenerate stars the radius of WD increases as they lose mass, thus in the following ~ 100 Myr the orbital period steadily increases to ~ 1 hour, with the X-ray luminosity decreases to $\sim 10^{36}$ erg/s. In the following evolution the UCXB becomes a transient source, which complicates its detection.

1.2 X-ray observations of LMXBs

Because of their proximity, galactic LMXBs were investigated in great detail during both active ($L_X \gtrsim 10^{36}$ erg/s) and quiescent ($\lesssim 10^{34}$ erg/s) states by various X-ray telescopes. However, there are still several factors complicating these studies. The most important one is the extinction in the galactic disk, which brings big errors in determining distances and measuring luminosities of LMXBs. On the

1 Introduction

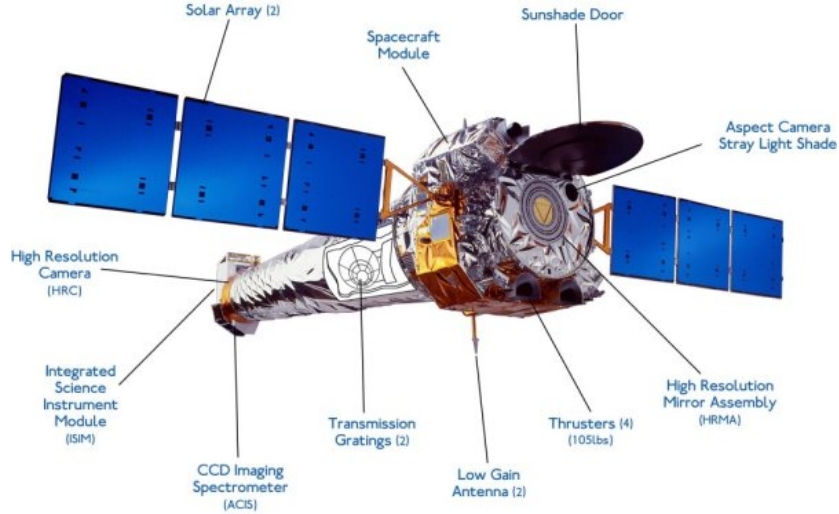


Figure 1.2: The *Chandra* X-ray Observatory and its instruments. Credit: *Chandra* X-ray center.

contrary, determination of the source luminosities is much more accurate in external galaxies, since all the sources have same Galactic absorption and are located at the same distance. Most of the nearby E/S0 galaxies fit in the field-of-view (FOV) of *Chandra*, thus all of the LMXBs can be observed at the same time, and the instantaneous luminosity function (LF) of LMXBs can be easily determined. For these reasons, the X-ray observations of nearby E/S0 galaxies are suitable for the studies of LMXB population. The main results of these studies, relevant to the topic of the dissertation are described below.

1.2.1 Chandra X-ray telescope

The *Chandra* X-ray Observatory (Fig. 1.2) was launched on the 23rd July 1999 from the Kennedy Space Center in Cape Canaveral by the Space Shuttle Columbia. It was designed to provide high resolution imaging of X-ray sources. *Chandra* was placed into an elliptical orbit to spend little time in the Earth's radiation belts, thus it allows up to 172.8 ksec of uninterrupted observing time. The onboard High Resolution Mirror Assembly (HRMA) consists of four pairs of nested Wolter type-I mirrors, with the effective area of 800 cm^2 at 0.25 keV, 400 cm^2 at 5 keV, and 100 cm^2 at 8 keV. The detectors are kept at very low temperatures ($-120 \text{ }^\circ\text{C}$) so that they are sufficiently sensitive and can record the energy of the incoming photon in an energy range of 0.3-10 keV. Its superior sub-arcsec angular resolution makes it extremely suitable for our scientific goal, that the *Chandra* archive has collected hundreds of high resolution observations of nearby E/S0 galaxies to date.

The spacecraft carries four science instruments - the High Resolution Cam-

era (HRC), the Advanced CCD Imaging Spectrometer (ACIS), the High Energy Transmission Grating (HETG) and the Low Energy Transmission Grating (LETG). Between the two imaging instruments the HRC has the highest spatial resolution but very little spectral resolution, thus it is mostly used for sky surveys. Whereas the ACIS detector has good spatial and spectral resolution, which is the primary detector for the observations in this study. As a non-dispersive imaging spectrometer, it records the location, time, and energy of every detected photon. A single chip of ACIS contains 1024×1024 pixels with an angular size of $0.492'' \times 0.492''$ per pixel, thus each chip covers an $8.4' \times 8.4'$ field of view. One 2×2 array of ACIS-I chips and one 1×6 array of ACIS-S chips are onboard. However, the more sensitive S3 chip is typically used and a galaxy at a distance of ~ 20 Mpc can normally fit in. At ~ 1.5 keV, the effective area including the quantum efficiency of the S3 chip is ~ 650 cm², and the 1σ point spread function (PSF) is $\sim 0.5''$ near the optical axis of the telescope. As a point source moves off-axis, the exposure efficiency does not change dramatically, however its PSF becomes much larger and more complex.

1.2.2 Luminosity functions of LMXBs

The luminosity function (LF, luminosity distribution) is an effective tool to study the LMXB population, which reveals their properties in various aspects. By comparing with theoretical models one can put constraints on the physical processes working in them, and give a classification of the dominant sources in certain luminosity ranges.

With the *RXTE* data of X-ray sources in the Milky Way, Grimm et al. (2002) has found that the LF of HMXBs can be well fitted by a single power-law, while the LF of LMXBs steepens towards the high luminosity end. The study of LFs in external galaxies is highly limited by the sensitivity of the observation, thus previous results of external galaxies are mostly focused on sources above few times 10^{37} erg/s. With more and more deep *Chandra* observations, the low luminosity end has been extended to $\sim 10^{36}$ erg/s in few nearest galaxies. Apart from some scatter, LFs of LMXBs were shown to have similar shape. The average XLF of LMXBs in nearby galaxies can be described by a power-law with the slope around -2.0 between few times 10^{37} and few times 10^{38} erg/s, a flatter power-law with the slope of -1.0 at the faint end, and a steeply declining function at the bright end (Gilfanov 2004; Voss & Gilfanov 2006, 2007a; Voss et al. 2009). The high luminosity break is sometimes attributed to the Eddington limit of NS binaries, while the flat power-law at the low luminosity end could be explained as due to gravitational braking driven mass transfer (e.g. in UCXBs).

Studies of LMXBs in different stellar environments revealed a possible variety of LMXB LFs. Indications have been found that the shape of LF of LMXBs in globular clusters may be different (Voss & Gilfanov 2007a; Voss et al. 2009) and that there may be a difference between younger and older populations (Kim & Fabbiano 2010).

1.2.3 LMXBs in globular clusters

It has long been known that the specific frequency of LMXBs in Galactic GCs is \sim two orders of magnitude higher than in the field (Clark 1975). With *Chandra* observations the phenomenon received further support in nearby external galaxies (e.g. Angelini et al. 2001; Sarazin et al. 2003; Minniti et al. 2004; Jordán et al. 2007b). This fact is explained as a result of dynamical formation of LMXBs in the high stellar density environment of GCs where the probability of two-body interactions is high (Fabian et al. 1975). It is different from the LMXBs in the low stellar density environment of the galaxy field, where the primordial formation is thought to be the main formation process. Thus a different LF of LMXBs in GCs and in the field was found in the Milky Way, M31 and Centaurus A, that the GC-LMXB population shows a deficit of faint sources below 10^{37} erg/s (Voss & Gilfanov 2007a; Voss et al. 2009).

In Voss & Gilfanov (2007b) the dynamical formation process of GC-LMXBs in M31 was investigated, and was compared with LMXBs in the inner bulge ($< 1'$) of M31 which were also thought to be dynamically formed (Voss & Gilfanov 2007a). Among the three main dynamical formation channels (Sect. 1.1.2), exchange reactions are potentially dominated in GCs, while collisions and tidal captures of NSs by MS stars $> 0.3M_{\odot}$ are also important. In the bulge of M31 tidal captures of low-mass MS stars ($< 0.3M_{\odot}$) dominate, where the stellar velocities are higher than in GCs by a factor of ~ 5 -10. The formation channel of collision results in some binaries with helium donor star at ~ 20 times higher critical mass accretion rate, thus they are not detected as persistent sources at low luminosities below 10^{37} erg/s. This may be the explanation of the main difference in the GC and field LMXB LFs.

1.2.4 A stellar mass indicator

Considering the primordial formation channels of LMXBs (potentially also for the dynamical channel, depending on the binary properties), the X-ray active phase is delayed by the time-scale of the nuclear evolution of the donor star and/or the binary orbit decay, which is $\sim 10^9 - 10^{10}$ yr (Verbunt & van den Heuvel 1995). This time-scale is comparable to the lifetime of the host galaxy, thus one can expect that their population is defined by the cumulative effect of the star formation episodes experienced by the galaxy, hence is proportional to its total stellar mass.

The preliminary scaling relation of LMXBs and the stellar mass was given by Grimm et al. (2002) with LMXBs in the Milky Way. Gilfanov (2004) has performed a systematic study of populations of LMXBs in 11 nearby galaxies, and have found that their cumulative number and luminosity are closely proportional to the near-infrared intensity of the host galaxy. Above 10^{37} erg/s, the total number of LMXBs estimated from their average XLF is ~ 14 per $10^{10}M_{\odot}$, and the total luminosity is $\sim 8 \cdot 10^{38}$ erg/s per $10^{10}M_{\odot}$.

A statistically significant dispersion was found from the mean value of X –

ray/M_* in Gilfanov (2004), which is $\sim 25\%$ for the luminosity and $\sim 40\%$ for the number. Neither the error induced in the colour-based correction of the K-band mass-to-light ratio, nor the variation in the morphological type of the galaxy is statistically sufficient to fully explain the dispersion.

1.3 Outline

We focused on studying properties of low-mass X-ray binaries (LMXBs) in nearby elliptical galaxies with the archival data of *Chandra* observations. The specific goal of this study is to compare formation histories and evolution of populations of LMXBs in different environments and investigate their dependence on the stellar density, velocity dispersion and the age of the stellar population.

The dissertation is structured as follows. In Chapter 2 we presented the analysis of the X-ray data from *Chandra* ACIS imaging spectrometer and the near-infrared data from 2MASS and *Spitzer*. In Chapter 3 we studied different sub populations of LMXBs – dynamically formed systems in globular clusters (GCs) and in the nucleus of M31 and presumably primordially formed X-ray binaries in the fields of galaxies. In Chapter 4 we studied the LMXB dependence on the age of the stellar population with 20 nearby E/S0 galaxies. In Chapter 5 we have our conclusions summarized.

2 X-ray and near-infrared data analysis

2.1 Chandra data analysis

2.1.1 Data preparation

We reduce the data following the standard CIAO threads ¹, always with the newest CIAO software package and calibration (CALDB). We start from ACIS *evt1* profile, using *acis_process_events* command to produce or update the time, coordinate, pulse-height, grade, and status information in the event file. Then we filter out bad grades and time intervals to create a new *evt2* file. For the aim of point source study, we do not need to exclude time intervals for background flares since the benefit of the increased exposure time outweighs the increased background. The energy range was limited to 0.5-8.0 keV. We make exposure maps with command *merge_all* in this energy range, assuming the single power-law model with $\Gamma = 1.7$ under the galactic absorption for each galaxy. Then we perform *wavdetect* to detect point sources on each observation, with the parameters listed in Sect. 2.1.2.

For galaxies with multiple observations, we correct their offsets using the point sources detected in each observation within the 4' radius of the telescope axis. The observations are then shifted using CIAO task *reproject_events*, to match the coordinate system of the reference (normally chosen as the observation with the highest exposure). The images are then combined together and re-analyzed.

The next step is to apply an absolute astrometry correction to the combined image. We use the 2MASS All-Sky Point Source catalog (Skrutskie et al. 2006) and correlate it with the brightest X-ray point sources detected from the combined image. X-ray images were shifted to give the shortest rms-distances between the X-ray sources and their 2MASS counterparts, using the command *reproject_events* again. The final corrected aspect is also applied to the exposure maps.

2.1.2 Point source detection

To detect point sources we use CIAO task *wavdetect*, which correlates the image with "Mexican Hat" wavelet functions of different scales and then searches the results for significant correlations. It is a wrapper for the tools *wtransform* and *wrecon*. We change some parameters from the default values. Most importantly, we use scales as $\sqrt{2}$ -series from 1.0 to 8.0 to give a wide range of source sizes covering the continuous change of the point spread function (PSF) from the CCD center to outwards. Sigthresh is set to 10^{-6} , yielding averagely 1 false detection per

¹<http://cxc.harvard.edu/ciao/threads/all.html>

8.2' × 8.2' area (10⁶ ACIS pixels). We also use `maxiter=10`, `iterstop=0.00001` and `bkgsthresh=0.0001` to do more iterations in the process of creating background files, and `eenergy=0.8` (the encircled fraction of source energy) to give larger areas for source parameter estimation at the risk of source merging. To obtain point source list alone we only run `wavdetect`. However to obtain the background files we have to run `wtransform` followed with `wrecon`, which consumes more time.

2.1.3 Source count and luminosity

To estimate the source counts we applied circular aperture centered on the central coordinates (output of `wavdetect`) of each source. We defined the source region as including 85% of the local point spread function (PSF) value. The PSF file was extracted by CIAO task `mkpsf` from each image, then combined together for multiple observations. The background region was defined as three times the source radius region outside of the source region. For background regions having neighboring sources overlapped, we excluded their source regions from the background regions. The source net counts (with the majority in the source region and minority in the background region) and errors were then computed by the equations from Voss & Gilfanov (2007a), which are:

$$S = \frac{C(b-d)d^{-1} - Q}{\alpha bd^{-1} - \beta} \quad (2.1)$$

and

$$\sigma_S^2 = \frac{\sigma_C^2(b-d)^2d^{-2} + \sigma_Q^2}{(\alpha bd^{-1} - \beta)^2}. \quad (2.2)$$

Here S is the total number of counts from the source, C the number of counts inside the source region, Q the number of counts in the background region, α the integral of the PSF over the source region, β the integral of the PSF over the source and background regions, b the area of the source and background regions and d is the area of the source region.

To convert the absorbed source count rates into unabsorbed luminosities in 0.5-8 keV, we assumed a power-law spectrum ($\Gamma = 1.7$) with galactic absorption at the location of the galaxy.

2.1.4 Contribution of CXB sources

The contribution of cosmic X-ray background (CXB) sources is calculated from few empirical results of the X-ray point source survey of the blank sky. We have used the $\log(N)$ - $\log(S)$ CXB distribution from Moretti et al. (2003) and Georgakakis et al. (2008).

Moretti et al. (2003) has collected ~ 3000 CXB sources combining surveys from *ROSAT*, *ASCA*, *XMM* and *Chandra*. In the 0.5-2 keV soft band which we find it covers the more complete sources in the full band, the cumulative flux distribution

can be presented as:

$$N(> S) = N_S \left[\frac{(2 \times 10^{-15})^{\alpha_{1,s}}}{S^{\alpha_{1,s}} + S_{0,s}^{\alpha_{1,s} - \alpha_{2,s}} S^{\alpha_{2,s}}} \right] \text{ cgs.} \quad (2.3)$$

where $\alpha_{1,s} = 1.82_{-0.09}^{+0.07}$, $\alpha_{2,s} = 0.60_{-0.03}^{+0.02}$, $S_{0,s} = (1.48_{-0.31}^{+0.27}) \times 10^{-14}$ erg/cm²/s and $N_S = 6150_{-1650}^{+1800}$ per deg² (errors at 68%). To convert the soft band flux to 0.5-8 keV we assume a power law spectrum with index of 1.4, The conversion factor is ~ 3.3 .

Georgakakis et al. (2008) only used *Chandra* for the survey, however a couple of deep observations have ~ 6000 sources collected, which gives a good fitting to the flux distribution:

$$N(> S) = \begin{cases} K \frac{S_{ref}}{1+\beta_1} \left(\left(\frac{S_b}{S_{ref}} \right)^{1+\beta_1} - \left(\frac{S}{S_{ref}} \right)^{1+\beta_1} \right) - \\ K' \frac{S_{ref}}{1+\beta_2} \left(\frac{S_b}{S_{ref}} \right)^{1+\beta_2}, & S < S_b, \\ -K' \frac{S_{ref}}{1+\beta_2} \left(\frac{S_X}{S_{ref}} \right)^{1+\beta_2}, & S \geq S_b, \end{cases} \quad (2.4)$$

where the normalization constants K and K' follow the relation:

$K' = K (S_b/S_{ref})^{\beta_1 - \beta_2}$, that $S_{ref} = 10^{-14}$ erg s⁻¹ cm⁻². In the 0.5-10 keV band, the best-fit parameters are: $S_b = 2.63_{-0.29}^{+0.46}$ in units of 10^{-14} erg/s, $\beta_1 = -0.58_{-0.02}^{+0.01}$, $\beta_2 = -2.48_{-0.03}^{+0.06}$, $K = 3.74 \pm 0.05$ in units of 10^{16} erg/cm²/s/deg². The conversion factor of 0.5-10 keV flux to 0.5-8 keV is 0.85.

We plotted the CXB $\log(N) - \log(S)$ distributions from the above two estimations in Fig. 2.1. They are almost consistent with each other. In the high flux end the estimation from Moretti et al. (2003) is $< 50\%$ higher than Georgakakis et al. (2008). This can possibly because of the CXB fluctuation, or the error of using soft band flux with the assumption of a certain CXB spectrum.

2.1.5 X-ray incompleteness function

The detection sensitivity of point source varies throughout the *Chandra* images. Various reasons include the non-homogeneous level of the diffuse X-ray emission in the galaxy, the deterioration of the PSF at large off-axis angles, and the non-uniform exposure of an image in which observations with different pointings are combined. To calculate the point source detection sensitivity we use the method and the code from (Voss & Gilfanov 2006), in which the detection method is inverted using the local PSF, background and exposure. The incompleteness function $K(L)$ is computed as the fraction of pixels weighted by the assumed spatial distribution of sources, in which the detection sensitivity is better (lower value) than the given luminosity. We calculated $K(L)$ separately for the CXB sources and LMXBs, since the CXB sources are assumed to have a flat distribution, while the field LMXBs are assumed to follow the K_S -band light from the 2MASS Large Galaxy Atlas (Jarrett et al. 2003). For GC-LMXBs no weighting is applied, but only pixels containing GCs were used in the calculation.

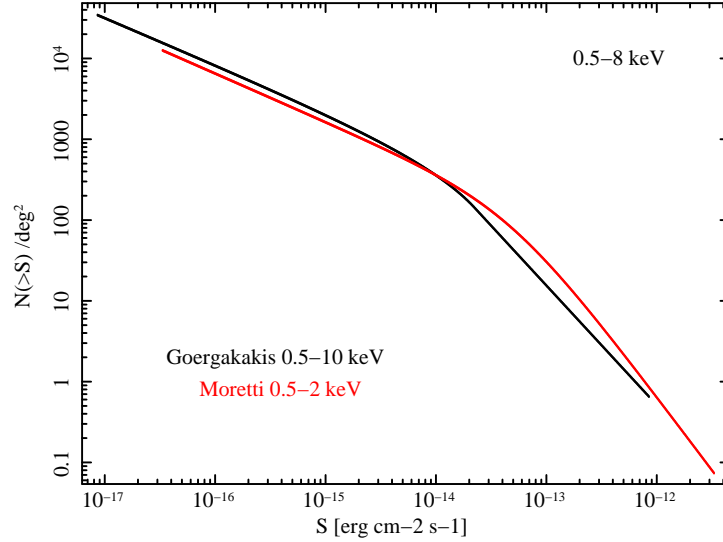


Figure 2.1: The $\log(N)$ - $\log(S)$ distribution of CXB sources in 0.5-8 keV from the conversion of Moretti et al. (2003) soft band and Georgakakis et al. (2008) full band.

2.2 Near-infrared data and the stellar mass

We calculate the stellar mass from near-infrared data, using the K_S ($2.16 \mu\text{m}$) images from the 2MASS Large Galaxy Atlas (Jarrett et al. 2003) provided by NASA/IPAC infrared science archive. We remove the contamination of bright fore/background point sources from images visually. The integrated, point source and background-subtracted count rate (S) was converted into calibrated magnitudes with $m_K(\text{mag}) = \text{KMAGZP} - 2.5 \log(S)$, where KMAGZP is the zero point magnitude for the K_S -band given in the image header. Hence the integrated K_S -band luminosity is calculated, and then converted to the stellar mass with the K_S -band mass-to-light ratios derived from Bell & de Jong (2001) with $B - V$ colors, using the equation: $\log(M_*/L_K) = -0.692 + 0.652(B - V)$.

From the 2MASS Large Galaxy Atlas most images are background subtracted. However, if the galaxy covers too large an area in the sky, the background can be possibly over subtracted. M31 is in such case. For M31 we use the IRAC/Spitzer data, and convert the $3.6 \mu\text{m}$ flux to K -band following Bogdán & Gilfanov (2010b). The conversion factor between pixel values is $C_K/C_{3.6\mu\text{m}} \sim 10.4$.

3 LMXB dependence on the stellar density and velocity dispersion

3.1 Introduction

It has long been known that there are many more low-mass X-ray binaries (LMXBs¹) per unit stellar mass in Galactic globular clusters (GCs) than in the field (Clark 1975). This fact is conventionally explained as a result of dynamical formation of LMXBs in the high stellar density environment of GCs where the probability of two-body interactions, which scales as ρ_*^2 , is high (Fabian et al. 1975). In the *Chandra* era this picture received further support from the high specific frequency of LMXBs in GCs observed in nearby external galaxies (e.g., Angelini et al. 2001; Sarazin et al. 2003; Minniti et al. 2004; Jordán et al. 2007b). Also, a significant “surplus” of LMXBs was detected in the nucleus of M31, with the spatial distribution of compact X-ray sources following the “ ρ_*^2 ” law (Voss & Gilfanov 2007a). The stellar density is low outside of GCs and the nuclear region of galaxies, with a correspondingly lower probability of stellar interaction, therefore primordial formation is thought to be the main formation process for LMXBs in the main bodies of galaxies. Their volume densities follow the distribution of stellar mass (Gilfanov 2004).

Although the above picture is attractive in its simplicity, there is a plausible alternative scenario: The entire population of LMXBs in galaxies, including those in the field may have been produced dynamically in GCs and later expelled into the field. Although the debate is still going on (White et al. 2002; Kundu et al. 2002, 2007; Irwin 2005; Juett 2005; Humphrey & Buote 2008), several strong arguments have been presented which suggest a (significant) fraction of field LMXBs formed in situ via primordial binary formation. These include the difference in spatial distributions of field LMXBs and GCs (e.g. Kundu et al. 2007) and the lack of correlation between the specific frequency of field LMXBs and that of GCs (e.g. Juett 2005). At the same time, Humphrey & Buote (2008) came to the opposite conclusion. The recently found evidence that the X-ray luminosity function (XLF) of GC-LMXBs may differ from that of field LMXBs (Voss & Gilfanov 2007a; Voss et al. 2009; Woodley et al. 2008; Kim et al. 2009) adds to this debate. Although some caveats are in order, differences in the luminosity distributions of the GC and field binaries suggest that the two sub populations of LMXBs may have different formation and/or evolution histories (Voss et al. 2009).

¹Throughout this paper we refer to objects that have been actively accreting in recent times (i.e. $\log(L_X) \gtrsim 35$) as X-ray binaries.

Differences in the luminosity distributions of LMXBs in GCs and in the field may be most obvious in the low-luminosity ($\log(L_X) \lesssim 37$) domain. Thus the reliable detection and quantitative study of any possible differences in the XLF demands special care in the treatment of incompleteness effects and the removal of the cosmic X-ray background sources (CXB). Another difficulty, of a more fundamental nature, is the statistical noise caused by the small numbers of sources. Although the majority of previous investigations seem to converge in their conclusions, with a few exceptions (e.g., Voss et al. 2009) most of these studies have marginal statistical significance. However it is difficult to achieve higher quality statistics by studying individual galaxies that host a limited number of sources. Massive ellipticals with their large GC populations could avoid this difficulty. But the long distances to the best candidates require deep X-ray observations, in the Msec range, to reach the required depth. Such data sets are not available in the *Chandra* archive. However, the potential impact of accurately determining the luminosity distributions of X-ray binaries located in different environments on our understanding of the formation and evolution of LMXBs is high. This motivated us to attempt to produce the most accurate LF of GC-LMXBs to date by combining *Chandra* data for multiple galaxies. To this end we undertook a systematic survey of nearby galaxies with sufficient numbers of LMXBs and GCs. The results of this study are reported below. The paper is structured as follows. We describe our selection criteria and resulting sample in Sect. 3.2, and our results of source detection and identification in Sect. 3.4. In Sect. 3.5 we describe the XLFs of different LMXB populations. In Sect. 3.6 we summarize our main results. Several caveats are discussed in Sect. 3.7. In the end we make our conclusion in Sect. 3.8.

3.2 The sample

In constructing the sample our goal is to provide uniform coverage over as wide a range in luminosity as possible. We aim to study sources as faint as 10^{35} erg/s. On the other hand, our goal is to have good enough statistics at the bright end where the specific frequencies of sources (per GC or per unit stellar mass) is low. Therefore our strategy is to include all galaxies with the best sensitivities achieved by *Chandra* so far and complement this with several sufficiently massive galaxies with somewhat low sensitivity in order to properly sample the high-luminosity domain. We based our selection on the list of normal galaxies available in the public *Chandra* archive. We did not exclude late-type galaxies, but in constructing the XLF of the field sources we considered only their bulges (to exclude possible contamination by HMXBs). The main selection criterion used was a detection sensitivity better than $\log(L_X) \sim 36.5 - 37$. This translates into a joint constraint on the distance to the galaxy and the exposure time of the *Chandra* observation. We also decided to exclude galaxies with stellar mass less than $10^{10} M_\odot$ because of their smaller LMXB populations and the consequently higher contamination by resolved CXB sources. Finally, we required the availability of extensive GC

data in order to reliably separate GC and field sources. Our final sample includes seven nearby galaxies (Table 3.1). In addition we also include the GC sources in the Milky Way.

M31 is the only nearby galaxy with *Chandra* sensitivity better than 10^{35} erg/s. Voss & Gilfanov (2007a) analyzed 160 ksec of *Chandra* data available at the time and found 12 LMXBs in confirmed GCs in the bulge. Since this study, an additional ~ 140 ksec of data has been collected by *Chandra* (which brings the total exposure time of the bulge to over 300 ksec), and more accurate GC data have been published (Peacock et al. 2010). We also analyzed an additional 160 ks observation of a region in the disk. Centaurus A was the target of a recent *Chandra* VLP program. With a total *Chandra* exposure time of ~ 800 ks, a detection sensitivity of 6×10^{35} erg/s has been reached in this galaxy. Voss et al. (2009) find 47 GC-LMXBs in this galaxy, so we use their source lists in our analysis. A similar detection sensitivity was reached in M81 with an exposure time of ~ 240 ks. The four other external galaxies in our sample have detection sensitivities of a few $\times 10^{36}$ erg/s and are included to increase the statistics of luminous sources. One of them, Maffei 1, is relatively small and marginally passed our mass threshold. However, it appears to be particularly rich in X-ray sources. The X-ray populations in NGC 3379, NGC 4697 and NGC 4278 have been studied previously (e.g., Kundu et al. 2007; Kim et al. 2009; Brassington et al. 2009). For these galaxies we redid the data analysis and found it to be in overall agreement with the above authors.

The Milky Way hosts 150 GCs (Harris 1996), of which 12 are known to host bright LMXBs. As all the Milky Way GCs have been surveyed in the X-rays multiple times by various instruments, we assume that our sample of GC-LMXBs is complete. We used the data from the All-Sky Monitor aboard RXTE to measure the luminosities of these sources. The advantages and shortcomings of such an approach are discussed in Sect. 3.4.4.

3.3 Data analysis

We listed the *Chandra* observations used here in Table 3.2. Data reduction follows the instructions in Sect. 2.1.1, with CIAO version 3.4 and CALDB version 3.4.1. In the procedure of correcting offsets between observations, for the disk region of M31, the observations are distributed in too wide an area to make this correction possible. For M81 and NGC 4697, the offsets between observations were insignificant thus this step was skipped. For NGC 3379, we used offsets from Brassington et al. (2008). The references of the coordinate system are marked with an asterisk in Table 3.2. After this correction, the combined images are shifted to apply an absolute astrometry, by matching with 2MASS All-Sky Point Source catalog (Skrutskie et al. 2006). These corrections are listed in Table 3.1, where dx refers to correction in the west and dy is the correction to the north. In the case of three galaxies: NGC 3379, NGC 4697, and NGC 4278, this step was skipped because

3 LMXB dependence on the stellar density and velocity dispersion

Table 3.1: The sample of external galaxies observed by *Chandra*.

Galaxy	Type	Distance (Mpc)	N_{H} ($10^{20}/\text{cm}^2$)	Study Field	M_*/L_{K} ($M_{\odot}/L_{\text{K},\odot}$)
(1)	(2)	(3)	(4)	(5)	(6)
M31	Sab	0.78 ± 0.03	6.7	$r = 11'$	0.56
	–	–	–	$15', 9', -65^\circ$	–
Cen A	S0	3.4 ± 0.4	8.6	$r = 10'$	0.76
M81	Sab	3.63 ± 0.34	4.2	$10', 5', -20^\circ$	0.70
Maffei 1	S0	3.0 ± 0.3	85.1	D25 & HST	0.73
N3379	E1	11.1	2.8	D25 & HST	0.83
N4697	E6	11.8	2.1	D25	0.77
N4278	E1-2	16.1	1.8	D25 & HST	0.79

Galaxy	M_* ($10^{10} M_{\odot}$)	Exp (ks)	Sensitivity (erg/s)	dx/dy (pixel)	Conversion (erg/cm ² /cnt)
(1)	(7)	(8)	(9)	(10)	(11)
M31	2.7	~300	4×10^{34}	+0.02/-0.37	3.4×10^{-9}
	0.60	~150	7×10^{34}	+0.11/+0.51	
Cen A	6.4	~800	6×10^{35}	– / –	3.5×10^{-9}
M81	6.0	~240	7×10^{35}	+0.10/+0.49	3.2×10^{-9}
Maffei 1	1.1	~55	3×10^{36}	+0.01/+0.29	7.7×10^{-9}
N3379	5.4	~330	4×10^{36}	– / –	3.1×10^{-9}
N4697	5.8	~200	5×10^{36}	– / –	3.0×10^{-9}
N4278	4.2	~480	6×10^{36}	– / –	3.0×10^{-9}

Columns are: (1) – Galaxy name. For M31, the first line is for the bulge region, the second line is for the region in the disk. (2) – Galaxy Type. (3) – Distance and its uncertainty (when available). References and methods are: M31 – luminosity function of red clump stars (Stanek & Garnavich 1998); Centaurus A – Cepheids (Ferrarese et al. 2007); M81 – Cepheids (Freedman et al. 1994); Maffei 1 – galaxy fundamental plane (Fingerhut et al. 2003); NGC 3379 – luminosity function of GCs (Kundu & Whitmore 2001); NGC 4697, NGC 4278 – surface brightness fluctuation (Tonry et al. 2001). (4) – Galactic column density (Dickey & Lockman 1990). (5) – The region used to study XLFs. When three numbers are given, they refer to major, minor axis and position angle. (6) – K -band mass-to-light ratios derived from Bell & de Jong (2001), with $B - V$ colors from the RC3 catalog (de Vaucouleurs et al. 1991) except for Maffei 1, which is from Buta & McCall (1983). (7) – Stellar mass in the study field, as calculated from the K -band magnitudes derived from 2MASS Large Galaxy Atlas (Jarrett et al. 2003). For M31 we used the IRAC/Spitzer data, and the $3.6 \mu\text{m}$ flux was converted to K -band following Bogdán & Gilfanov (2010b). (8) – The total exposure time of *Chandra* observations. (9) – Point source detection sensitivity estimated from the incompleteness functions in Fig. 3.5. (10) – Attitude correction. (11) – Conversion factor of *Chandra* count rate to unabsorbed X-ray flux in the 0.5-8 keV band.

we did not find enough matches.

We have only used sources located in the regions where *Chandra* data overlaps with the GC data to construct the XLFs. The sizes of these "study fields" are listed in Table 3.1, and the regions are overlaid on the X-ray images shown in Fig. 3.1.

Table 3.2: The list of *Chandra* observations analyzed in this paper. M31(1) is the bulge region and M31(2) is the disk region. The observations marked by "*" were used as the reference when combining the data.

Galaxy	Obs-ID	Instrument	Exp	Galaxy	Obs-ID	Instrument	Exp
M31(1)	0303	ACIS-I	12.01	M31(2)	0314	ACIS-S	5.15
M31(1)	0305	ACIS-I	4.18	M31(2)	1576	ACIS-I	4.95
M31(1)	0306	ACIS-I	4.18	M31(2)	1580	ACIS-S	5.13
M31(1)	0307	ACIS-I	4.17	M31(2)	1584	ACIS-I	4.97
M31(1)	0308	ACIS-I	4.06	M31(2)	2049	ACIS-S	14.76
M31(1)	0309	ACIS-S	5.16	M31(2)	2050	ACIS-S	13.21
M31(1)	0310	ACIS-S	5.14	M31(2)	2051	ACIS-S	13.80
M31(1)	0311	ACIS-I	4.96	M31(2)	2894	ACIS-I	4.72
M31(1)	0312	ACIS-I	4.73	M31(2)	2899	ACIS-I	4.97
M31(1)	*1575	ACIS-S	38.15	M31(2)	2901	ACIS-I	4.68
M31(1)	1577	ACIS-I	4.98	M31(2)	2902	ACIS-I	4.76
M31(1)	1581	ACIS-I	4.46	M31(2)	*4536	ACIS-S	54.94
M31(1)	1582	ACIS-I	4.36	M81	*0735	ACIS-S	50.56
M31(1)	1583	ACIS-I	5.00	M81	5935	ACIS-S	11.12
M31(1)	1585	ACIS-I	4.95	M81	5936	ACIS-S	11.55
M31(1)	1854	ACIS-S	4.75	M81	5937	ACIS-S	12.16
M31(1)	2895	ACIS-I	4.94	M81	5938	ACIS-S	11.96
M31(1)	2896	ACIS-I	4.97	M81	5939	ACIS-S	11.96
M31(1)	2897	ACIS-I	4.97	M81	5940	ACIS-S	12.13
M31(1)	2898	ACIS-I	4.96	M81	5941	ACIS-S	11.96
M31(1)	4360	ACIS-I	4.97	M81	5942	ACIS-S	12.11
M31(1)	4678	ACIS-I	4.87	M81	5943	ACIS-S	12.17
M31(1)	4679	ACIS-I	4.77	M81	5944	ACIS-S	11.96
M31(1)	4680	ACIS-I	5.24	M81	5945	ACIS-S	11.72
M31(1)	4681	ACIS-I	5.13	M81	5946	ACIS-S	12.17
M31(1)	4682	ACIS-I	4.93	M81	5947	ACIS-S	10.84
M31(1)	4719	ACIS-I	5.10	M81	5948	ACIS-S	12.18
M31(1)	4720	ACIS-I	5.14	M81	5949	ACIS-S	12.18
M31(1)	4721	ACIS-I	5.16	M81	9122	ACIS-S	10.04
M31(1)	4722	ACIS-I	4.87	Maffei 1	5619	ACIS-S	55.75
M31(1)	4723	ACIS-I	5.05	N3379	1587	ACIS-S	31.92
M31(1)	7064	ACIS-I	29.07	N3379	*7073	ACIS-S	85.18
M31(1)	7068	ACIS-I	9.62	N3379	7074	ACIS-S	69.95

Table 3.2: Continued.

Galaxy	Obs-ID	Instrument	Exp	Galaxy	Obs-ID	Instrument	Exp
M31(1)	7136	ACIS-I	4.96	N3379	7075	ACIS-S	84.18
M31(1)	7137	ACIS-I	4.91	N3379	7076	ACIS-S	70.14
M31(1)	7138	ACIS-I	5.11	N4697	784	ACIS-S	39.76
M31(1)	7139	ACIS-I	4.96	N4697	*4727	ACIS-S	40.45
M31(1)	7140	ACIS-I	5.12	N4697	4728	ACIS-S	36.16
M31(1)	8183	ACIS-I	4.95	N4697	4729	ACIS-S	38.61
M31(1)	8184	ACIS-I	5.18	N4697	4730	ACIS-S	40.58
M31(1)	8185	ACIS-I	4.95	N4278	4741	ACIS-S	37.94
M31(1)	8191	ACIS-I	4.95	N4278	*7077	ACIS-S	111.72
M31(1)	8192	ACIS-I	5.09	N4278	7078	ACIS-S	52.09
M31(1)	8193	ACIS-I	5.16	N4278	7079	ACIS-S	106.42
M31(1)	8194	ACIS-I	5.04	N4278	7080	ACIS-S	56.54
M31(1)	8195	ACIS-I	4.95	N4278	7081	ACIS-S	112.14
M31(2)	0313	ACIS-S	6.05				

3.4 Statistics of X-ray sources

3.4.1 Resolved LMXBs and CXB

We used “wavdetect” to detect point sources, as described in Sect. 2.1.2. The statistics of the detected sources are summarized in Tables 3.3 and 3.4. The calculation of the count rates follows Sect. 2.1.3. The luminosities of point sources were calculated assuming a power-law spectrum with $\Gamma=1.7$. Count rates in 0.5-8.0 keV band were converted into absorption corrected fluxes assuming Galactic absorption. We list the conversion factors in Table 3.1.

The estimation of the expected number of CXB sources follows the method described in Sect. 2.1.4, using the CXB $\log(N)$ - $\log(S)$ determination by Moretti et al. (2003). The predicted numbers of CXB sources account for the incompleteness are described in Sect. 3.5.1. The computed numbers of CXB sources are listed in Table 3.3. In the closest galaxies, background AGN account for a large fraction of detected X-ray sources, especially in M31 where nearly half of the X-ray sources are CXBs. Maffei 1 is a small galaxy that is abundant in LMXBs, and the contamination by CXB sources is minimal. In NGC 3379 and NGC 4278 HST the WFPC2 field-of-views (FOVs) are located in the very central region, where the CXB fraction is less than 10%. In NGC 4697 the CXB fraction is about 15% in the D25 region.

The CXB estimates based on the average source counts are subject to uncertainties caused by angular fluctuations of the density of background AGN. These are likely to be reduced in our analysis as it covers a rather large solid angle composed of non contiguous fields. Nevertheless, for each individual galaxy we verified

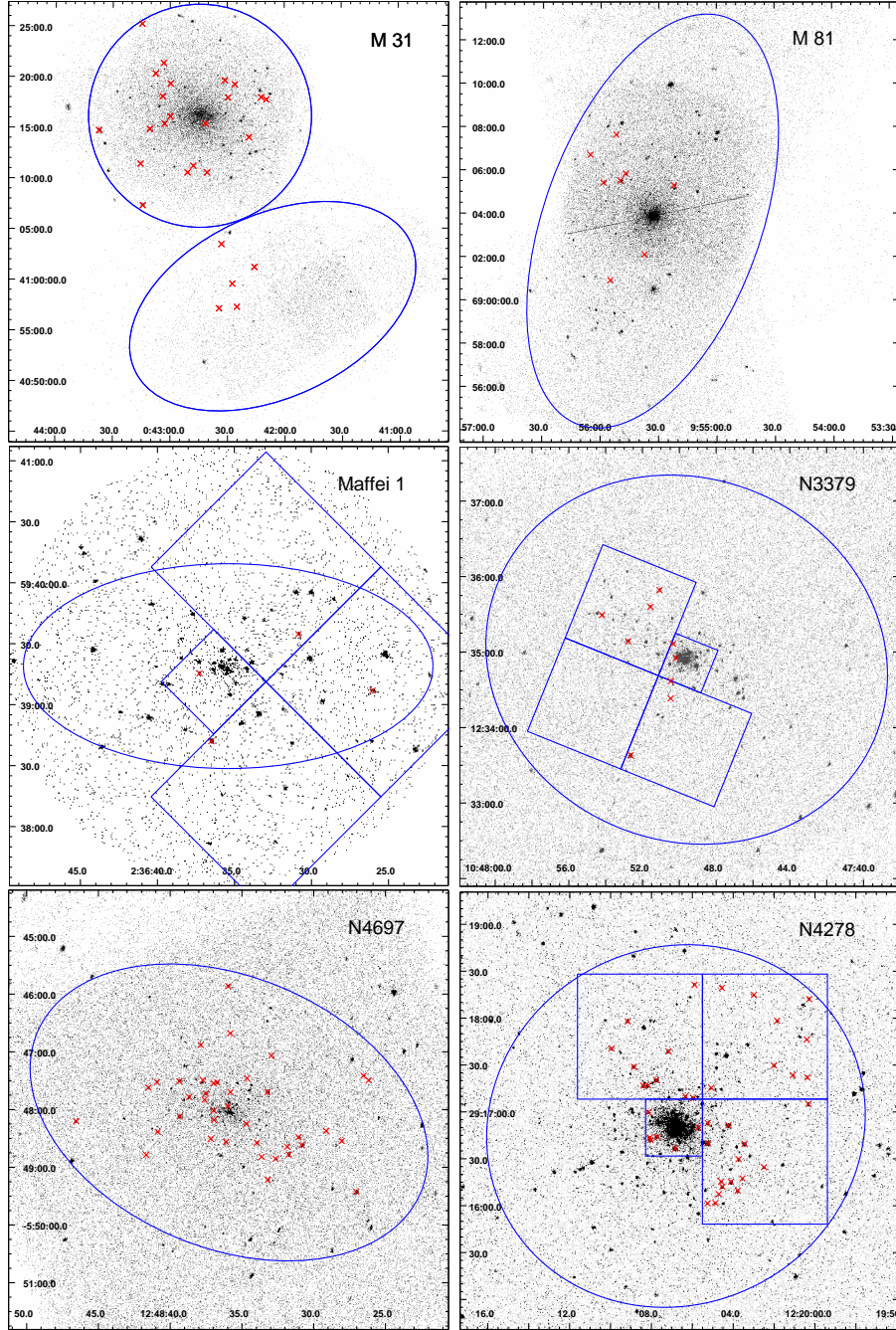


Figure 3.1: X-ray images (0.5–8 keV) of external galaxies and the fields of view studied. For M31 and M81 we study the sources within the ellipses with radii and position angle shown in Table 3.1. For Maffei 1, NGC 3379, NGC 4697, and NGC 4278 ellipses show D25 regions and squares show the HST FOVs. The field of view of interest are the overlapping regions between the two. Crosses show detected GC-LMXBs in each galaxy. The *Chandra* image of Centaurus A can be found in Fig. 1 in Voss et al. (2009).

Table 3.3: Statistics of compact sources I.

Galaxy (1)	N_{XRS} (2)	N_{CXB} (3)	N_{GC} (4)	$K_{\text{opt}}^{\text{GC}}$ (5)	N_{GC}^{X} (6)	$K_{\text{opt}}^{\text{GC,X}}$ (7)	R (8)	N_{r} (9)
M31	386	194	121	1.00	26	1.00	2.0''	0.2
Cen A	231	64	479	0.67 ± 0.03	47	0.55 ± 0.19	2.0''	1.2
M81	220	79	77	0.77 ± 0.09	8	0.84 ± 0.48	3.0''	0.8
Maffei 1	38	1	20	1.00	4	1.00	1.0''	0.3
N3379	59	4	61	0.80 ± 0.10	9	0.74 ± 0.39	1.0''	0.6
N4697	117	17	441	0.85 ± 0.04	39	0.93 ± 0.31	0.8''	1.1
N4278	120	6	266	0.69 ± 0.04	40	0.86 ± 0.29	0.6''	1.8
MW	–	–	150	1.00	12	1.00	–	–
Total	1171	365	1615	–	185	–	–	6.7

Columns are: (1) – Galaxy name. (2) – Total number of resolved X-ray point sources in the study fields. (3) – Predicted number of CXB sources in the study fields above the corresponding sensitivity threshold. (4) – Number of optically identified GCs. (5) – Completeness fraction of GC lists and its 1σ uncertainty, estimated as described in Sect. 3.4.3 (6) – Number of LMXBs found in GCs. (7) – Completeness fraction and its uncertainty of GC lists with respect to GCs containing LMXBs (see Sect. 3.4.3). (8) – Search radius to match XRS to GC. (9) – Expected number of random coincidences of X-ray sources with GCs.

Table 3.4: Statistics of compact sources II.

Galaxy (1)	$N_{\text{GC}}^{\text{X},1}$ (2)	$N_{\text{GC}}^{\text{X},2}$ (3)	$N_{\text{GC}}^{\text{X},3}$ (4)	$N_{\text{GC}}^{\text{X},3}/N_{\text{GC}}$ (5)	$N_{\text{F}}^{\text{X},1}$ (6)	$N_{\text{F}}^{\text{X},2}$ (7)	$N_{\text{F}}^{\text{X},3}$ (8)	$N_{\text{F}}^{\text{X},3}/M_*$ (9)
M31	2	11	12	0.10 ± 0.03	110	64	28	9.5 ± 1.8
Cen A	0	16	30	0.06 ± 0.01	6	85	29	7.2 ± 1.3
M81	0	4	4	0.05 ± 0.03	–	–	–	–
Maffei 1	0	2	2	0.10 ± 0.07	0	6	12	14.8 ± 4.3
N3379	0	0	8	0.13 ± 0.05	0	9	24	6.3 ± 1.3
N4697	0	2	34	0.08 ± 0.01	0	2	66	8.9 ± 1.1
N4278	0	4	36	0.14 ± 0.02	0	3	52	17.4 ± 2.4
MW	1	9	2	0.013 ± 0.009	–	–	–	–
Total	3	48	128	0.08 ± 0.01	116	169	211	9.8 ± 0.7

Columns are: (1) – Galaxy name. Columns (2)–(4) and (6)–(8) – Number of GC-LMXBs (N_{GC}^{X}) and field LMXBs (N_{F}^{X}) in different luminosity ranges (1, 2 and 3 refer to $\log(L_X)$ ranges of 35–36, 36–37 and >37) with incompleteness higher than 0.5. The source numbers are not corrected for incompleteness, and the CXB contribution is not subtracted. Columns (5) and (9) – The specific number of GC-LMXB (per GC) and field LMXBs (per $10^{10} M_{\odot}$) in the highest luminosity bin $\log(L_X) > 37$. The numbers are corrected for incompleteness of X-ray source lists, the contribution of CXB is subtracted. Note that the specific numbers of GC-LMXB are not corrected for incompleteness of the GC lists and are given here as a characterization of our sample, rather than of the properties of GC systems in different galaxies.).

that the observed density of compact sources outside its main body is consistent, within the statistical errors, with the predicted density of CXB sources. This was possible to do directly for Maffei 1, NGC 3379, NGC 4697, and NGC 4278, thanks to their relatively small angular size. For M31 and Centaurus A whose angular extent exceeds or is comparable to the Chandra FOV, we used the results of Voss & Gilfanov (2007b) and Voss et al. (2009). In Centaurus A the CXB source density was found to exceed the average source count by a factor of ~ 1.5 , which that was accounted for in our calculations.

3.4.2 GC-LMXB identification

We correlated the lists of detected X-ray point sources with the GC lists available for M31, M81, Maffei 1, NGC 3379, NGC 4697, and NGC 4278. For Centaurus A we used the results of Voss et al. (2009).

For M31, the most recent and complete GC catalog is a systematic survey using WFCAM on the United Kingdom Infrared Telescope and SDSS by Peacock et al. (2010). In total there are 416 confirmed GCs, with 121 located in the two *Chandra* fields in our study. GCs in M81 are from Perelmuter et al. (1995), Chandar et al. (2001), and Schroder et al. (2002). Chandar's study is based on deep HST observations that cover 25% of our *Chandra* field. We took the 59 GCs from Chandar et al. (2001) and the others from the other two catalogs, which resulted in 77 confirmed GCs in the *Chandra* field. For Maffei 1, there are 20 GCs from HST observation by Buta & McCall (2003). For NGC 3379, we took the 61 GCs from Kundu & Whitmore (2001), which are based on deep HST observations. The GC list for NGC 4697 is taken from Jordán et al. (2011). And the GCs in NGC 4278 are from Kundu & Whitmore (2001) and Brassington et al. (2009).

The search radius R used in cross-correlating the X-ray source lists and GC catalogs was chosen for each galaxy individually based on the following considerations. The number of random matches is $N_r = \pi R^2 \times N_{\text{XRS}} \times N_{\text{GC}}/A$, where N_{XRS} is the number of X-ray point sources, N_{GC} the number of GCs, and A the area of our study field. Because of the rather high source density, the number of random matches may be non-negligible for high values of the search radius R . On the other hand, the search radius has to be broad enough to account for position errors and, for the closest galaxies, the finite angular sizes of GCs. We therefore devised a procedure in which we varied R from 0 to $5''$ (Fig. 3.2). For each value of R we computed the number of true matches as the number of total detected matches minus the predicted number of false matches calculated from the above formula. This number increases with R and saturates at some value of R that depends on the typical positional error and angular extent of GCs. This value of R may be chosen as the optimal match radius. In some cases, however, it results in too high a fraction of false matches in the sample. We therefore set an additional requirement that the predicted number of false matches does not exceed 5% of the total number of matches. This procedure is a simplified version of the method used in Shtykovskiy & Gilfanov (2005). The optimal search radius used for the

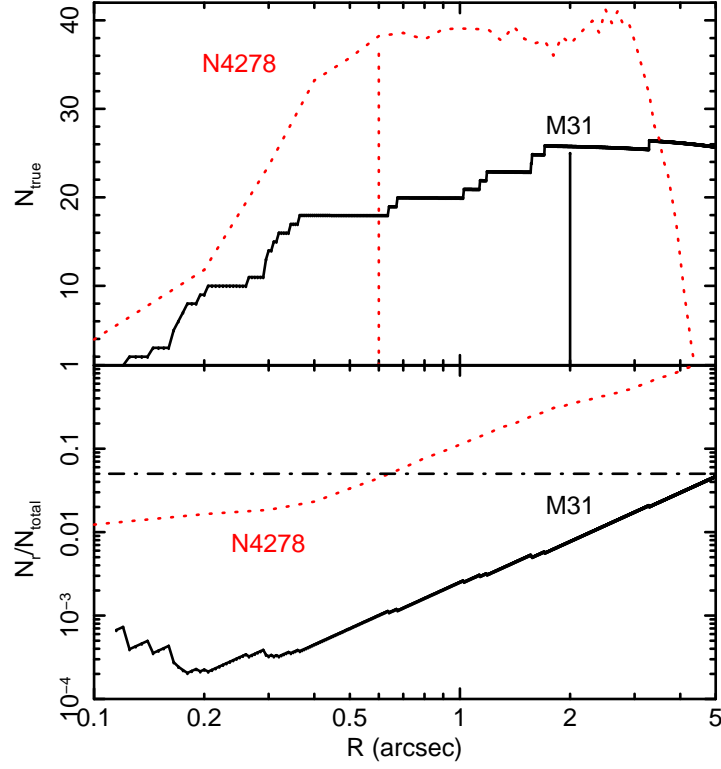


Figure 3.2: Examples of the determination of the optimal search radius for cross-correlation of X-ray source lists with GC catalogs for two galaxies – M31 (solid lines) and NGC 4278 (dashed lines). Upper panel: the number of true matches (N_{true} , computed as the difference between the number of total matches N_{total} and the number of expected random matches N_r) as a function of the search radius R . Lower panel: the ratio of the number of random matches to the number of total matches. The dash-dotted line is the 5% level. The vertical lines in the upper panel show our choice of the search radii for these two galaxies.

3 LMXB dependence on the stellar density and velocity dispersion

program galaxies are listed in Table 3.3. As expected, there is a general trend that nearby galaxies require larger search radii.

The numbers of X-ray sources associated with GCs are listed in Table 3.3 along with the predicted numbers of false matches.

3.4.3 Incompleteness of GCs

Although the availability of the high quality GC optical data was one of the criteria in selecting our galaxy sample, the GC lists are not 100% complete for all of them. The incompleteness of these lists can result in incompleteness of the GC-LMXB lists and can compromise the shape and (less importantly) the normalization of the GC XLF.

In order to estimate the completeness fraction of the GC lists we used the fact that optical luminosity function of GCs (GCLF) can be described to good accuracy by log-normal distribution in the form

$$\frac{dN}{dM} = \frac{1}{\sqrt{2\pi}\sigma} \exp\left[-\frac{(M-\mu)^2}{2\sigma^2}\right], \quad (3.1)$$

where M is the absolute magnitude of GC, μ the turnover luminosity, and σ the dispersion. The turnover luminosity is remarkably constant in different galaxies. We used the following values for different bands: $\mu_V^0 = -7.41$, $\mu_I^0 = -8.46$ (Kundu & Whitmore 2001) and $\mu_g^0 = -7.2$ (Jordán et al. 2007a). The reddening corrected photometry data of GCs for each galaxy (see references in Sect. 3.4.2) was fit by this model using maximum likelihood method. The fitting was performed using only GCs above the completeness limit of the optical data for each galaxy. The width of the distribution σ and normalizations were free parameters of the fit. The data along with the best-fit model are shown for six galaxies from our sample in Fig. 3.3. The completeness fraction of the GC lists K_{opt}^{GC} was then determined as a ratio of the total number of detected GCs (of all magnitudes) to the total number predicted by integrating the best-fit model. The results are listed in Table 3.3. Given the completeness limits of M31 and Maffei 1 data, their GC lists are complete. The list of GCs in the Milky Way is also believed to be reasonably complete (Harris 2001). In agreement with this, the best-fit values obtained for these three galaxies are consistent, within errors, with 1. We therefore set the completeness fraction for these three galaxies equal to unity.

The second factor, required to correctly computing GC XLF is $K_{opt}^{GC,X}$ – the completeness fraction of the GC-LMXB identifications, caused by the incompleteness of the overall GC lists. If the probability of finding an LMXB in a globular was independent of its optical luminosity, the two quantities would coincide: $K_{opt}^{GC,X} = K_{opt}^{GC}$ would hold. However, it has been shown that X-ray sources tend to be associated with brighter GCs (e.g., Sivakoff et al. 2007). This is illustrated by the Fig. 3.4 where we plot the combined LF of all GCs and all the GCs hosting an X-ray source in the three galaxies which GC lists are complete – MW, M31 and Maffei 1. To determine $K_{opt}^{GC,X}$ we assume that LF of GCs hosting an X-ray source

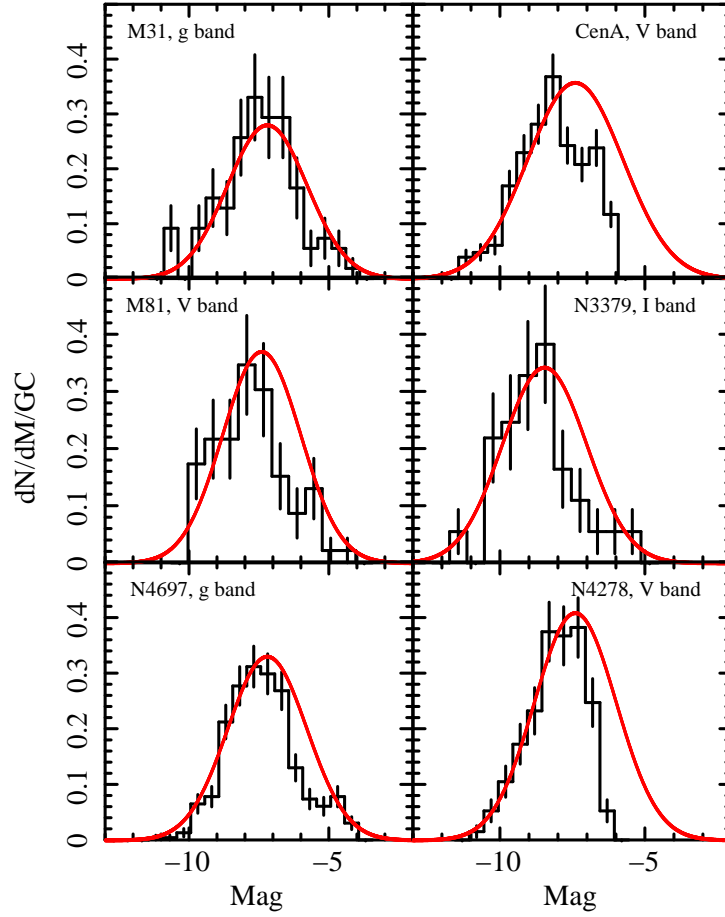


Figure 3.3: The observed luminosity functions of GCs for six galaxies in our sample and their best-fit models. The turnover luminosity of the model in different bands was fixed at the values determined elsewhere (see text), the width σ was a free parameter of the fit.

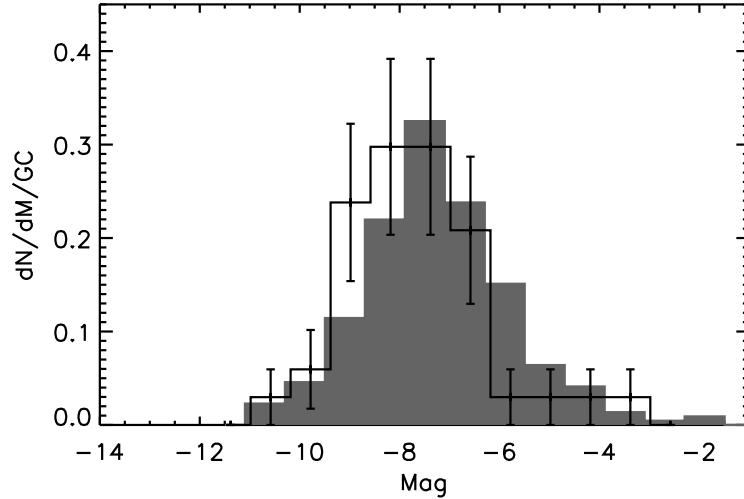


Figure 3.4: The combined LFs of all GCs in the Milky Way, M31, and Maffei 1 (the shaded histogram). The thin solid histogram shows the combined LF of GCs hosting X-ray sources. The Poisson errors for the latter are indicated by the vertical error bars. The statistical errors are ~ 2 -3 times smaller for the combined LF of all GCs.

is the same in all galaxies. Using the combined LFs in Fig. 3.4 as the template, we then use the ratio of the numbers of GCs hosting X-ray sources above and below the threshold magnitude of $V = -7$ ($V = -8$ for Cen A) to estimate the number of missed X-ray sources in GCs in each galaxy. The threshold magnitude was chosen so that the GC lists are complete above its value. The results of this calculation, along with their uncertainties are listed in Table 3.3.

3.4.4 The Milky Way Sources

The luminosities of the Milky Way sources were calculated from the light curves measured by the All-Sky Monitor aboard *RXTE*. The light curves were averaged over the period from January 1996 to June 2009. The count rates were transformed to the 0.5-8.0 keV band fluxes with the conversion factor obtained using PIMMS: 1 count/s = 4.3×10^{-10} erg/cm²/s. A power-law with $\Gamma=1.7$ was assumed. To compute source luminosities we used distances to the GCs from Harris (1996).

The following comments regarding the determination of the luminosities of the Milky Way sources are in order. The ASM fluxes are averaged over a significantly longer time scale than the *Chandra* data for external galaxies. Although both the ASM (\sim years) and *Chandra* ($\sim 1 - 10$ days of total integration time, \sim years time span of observations) integration time scales are much longer than the characteristic time scales of the accretion disk in these sources the variability of the X-ray light curves could in principle result in “clipping” of the XLF i.e. smoothing

out the extrema of long term variability. The effect of averaging ASM light curves on the XLF was studied by Postnov & Kuranov (2005), who came to the conclusion that flux probability distribution functions for persistent galactic X-ray binaries are such that light curve averaging does not modify the shape of the power-law luminosity distribution. To verify this further we considered variations in the XLF obtained by averaging ASM light curves over shorter intervals, comparable to the duration of *Chandra* observations of external galaxies. The results of this analysis are presented in Sect. 3.7.2. However, the effect of such time averaging may be more significant for transients that, for long averaging times, will “accumulate” in the low-luminosity bins and will lead to a steepening of the XLF (Voss & Gilfanov 2007a). It is also an issue for M31, which was observed in several short observations distributed over the time span of a few years, and to a less extent for M81. This can potentially lead to significant distortions of the XLF, depending on the average time and light curve properties of transients. However, as discussed in Sect. 3.7.3, it is not a significant factor in our particular case.

It is also known that one of the Galactic GCs, M15, contains two bright X-ray binaries (White & Angelini 2001). Transients have been detected in two other GCs, NGC 6440 (Heinke et al. 2010) and Terzan 5 (Bordas et al. 2010). The net effect of source blending on the XLF of GCs was considered and shown to be negligible in Voss & Gilfanov (2007a). It is also discussed in Sect. 3.7.4.

3.5 XLFs of different LMXB populations

In combining the data from individual galaxies two effects need to be considered: correction for the incompleteness and removal of the contamination by background AGN. The former has to compensate for the fact that different sensitivities have been achieved for different galaxies, as well as for variations in the source detection sensitivity across the FOV in individual observations. On the other hand, estimation of the contribution of CXB sources in the XLF has to take into account the effects of incompleteness that affect the detection of CXB sources as well.

There are a few different weighting schemes for combining the XLFs; here, we have used the one that produces the best signal-to-noise ratio under the assumption that XLFs of different galaxies have the same shape (Eqs. (3.2) and (3.5) below). Obviously this assumption can only be verified to the accuracy allowed by the statistical quality of the individual XLFs, which is by a factor of a few less than the accuracy of the combined XLF. Indirectly, this assumption is supported by not seeing large variations in the specific frequency of GC and field sources between galaxies (Table 3.4, but see also Sect. 3.7).

3.5.1 X-ray incompleteness function

We calculated the X-ray incompleteness function $K_X(L)$ following Sect. 2.1.5. The incompleteness function for GC and field sources in individual galaxies are shown in the two upper panels in Fig. 3.5. The bottom panel in Fig. 3.5 shows

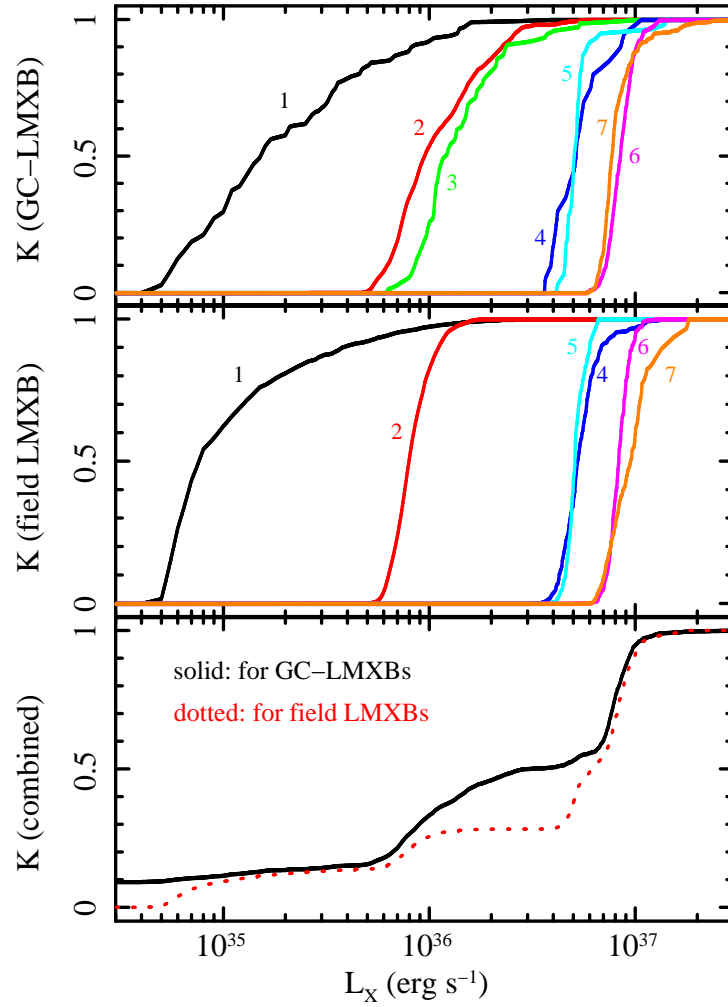


Figure 3.5: The incompleteness functions for individual galaxies from our sample (top panel for GC-LMXBs and middle panel for field LMXBs; the numbers 1, 2, 3, 4, 5, 6, and 7 by the curves refer to M31, Centaurus A, M81, Maffei 1, NGC 3379, NGC 4697, and NGC 4278, correspondingly). The bottom panel shows the combined curves for GC (solid line) and field (dotted line) sources. L_X is the unabsorbed X-ray luminosity in 0.5-8 keV.

the combined incompleteness functions for GC and field sources computed by summing individual incompleteness functions weighted by the number of GC and stellar mass inside the study area of each galaxy. Since the distributions of GCs and stellar mass do not differ strongly, one may expect these two functions to be nearly identical. This is in fact the case throughout most of the luminosity range. The two curves diverge near $\sim 5 \times 10^{36}$ erg/s because of the different areas used to study GC and field sources in Centaurus A (see Voss et al. 2009, for details). The difference below $\sim 10^{35}$ erg/s is caused by only using GC sources for the Milky Way.

3.5.2 Combined LF of GC-LMXBs

There are 185 GC-LMXBs in total in our sample. To avoid uncertainties from the highly incomplete low-luminosity end, we adopted a completeness threshold of 0.5 and used the curves shown in the upper panel of Fig. 3.5 for each galaxy to determine the corresponding luminosity limit. Sources below these limits were excluded from the XLF construction. This procedure excluded source numbers 13, 39, 98, 107, 108, and 109 from Table 3.6. The XLF value in the j -th luminosity bin centered at L_j and having a width of $\Delta \log(L_j)$ was computed according to the equation:

$$\left(\frac{dN}{d \log(L_j)} \right)^{GC} = \frac{1}{\Delta \log(L_j)} \sum_{k=1}^{N_{gal}} \sum_{L_i^k \in \Delta L_j} \frac{1}{N_{eff}^{GC}(L_i^k)}, \quad (3.2)$$

where N_{eff}^{GC} is the effective number of GCs involved in the calculation of the XLF at the given luminosity L_X , corrected for optical and X-ray incompleteness. It depends on X-ray luminosity because it accounts for the X-ray incompleteness,

$$N_{eff}^{GC}(L) = \sum_{k=1}^{N_{gal}} N_k^{GC} \frac{K_{opt}^{GC,X}}{K_{opt}^{GC}} K_{X,k}^{GC}(L), \quad (3.3)$$

where N_k^{GC} is the number of observed GCs in the study field of the k -th galaxy, $K_{X,k}^{GC}(L)$ is the X-ray incompleteness function for GC sources in the k -th galaxy, the $K_{opt,k}^{GC,X}$ and $K_{opt,k}^{GC}$ are optical completeness factors, described in Sect. 3.4.3 and listed in Table 3.3. The thus computed XLF is normalized per GC.

The effective X-ray incompleteness of the GC data can be defined as

$$K_{tot}^{GC}(L) = \frac{\sum_{k=1}^{N_{gal}} N_k^{GC} K_k^{GC}(L)}{\sum_{k=1}^{N_{gal}} N_k^{GC}}. \quad (3.4)$$

This is the quantity plotted in Fig. 3.5 (individual $K(L)$ not clipped at the incompleteness level of 0.5 when plotting the figure).

The factor $K_{opt}^{GC,X}/K_{opt}^{GC}$ in eq.(3.3) accounts for the incompleteness of the optical GC data. The denominator in this expression, $K_{opt}^{GC,X}$, is rather poorly

3 LMXB dependence on the stellar density and velocity dispersion

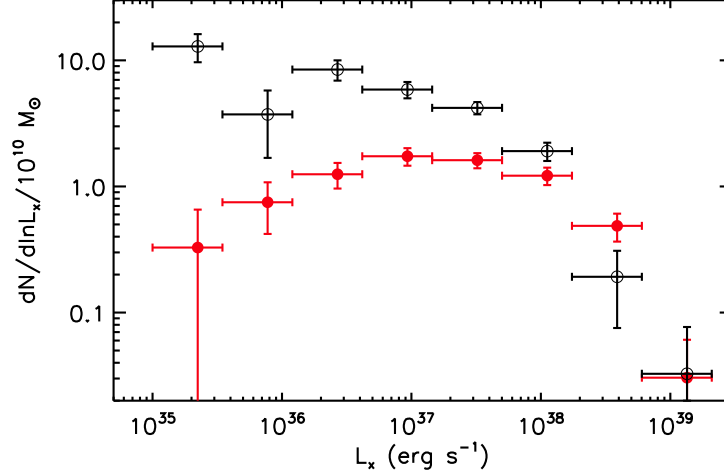


Figure 3.6: The combined XLFs of LMXBs in GC (filled circles) and in the field (open circles). L_X is the unabsorbed X-ray luminosity in 0.5-8 keV. The contribution of CXB sources was subtracted and the incompleteness correction was applied. The field XLF is normalized to stellar mass of $10^{10} M_\odot$. The GC XLF is normalized to have the same number of sources as the field XLF above 10^{38} erg/s.

constrained by our data (Table 3.3) and is consistent with $K_{opt}^{GC,X} = K_{opt}^{GC}$ within the measurement uncertainties. In fact, given the amplitude of the uncertainties, using the best-fit values would introduce additional noise into the obtained XLF. We therefore assumed that $K_{opt}^{GC,X} = K_{opt}^{GC}$ in the further calculations. With this assumption the incompleteness of the optical data cancels out (see the discussion in the beginning of the last paragraph in Sect. 3.4.3). The impact of this assumption on the final LF of GC-LMXBs is investigated in Sect. 3.7.

In the case of GC sources, the contamination by background AGN is insignificant so was ignored. Indeed, the predicted total number of random matches between resolved CXB sources and GC positions with the given search radii from Table 3.3 is ≈ 1.1 . The final XLF of GC sources is shown in Fig. 3.6. The incompleteness-corrected number of GC sources with luminosity exceeding 10^{35} erg/s is ≈ 244 .

3.5.3 Combined LF of field LMXBs

We have only considered field sources in elliptical galaxies and the bulges of spiral galaxies, in order to minimize the contamination by HMXBs. M81 was not included due to the relatively small size of its bulge. Thus, the bulge regions of M31, Maffei 1, NGC 3379, NGC 4278, and NGC 4697 were combined with the Centaurus A observations. For the last, we excluded the jet and radio lobe regions that have small-scale structures in the diffuse emission (Voss et al. 2009). In M31

3.5 XLFs of different LMXB populations

we excluded the sources located in the central $1'$ of the galaxy since they have been demonstrated as very likely dynamically formed (Voss & Gilfanov 2007a). A separate XLF was constructed for these 36 sources, as discussed in the next section. In Maffei 1, NGC 3379, NGC 4278, and NGC 4697 the central $10''$ were excluded. These regions are affected by source confusion, which makes accurate luminosity estimates difficult. We then followed a procedure similar to the GC sources by applying a luminosity threshold corresponding to $K(L) = 0.5$ in each galaxy. With these selection criteria we obtained 496 sources above 10^{35} erg/s, of which ~ 177 are predicted to be CXB sources.

In order to correctly subtract CXB contribution one has to take into account the difference in the incompleteness functions for CXB sources and LMXBs:

$$\left(\frac{dN}{d\log(L_j)}\right)^{LMXB} = \frac{1}{\Delta\log(L_j)} \sum_{k=1}^{N_{gal}} \left(\sum_{L_i^k \in \Delta L_j} \frac{1}{K_{tot}^{LMXB}(L_i^k)} - \int_{L \in \Delta L_j} 4\pi D_k^2 \frac{dN^{CXB}}{dL} \frac{K_k^{CXB}(L)}{K_{tot}^{LMXB}(L)} dL \right), \quad (3.5)$$

where D_k is the distance to the k -th galaxy, $K_{tot}^{LMXB}(L)$ the combined incompleteness function for LMXBs computed similar to eq.(3.4), and $4\pi D_k^2 \times dN^{CXB}/dL$ is the $\log(N) - \log(S)$ distribution for the CXB sources. In practice we implemented this by adding a large number ($\sim 10^3$) of fake sources with small negative weights to each galaxy's source list. This accounted for the CXB $\log(N) - \log(S)$ distribution and incompleteness function of the galaxy. The sum of these weights for each galaxy equals the predicted number of CXB sources in this galaxy. These "enhanced" source lists were used to produce the combined XLF according to eq.(3.5):

$$\left(\frac{dN}{d\log(L_j)}\right)^{LMXB} = \frac{1}{\Delta\log(L_j)} \sum_{k=1}^{N_{gal}} \left(\sum_{L_i^k \in \Delta L_j} \frac{1}{K_{tot}^{LMXB}(L_i^k)} - \sum_{L_i^{cxb} \in \Delta L_j} \frac{w_i^{cxb}}{K_{tot}^{LMXB}(L_i^{cxb})} \right). \quad (3.6)$$

The final XLF for field sources normalized to unit stellar mass is shown in Fig. 3.6. The total stellar mass involved in this calculation is $1.82 \times 10^{11} M_\odot$. The specific frequency of LMXBs above $10^{36}(10^{37})$ erg/s is 25.7(9.6) per $10^{10} M_\odot$, which is consistent with the average values from Gilfanov (2004) – 33.9(14.3).

3.5.4 LF of sources in the nucleus of M31

Voss & Gilfanov (2007a) demonstrate that most sources in the inner $\sim 1'$ of M31 are very likely to have formed dynamically, similar to the sources in GCs. In

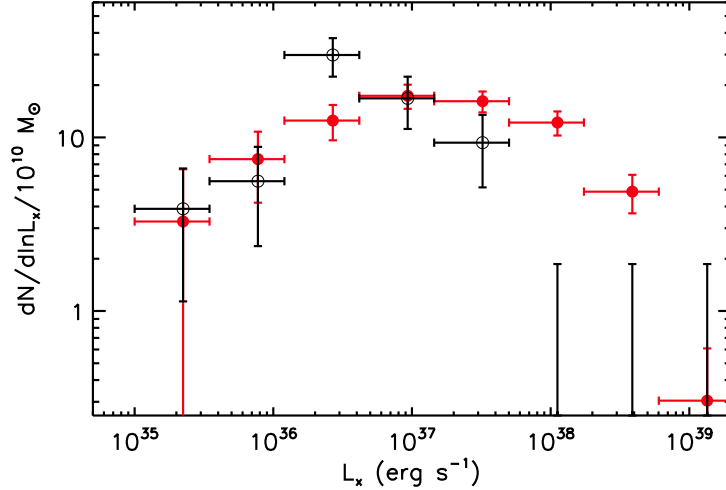


Figure 3.7: The XLFs of sources in the inner $1'$ of M31 (open circles) and of GC sources (filled circles). L_X is the unabsorbed X-ray luminosity in 0.5–8 keV. The normalization of the GC XLF is arbitrary. No sources are detected in the three highest luminosity bins of the M31 XLF.

particular, they find that their spatial distribution follows the ρ_*^2 law, in contrast to the X-ray sources outside this region, where the density is proportional to the stellar density. We updated the LMXB list in this region using an exposure approximately twice of the one presented in Voss & Gilfanov (2007a). We have detected three new sources, bringing the total number to 36 (The increase in the number of sources for a $\log(N) - \log(S)$ distribution with the slope of -1 would be ~ 13). We excluded one source that coincided with a GC and computed the luminosity distribution of the detected sources, performing incompleteness correction and CXB subtraction as described before. The resulting XLF is shown in Fig. 3.7 along with the XLF of GC sources. It is obvious from the plot that the two distributions have similar shapes at $\log(L_X) \gtrsim 37$ but differ at the bright end, with the XLF of the sources in the M31 nucleus having a deficit of bright sources. To test the statistical significance of this conclusion we ran the same tests as we did to compare XLFs of GC and field LMXBs in Sect. 3.6. We found that the LF of LMXBs in the M31 nucleus differs from the GC XLF with a significance ≈ 2.6 – 2.8σ (Table 3.5). In other words, one should expect 26 sources with $\log(L_X) > 37$ in the nucleus of M31, assuming that both distributions have the same shape and using the number of faint sources for normalization. The observed number of bright sources is 11, which is $\approx 3\sigma$ less than expected. Both calculations give similar results, confirming the marginal significance of our conclusion.

Although both populations were formed dynamically, there is an important difference between stellar environments in GCs and galactic nuclei: stellar velocities in the latter are about $\sim 10 - 20$ times higher. This leads to different forma-

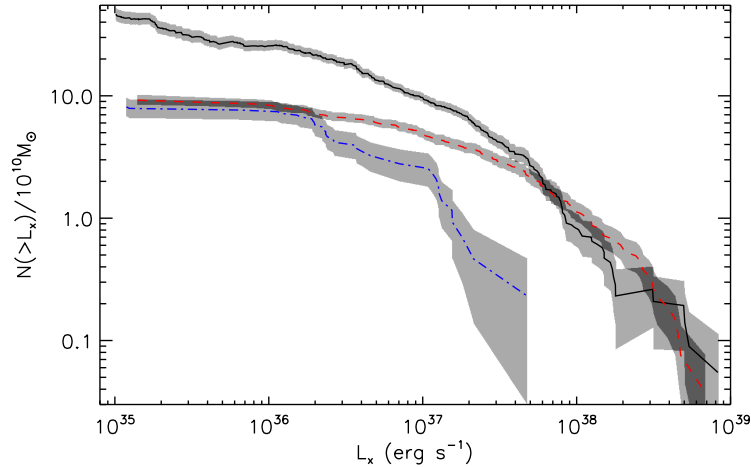


Figure 3.8: The combined XLFs of LMXBs in different environments plotted in the cumulative form. L_X is the unabsorbed X-ray luminosity in 0.5–8 keV. The contribution of CXB sources was subtracted and the incompleteness correction was applied. The field XLF (solid) is normalized to the stellar mass of $10^{10} M_\odot$. The normalizations of GC (dashed) and M31 nucleus (dash-dotted) XLFs are arbitrary. The shaded areas around the curves show 1σ statistical uncertainty.

tion channels in GCs and galactic nuclei (Voss & Gilfanov 2007b, and references therein). Calculations of Voss & Gilfanov (2007b) suggest that in the high-velocity environment of the M31 nucleus the main formation channel for X-ray binaries may be tidal captures of compact objects by low-mass stars, producing short orbital period binaries. In GCs, in contrast, LMXBs are predominantly formed in exchange reactions and collisions of neutron stars with evolved stars. Obviously, this difference will affect the distributions of binary systems over the mass accretion rate. Detailed population synthesis calculations are required to understand what this effect may be and to interpret the observed luminosity distributions in a more quantitative and meaningful manner.

3.6 Results

The background-subtracted and incompleteness-corrected XLFs of the GC and field LMXBs are shown in Figs. 3.6 and 3.8. The XLF of field sources is normalized to a stellar mass of $10^{10} M_\odot$. The XLF of GC sources is normalized to the same number of sources above 10^{38} erg/s as the field XLF. It is obvious from the plot that the two luminosity distributions have different shapes. Although they differ across the entire luminosity range, the most evident difference is at lower luminosities, below $\log(L) \sim 37$. Both XLFs change their slope between

3 LMXB dependence on the stellar density and velocity dispersion

Table 3.5: Comparison of XLFs of different populations.

	$L_{min} = 10^{35}$	$L_{min} = 10^{36}$
R_{GC}	$0.89^{+0.18}_{-0.16}$	$0.71^{+0.13}_{-0.12}$
R_F	$3.82^{+0.65}_{-0.61}$	$1.67^{+0.28}_{-0.27}$
R_C	$2.18^{+1.07}_{-0.64}$	$1.91^{+0.97}_{-0.58}$
$P(R_F < R_{GC})$	$< 10^{-7}$ ($> 5\sigma$)	$3.6 \cdot 10^{-4}$ (3.6σ)
$P(R_C < R_{GC})$	$8.3 \cdot 10^{-3}$ (2.6σ)	$4.6 \cdot 10^{-3}$ (2.8σ)

R_{GC} , R_F , and R_C are ratios of the number of faint sources ($L_{min} < L_x < 10^{37}$ erg/s) to the number of bright sources ($L_x > 10^{37}$ erg/s) for GCs, field sources, and sources in the inner 1' of M31. P is the probability that the luminosity distributions of corresponding populations are drawn from the same mean (see text for details).

$\log(L) \sim 37 - 38$. Due to their rather complicated shapes we did not attempt to do global fits with analytical functions. Instead, we perform power-law fits to the high- and low-luminosity ends. We did maximum-likelihood fits to the background-subtracted XLFs. To account for the incompleteness, we multiplied the model by the respective incompleteness function. In the $\log(L) \geq 38$ range, we obtained differential slopes of $1.70^{+0.60}_{-0.58}$ and $2.06^{+0.92}_{-0.75}$ for GC and field sources correspondingly. At the faint end, $\log(L) \leq 37$ the slopes are: $0.68^{+0.21}_{-0.23}$ and $1.17^{+0.13}_{-0.14}$ respectively. The slopes of the field sources are broadly consistent with the parameters of average LMXB XLFs from Gilfanov (2004).

Differences in the incompleteness curves and in the CXB contribution render direct application of the K-S test to compare these two XLFs impossible. We have therefore considered the ratio of the number of faint to bright sources in order to assess the statistical significance of the difference between the two XLFs, the same method as used in Voss et al. (2009). For each population we computed the ratio $R = N_{faint}/N_{bright}$, with the boundary between faint and bright set to 10^{37} erg/s. We ran Monte-Carlo simulations to calculate statistical errors and the significance of our results. The details of these calculations are described in Voss et al. (2009). For each XLF we did 10^7 Monte-Carlo runs. The results are listed in Table 3.5. The lines marked ‘‘P’’ give the probability of obtaining the observed values of R due to statistical fluctuations, while their mean (true) values obey the relation given in parenthesis. These numbers can be interpreted as the probability that the corresponding luminosity distributions are drawn from the same mean. The upper limit of $< 10^{-7}$ in the left column means that no such realizations were detected in 10^7 Monte-Carlo runs.

These calculations show that the GC and field XLFs differ at a confidence level of $< 10^{-7}$, which corresponds to a significance of $> 5\sigma$. To investigate the robustness of this conclusion we have also used a more restricted luminosity range of $\log(L_X) > 36$, where the incompleteness functions vary less and different galaxies

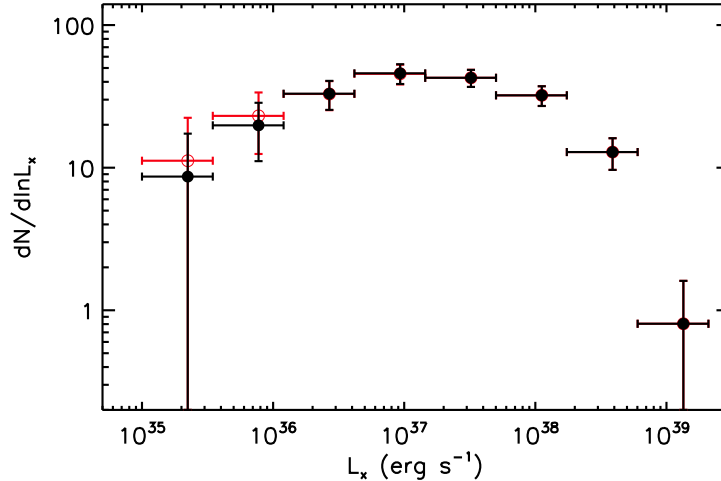


Figure 3.9: The maximum possible effect of the optical incompleteness on the GC LMXB XLF. The solid symbols show the XLF computed assuming $K_{opt}^{GC,X} = K_{opt}^{GC}$ (our default version), open circles – assuming $K_{opt}^{GC,X} = 1$ (the maximum possible correction). To emphasize the effect on the shape, rather than overall normalization, the XLF are normalized to the total number of detected GCs. See Sect. 3.4.3, 3.5.2, and 3.7 for details.

from our sample make more uniform contributions. In this case the confidence level decreases to $3.4 \cdot 10^{-4}$ (3.6σ), but the conclusion still holds.

3.7 Caveats

Several caveats regarding possible systematic effects are discussed in the following sections.

3.7.1 Incompleteness of GCs

We used a rather inhomogeneous set of the GC lists, having varying degree of completeness. The procedure of correction for incompleteness of the optical data is described in Sect. 3.4.3 and 3.5.2. Its accurate implementation, however, was hindered by the large statistical uncertainties of the completeness fraction of the GCs hosting an X-ray source, $K_{opt}^{GC,X}$. As results of Sect. 3.4.3 were consistent with $K_{opt}^{GC,X} = K_{opt}^{GC}$ (the latter much better constrained), we assumed that this relation holds for all galaxies. This could be the case, for example, if the probability of finding an LMXB did not depend on the optical luminosity of the GC. However, this is known not to be the case (e.g., Sivakoff et al. 2007) (see Fig. 3.4). As is obvious from Eq.(3.3), the optical incompleteness would have the strongest effect

3 LMXB dependence on the stellar density and velocity dispersion

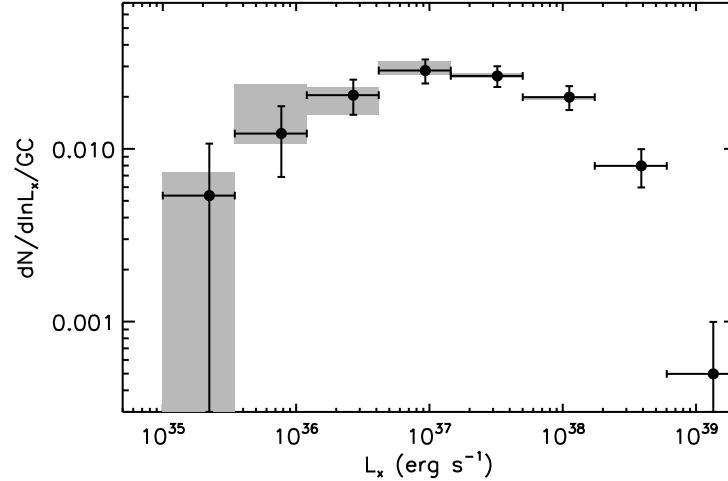


Figure 3.10: The combined XLF of GC-LMXBs. L_X is the unabsorbed X-ray luminosity in 0.5-8 keV. The XLF uncertainty shown by the shaded regions is due to the variability of GC-LMXBs in the Milky Way.

on the XLF if for all galaxies $K_{opt}^{GC,X} = 1$ (i.e. if all LMXBs were located in the brightest GCs and not subject to optical incompleteness at all, which is not true either). To illustrate its amplitude, we show in Fig. 3.9 the XLFs computed in these two limiting cases. As is obvious from the plot, the XLF does not change by more than $\sim 20 - 30\%$ in the two lowest luminosity bins. We emphasize that the example shown in the plot illustrates the maximum possible effect of the optical incompleteness, the real effect being smaller.

3.7.2 Variability of GC-LMXBs in the Milky Way

About half of the GCs with X-ray sensitivity in the lowest luminosity domain, $\log(L) \gtrsim 36$ are located in the Milky Way. The flux determination of the latter, based on the averaging of the ASM light curves, may be subject to systematic effects. It is different from those affecting *Chandra* galaxies data as discussed in Sect. 3.4.4. Primarily, this is due to the long integration times of ASM light curves. To investigate its effect on the XLF, we divided the ASM light curves into 100 sub intervals with a duration of 50 days each (comparable to the integration time of the longest *Chandra* observations) and recalculated the GC XLF 100 times, each time using the data from different sub intervals to compute ASM fluxes for the Milky Way sources. The range of obtained XLF values is shown by shaded area in Fig. 3.10. As is obvious from the plot, the long integration time of ASM data does not affect the GC XLF significantly.

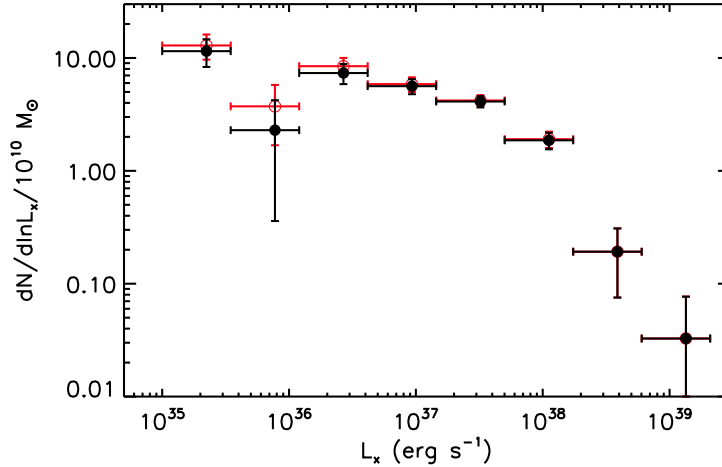


Figure 3.11: The combined XLFs of field sources with (open circles) and without (filled circles) transient sources in M31. L_X is the unabsorbed X-ray luminosity in 0.5–8 keV. Due to multiple short observations averaging the luminosities of transients (which are bright in only a few observations and faint in many others) the number of faint sources is artificially increased, making the XLF appear steeper. See text for details.

3.7.3 Transient sources in M31

If the time span of observations is longer than the typical time scale of transient sources, averaging of their luminosity can also modify the shape of the luminosity distribution, making it steeper (Voss & Gilfanov 2007a). The typical decay time scales of the Galactic transient sources are in the \sim weeks–months range. Thus, for the Milky Way GCs, this issue is addressed by the above exercise with the ASM light curves, and Fig. 3.10 demonstrates that averaging of transients does not result in significant modifications of XLF, given its statistical quality. This issue is also relevant for the multiple *Chandra* observations of M31 and, to a less extent, M81. Indeed, the *Chandra* image of the bulge of M31 was obtained by combining more than 40 short (\sim 5 ks) observations. As transients are bright only in a few observations and dim in many others, they will tend to accumulate in the low-luminosity bins, making the XLF steeper. In Voss & Gilfanov (2007a) 28 transients were reported, two of which (Src. 22 and Src. 35 in Table 3.6) are in our GC-LMXB source list and 21 are in the field source list. We recomputed the luminosity distributions excluding these sources and did not find any significant changes (Fig. 3.11). The results of the statistical tests reported in Table 3.5 are not changed significantly either: the probability $P(R_F < R_{GC})$ for the full luminosity range remains $< 10^{-7}$ (although this may be affected somewhat by the incompleteness of the transient list at the faint end) for sources with $\log(L_X) >$

36 it changes from $3.6 \cdot 10^{-4}$ to $2 \cdot 10^{-3}$ (from 3.6σ to 3.1σ). This proves that the contamination by transient sources in M31 does not significantly bias our results. It is much less significant for other galaxies, as they were observed by *Chandra* in much fewer longer observations. Thus, averaging of persistent and transient sources does not lead to significant (as compared to statistical errors) distortions of the XLFs derived in this paper and does not affect our results in any significant way. This conclusion should not be taken out of the context though. In a more general case, the effects discussed above may be important and may need a more elaborate treatment.

3.7.4 Multiplicity of X-ray sources in GCs

Another factor that can modify the apparent XLF of GC LMXBs is the multiplicity of X-ray sources in GCs, which can affect both Milky Way data and *Chandra* data for external galaxies. We use the Milky Way GCs to estimate its impact on XLF. One of the Milky Way GCs, M15, is known to contain two persistent LMXBs (X2127+119-1 and X2127+119-2) with instantaneous luminosities of 9.5×10^{35} erg/s and 1.5×10^{36} erg/s (converted to 0.5-8 keV band) (White & Angelini 2001). Obviously these two sources could not be resolved by ASM, which measured the long-term average luminosity of 4.05×10^{36} erg/s. Similarly, they would not be resolved by *Chandra* in any of our external galaxies with the exception of M31, where it may be marginally possible. Two bright transients have been detected recently, in NGC 6440 (Heinke et al. 2010) and Terzan 5 (Bordas et al. 2010) with the luminosities in the $\sim 10^{36} - 10^{38}$ erg/s range. Their effect on the "snapshot" XLF would depend on their unknown duty cycle. Assuming a duty cycle of ~ 0.5 , which seems to be a very generous upper limit, the multiplicity fraction for the Milky Way GCs is $\sim 1/12 - 2/12 \approx 8 - 16\%$. As demonstrated in Voss & Gilfanov (2007a), the multiplicity at the level of $\sim 10\%$ does not modify the luminosity distribution in any significant way. We also checked to see how the GC XLF is affected if the ASM M15 source is replaced by two source with the luminosities determined by *Chandra* and the transient source in NGC 6440 at its brightest state is added to the sample. The overall effect on the XLF is insignificant and the R_{GC} changed from $0.89^{+0.18}_{-0.16}$ to $0.92^{+0.17}_{-0.14}$, which is also negligible. We conclude that unless the multiplicity is much higher in external galaxies, it does not affect our conclusions in any significant way.

3.7.5 Other caveats

The distance uncertainties, in the limit of several galaxies, will smooth out the luminosity distributions. For a smaller sample (which is the case for the current study), there could be a non trivial effect on the computed XLFs. However, the distances to the galaxies in our sample are fairly well known, with an accuracy of $\sim 5 - 15\%$ (Table 3.1). This translates to $\sim 10 - 30\%$ uncertainty in the luminosity and $\sim 4 - 11\%$ in its logarithm. This is a factor of $\sim 4 - 12$ smaller than the bin

width used in the XLF calculations. Thus it should not affect the measured XLFs in any significant way.

Combining XLFs necessarily involves an assumption regarding the similarity of their shapes in individual galaxies. Although we did not detect statistically significant differences between different galaxies, this assumption cannot be verified directly at the same level of accuracy as provided by the output average XLF. On the other hand, we do detect marginally significant variations in the specific frequency of X-ray sources in GCs between galaxies, although these may be related, at least in part, to the incompleteness of the GC lists in more distant galaxies. However, if they are real, they may be accompanied by variations in the XLF shapes. The effect of such variations may be further amplified by the fact that data for different luminosities come from different galaxies. The low-luminosity domain, $\log(L) < 36$, is covered exclusively by the nearby M31 and Milky Way, whereas the bright end is dominated by sources located in more massive but more distant galaxies, such as Centaurus A and NGC 4697. This is another unavoidable limitation, as bright sources, although more easy to detect, are less frequent, and it takes a bigger galaxy to have them in large numbers. On the other hand, bigger galaxies are more distant and the sensitivity achieved in a typical *Chandra* observation is lower. Conversely the nearby galaxies, where fainter sources can be studied, tend to be less massive and contain fewer bright sources. Luckily, the 800 ksec Very Large *Chandra* program on Centaurus A and relatively good coverage of M31 allowed us to bridge faint, intermediate, and bright luminosity ranges.

3.8 Conclusions

The aim of this study was to produce accurate luminosity distributions of LMXBs in different environments – dynamically formed systems in GCs, in the nucleus of M31 and field sources of presumably primordial origin – in order to facilitate their quantitative comparison and to provide input for verifying population synthesis models. This goal required a broad luminosity coverage with a point source detection sensitivity reaching 10^{35} erg/s and, on the other hand, good sampling of the high-luminosity end, where the specific frequency of sources (per GC or per unit stellar mass) is low. As this combination of properties cannot be achieved with a single galaxy, we combined the data from a number of galaxies. To this end, we assembled a sample of galaxies from the public *Chandra* archive which is best suited to our study. It included seven nearby galaxies (M31, Maffei 1, Centaurus A, M81, NGC 3379, NGC 4697, and NGC 4278) and the Milky Way. We detected 185 X-ray sources in 1615 GCs, 36 sources in the nucleus of M31, and 998 sources in the fields of galaxies (of which ≈ 365 are expected to be background AGN). These sources were used to produce the average luminosity distributions of different populations. In doing so we took special care to accurately subtract resolved CXB sources and correct for incompleteness effects. As a result, we produced XLFs of LMXBs with a statistical accuracy that far exceeds what has been

achieved in previous studies.

We demonstrate that, although the luminosity distributions of LMXBs in different environments are similar in a broad sense (e.g., when compared with XLF of HMXBs), their detailed shapes are different. Although the fraction of faint LMXBs ($\log(L_X) < 37$) in GCs is ~ 4 times smaller than in the field, in agreement with a suggested effect found in previous studies, the difference in their XLFs cannot be described merely in terms of a roll over of the XLF of GC sources. Rather, the luminosity distributions of these two populations of LMXBs appear to be different throughout the entire luminosity range. This may present a challenge for the models suggesting that the entire LMXB population was formed dynamically in GCs and then expelled to the field due to kicks, dynamical interactions, or GC destruction.

We also compare luminosity distributions of LMXBs in the nucleus of M31 (its inner $1'$) and in GCs. We find that although their shapes at the low-luminosity end are similar (and different from the field sources), the M31 nuclear population appears to have far fewer luminous sources than GCs (and field population). For example, the most luminous source in the nucleus of M31 has the luminosity of 4.7×10^{37} erg/s. If the XLFs were drawn from the same parent distribution, we would expect to see 11 sources above this luminosity, whereas we found none. Different estimates of the statistical significance of the difference between the two XLFs give results in the $\sim 2.5-3\sigma$ range. The difference between the XLFs is likely caused by the factor of $\sim 10-20$ difference in stellar velocities in GCs and galactic nuclei, which leads to different dynamical formation channels. However detailed population synthesis calculations are needed in order to understand the particular mechanisms responsible for forming the observed luminosity distributions.

Table 3.6: All the 185 LMXBs in GCs in our sample. X-ray luminosity is in 0.5-8 keV range, in units of 10^{36} erg/s.

Number (1)	Galaxy (2)	RA(J2000) (3)	DEC(J2000) (4)	Luminosity (5)
1	MW	+17:35:47.64	-30:28:55.70	0.14
2	MW	+18:53:04.89	-08:42:19.70	1.14
3	MW	+17:48:53.54	-20:22:02.00	1.31
4	MW	+18:35:44.00	-32:58:55.40	1.68
5	MW	+17:50:45.54	-31:17:32.50	1.76
6	MW	+17:48:55.73	-24:53:40.10	1.78
7	MW	+05:14:06.59	-40:02:37.00	2.34
8	MW	+21:29:58.33	+12:10:02.80	4.05
9	MW	+17:33:24.06	-33:23:16.20	5.00
10	MW	+17:27:33.25	-30:48:07.40	6.79
11	MW	+17:50:12.66	-37:03:08.20	14.70
12	MW	+18:23:40.57	-30:21:40.60	66.12
13	M31	+00:42:29.64	+41:17:57.27	0.04
14	M31	+00:42:50.86	+41:10:33.72	0.41
15	M31	+00:43:14.65	+41:25:13.32	0.84
16	M31	+00:42:27.43	+40:59:35.63	1.05
17	M31	+00:42:34.40	+40:57:09.31	1.07
18	M31	+00:43:15.48	+41:11:25.69	1.17
19	M31	+00:42:40.60	+41:10:33.60	1.39
20	M31	+00:42:25.04	+40:57:18.78	2.09
21	M31	+00:42:41.43	+41:15:23.71	2.53
22	M31	+00:42:47.81	+41:11:13.66	2.56
23	M31	+00:43:07.51	+41:20:19.44	3.24
24	M31	+00:42:33.10	+41:03:29.86	4.23
25	M31	+00:42:09.51	+41:17:45.42	9.31
26	M31	+00:42:26.05	+41:19:14.81	9.94
27	M31	+00:42:12.17	+41:17:58.62	11.51
28	M31	+00:43:03.31	+41:21:21.60	12.02
29	M31	+00:42:31.25	+41:19:38.78	18.50
30	M31	+00:43:02.93	+41:15:22.47	22.50
31	M31	+00:43:03.86	+41:18:04.79	28.37
32	M31	+00:42:59.86	+41:16:05.64	33.75
33	M31	+00:42:59.65	+41:19:19.18	34.19
34	M31	+00:42:18.64	+41:14:01.74	36.23
35	M31	+00:43:14.31	+41:07:19.68	46.14
36	M31	+00:43:37.29	+41:14:43.63	47.94
37	M31	+00:43:10.61	+41:14:51.24	77.93
38	M31	+00:42:15.84	+41:01:14.32	123.26

3 *LMXB dependence on the stellar density and velocity dispersion*

Table 3.6: Continued.

Number (1)	Galaxy (2)	RA(J2000) (3)	DEC(J2000) (4)	Luminosity (5)
39	Cen A	+13:25:41.76	-42:57:00.00	0.90
40	Cen A	+13:25:11.04	-43:01:31.80	1.79
41	Cen A	+13:25:29.28	-42:57:46.80	1.90
42	Cen A	+13:25:14.88	-43:00:48.96	1.92
43	Cen A	+13:25:42.00	-43:03:19.44	2.15
44	Cen A	+13:25:58.32	-43:08:06.72	3.15
45	Cen A	+13:25:43.20	-42:58:37.20	3.57
46	Cen A	+13:25:35.28	-43:05:29.40	4.45
47	Cen A	+13:24:49.20	-43:05:12.12	4.81
48	Cen A	+13:25:27.60	-43:05:24.72	5.19
49	Cen A	+13:25:32.40	-43:04:40.44	6.25
50	Cen A	+13:24:58.08	-42:56:10.32	6.84
51	Cen A	+13:25:14.16	-43:02:42.72	7.01
52	Cen A	+13:25:22.08	-43:02:45.24	7.68
53	Cen A	+13:25:30.24	-42:59:34.80	7.83
54	Cen A	+13:25:32.88	-42:56:24.36	8.54
55	Cen A	+13:24:50.40	-43:04:50.88	9.16
56	Cen A	+13:25:38.40	-42:57:19.80	10.12
57	Cen A	+13:25:12.00	-42:57:12.96	10.27
58	Cen A	+13:26:07.68	-42:52:01.56	10.40
59	Cen A	+13:26:05.28	-42:56:32.64	10.71
60	Cen A	+13:26:10.56	-42:53:43.08	11.14
61	Cen A	+13:25:05.76	-43:10:30.36	11.57
62	Cen A	+13:25:28.08	-43:04:01.92	13.71
63	Cen A	+13:25:03.12	-42:56:24.72	13.84
64	Cen A	+13:25:32.88	-43:04:28.92	15.85
65	Cen A	+13:25:52.80	-43:05:46.32	20.97
66	Cen A	+13:25:05.04	-43:01:32.88	22.37
67	Cen A	+13:25:39.84	-43:05:01.68	23.62
68	Cen A	+13:25:32.40	-42:58:49.80	23.69
69	Cen A	+13:25:18.48	-43:01:15.96	24.05
70	Cen A	+13:25:10.56	-43:06:24.12	27.47
71	Cen A	+13:26:19.68	-43:03:19.08	30.51
72	Cen A	+13:25:19.92	-43:03:09.72	31.62
73	Cen A	+13:25:10.32	-42:55:09.48	37.62
74	Cen A	+13:26:00.72	-43:09:40.32	46.48
75	Cen A	+13:25:46.56	-42:57:02.88	55.91
76	Cen A	+13:25:35.52	-42:59:34.80	57.54
77	Cen A	+13:25:09.12	-42:58:58.80	58.10
78	Cen A	+13:25:10.32	-42:53:32.64	69.64

Table 3.6: Continued.

Number (1)	Galaxy (2)	RA(J2000) (3)	DEC(J2000) (4)	Luminosity (5)
79	Cen A	+13:25:12.96	-43:01:14.16	79.97
80	Cen A	+13:25:31.68	-43:00:02.88	87.42
81	Cen A	+13:25:35.28	-42:53:00.96	97.94
82	Cen A	+13:25:54.48	-42:59:25.44	105.59
83	Cen A	+13:25:07.68	-43:01:14.88	199.09
84	Cen A	+13:25:02.64	-43:02:43.08	255.53
85	Cen A	+13:25:42.00	-43:10:41.52	315.01
86	M81	+09:56:05.30	+69:06:43.53	2.01
87	M81	+09:55:37.26	+69:02:07.57	2.36
88	M81	+09:55:51.97	+69:07:39.18	4.83
89	M81	+09:55:22.05	+69:05:18.93	6.68
90	M81	+09:55:54.93	+69:00:56.03	35.33
91	M81	+09:55:47.00	+69:05:51.09	67.26
92	M81	+09:55:58.54	+69:05:26.04	70.40
93	M81	+09:55:49.80	+69:05:31.93	434.56
94	Maffei 1	+02:36:37.26	+59:39:15.50	5.41
95	Maffei 1	+02:36:30.84	+59:39:34.70	9.11
96	Maffei 1	+02:36:26.03	+59:39:06.91	16.22
97	Maffei 1	+02:36:36.50	+59:38:42.03	42.07
98	N3379	+10:47:50.47	+12:34:23.11	4.14
99	N3379	+10:47:51.57	+12:35:36.01	14.18
100	N3379	+10:47:54.20	+12:35:29.49	39.83
101	N3379	+10:47:50.47	+12:34:36.94	53.20
102	N3379	+10:47:50.33	+12:35:06.59	58.00
103	N3379	+10:47:51.08	+12:35:49.25	87.35
104	N3379	+10:47:52.77	+12:35:08.58	242.70
105	N3379	+10:47:50.19	+12:34:55.34	333.36
106	N3379	+10:47:52.65	+12:33:38.01	680.58
107	N4697	+12:48:32.94	-05:47:04.04	7.23
108	N4697	+12:48:33.63	-05:48:49.20	8.22
109	N4697	+12:48:29.13	-05:48:22.15	8.26
110	N4697	+12:48:34.64	-05:47:27.55	9.39
111	N4697	+12:48:26.52	-05:47:24.91	9.53
112	N4697	+12:48:35.80	-05:47:41.90	10.13
113	N4697	+12:48:37.60	-05:47:49.79	10.26
114	N4697	+12:48:34.68	-05:48:14.82	11.08
115	N4697	+12:48:37.16	-05:48:30.34	11.76
116	N4697	+12:48:28.04	-05:48:32.66	13.69
117	N4697	+12:48:40.86	-05:48:23.12	14.88
118	N4697	+12:48:41.66	-05:48:47.04	15.00

3 *LMXB dependence on the stellar density and velocity dispersion*

Table 3.6: Continued.

Number (1)	Galaxy (2)	RA(J2000) (3)	DEC(J2000) (4)	Luminosity (5)
119	N4697	+12:48:37.71	-05:47:29.32	16.78
120	N4697	+12:48:35.80	-05:46:40.69	17.44
121	N4697	+12:48:31.84	-05:48:38.70	23.44
122	N4697	+12:48:36.97	-05:47:32.61	23.97
123	N4697	+12:48:33.95	-05:48:34.46	25.58
124	N4697	+12:48:26.16	-05:47:29.50	26.29
125	N4697	+12:48:36.95	-05:48:10.80	30.36
126	N4697	+12:48:33.19	-05:49:12.85	40.98
127	N4697	+12:48:37.87	-05:46:52.81	42.12
128	N4697	+12:48:40.92	-05:47:31.44	42.31
129	N4697	+12:48:31.05	-05:48:28.66	46.15
130	N4697	+12:48:41.50	-05:47:37.25	46.82
131	N4697	+12:48:36.10	-05:48:33.61	60.54
132	N4697	+12:48:46.55	-05:48:12.02	75.50
133	N4697	+12:48:38.67	-05:47:46.88	91.24
134	N4697	+12:48:35.95	-05:45:51.79	91.79
135	N4697	+12:48:31.73	-05:48:46.73	97.43
136	N4697	+12:48:36.97	-05:48:01.04	110.29
137	N4697	+12:48:32.65	-05:48:51.11	125.21
138	N4697	+12:48:35.97	-05:47:56.56	150.11
139	N4697	+12:48:39.35	-05:47:30.48	168.46
140	N4697	+12:48:36.72	-05:47:31.89	178.73
141	N4697	+12:48:37.51	-05:47:43.40	192.56
142	N4697	+12:48:27.03	-05:49:25.25	206.76
143	N4697	+12:48:30.83	-05:48:36.93	308.63
144	N4697	+12:48:33.21	-05:47:41.90	455.00
145	N4697	+12:48:39.32	-05:48:07.22	474.28
146	N4278	+12:20:04.55	+29:18:19.33	7.97
147	N4278	+12:20:00.39	+29:17:46.37	8.53
148	N4278	+12:20:04.70	+29:16:07.46	9.19
149	N4278	+12:20:02.98	+29:18:14.97	9.78
150	N4278	+12:20:00.37	+29:17:22.08	11.84
151	N4278	+12:20:05.24	+29:16:01.51	12.03
152	N4278	+12:20:04.87	+29:16:01.73	15.23
153	N4278	+12:20:03.54	+29:16:17.50	17.76
154	N4278	+12:20:02.49	+29:16:24.65	18.28
155	N4278	+12:20:05.89	+29:18:21.35	18.72
156	N4278	+12:20:01.08	+29:17:23.52	21.70
157	N4278	+12:20:04.59	+29:16:15.51	22.01
158	N4278	+12:20:09.95	+29:17:40.59	24.65

Table 3.6: Continued.

Number (1)	Galaxy (2)	RA(J2000) (3)	DEC(J2000) (4)	Luminosity (5)
159	N4278	+12:20:05.07	+29:17:15.46	26.87
160	N4278	+12:20:06.33	+29:17:10.05	28.26
161	N4278	+12:20:08.14	+29:16:59.83	28.32
162	N4278	+12:20:00.28	+29:18:12.18	29.04
163	N4278	+12:20:01.85	+29:17:58.35	30.38
164	N4278	+12:20:05.24	+29:16:52.84	37.40
165	N4278	+12:20:02.00	+29:17:29.78	46.63
166	N4278	+12:20:03.73	+29:16:29.81	48.82
167	N4278	+12:20:07.16	+29:17:38.74	50.30
168	N4278	+12:20:04.53	+29:16:12.19	50.37
169	N4278	+12:20:00.32	+29:17:05.11	52.01
170	N4278	+12:20:03.77	+29:16:09.66	58.85
171	N4278	+12:20:08.04	+29:16:42.13	61.23
172	N4278	+12:20:09.15	+29:17:57.95	66.65
173	N4278	+12:20:04.11	+29:16:15.34	66.84
174	N4278	+12:20:08.07	+29:16:43.61	71.32
175	N4278	+12:20:08.85	+29:17:28.92	90.19
176	N4278	+12:20:08.39	+29:17:16.85	113.49
177	N4278	+12:20:05.70	+29:16:49.98	119.54
178	N4278	+12:20:08.15	+29:17:16.97	125.36
179	N4278	+12:20:05.95	+29:17:08.94	138.53
180	N4278	+12:20:07.71	+29:16:44.05	144.98
181	N4278	+12:20:06.82	+29:16:36.65	145.01
182	N4278	+12:20:05.24	+29:16:39.97	265.89
183	N4278	+12:20:04.23	+29:16:51.47	269.32
184	N4278	+12:20:03.44	+29:16:39.55	292.63
185	N4278	+12:20:07.76	+29:17:20.46	388.68

4 LMXB dependence on the stellar age

4.1 Introduction

The collective luminosity of LMXBs in a galaxy was found to closely follow the near-infrared light and the scaling relation of the LMXB population with the stellar mass has been obtained (Gilfanov 2004). However, a moderate scatter exists in these relations, suggesting that the specific frequency (number per unit stellar mass) of X-ray binaries is not universally constant among galaxies and secondary correlations may exist.

Obviously, among various candidates of the second order correlations one is with the age of the stellar population. Unlike high-mass X-ray binaries, LMXBs are found both in young and old galaxies. Given that the characteristic time scale for the stellar evolution of the donor star and for the orbital evolution of the binary are both in the Gyrs range, it is not surprising that younger and older galaxies differ in the LMXB content. For example, recently Kim & Fabbiano (2010) reported the evidence that younger galaxies may have a higher fraction of bright sources than the older ones. On the theoretical side, the population synthesis calculations by Fragos et al. (2008) predicts that the formation rate of LMXBs steadily decreases with time after 1 Gyr. This conclusion seems to have been supported by observations – based on the analysis of galaxies detected in the extended *Chandra* Deep Field South Lehmer et al. (2007) found that for optically faint early-type galaxies (where LMXBs dominate the X-ray emission), L_X/L_B increases with redshift over $z \sim 0.0 - 0.5$ range. Other observational facts, however, appear to challenge this conclusion. In an S0 galaxy NGC 5102, whose stellar population is younger than 1 Gyr, Kraft et al. (2005) found only two sources brighter than 10^{37} erg/s, which is three times less than the predicted number of 6. Bogdán & Gilfanov (2010a) reported similar results for two young elliptical galaxies, NGC 3377 and NGC 3585. Admittedly, both studies suffered from relatively low statistical significance of the results and therefore cannot be considered as a final argument. Similarly, the result of Lehmer et al. (2007) was not based on a direct determination of the age of the stellar environment (which was rather inferred from the redshift) and could have been contaminated by other effects (e.g. the rate of galaxy mergers).

It is obvious that more observational effort is needed in order to clarify this issue. However, progress in this direction is hampered by the difficulty in reliable determination of the age of stellar populations. In addition, significant fraction of LMXBs in elliptical galaxies resides in globular clusters are dynamically formed in two-body stellar interactions, rather than having primordial origins. In order to

investigate the age effects on the primordial population of LMXBs, globular cluster sources need to be identified and excluded from the analysis. To this end, reliable lists of globular clusters are needed, which are not available for large number of galaxies required for a statistically meaningful study.

By now, *Chandra* has observed large number of galaxies with different morphological types and ages. On the other hand, significant progress has been achieved in the accuracy of the age determination techniques and advanced spectroscopical methods have been applied to a large number of galaxies. This motivated us to undertake a systematic study of the dependence of properties of LMXB populations on the stellar age. Among such properties we consider the specific (per unit stellar mass) number and X-ray luminosity of LMXBs and their luminosity distributions. In our analysis we will take into account the possible contamination by the globular cluster sources to the degree allowed by the available globular cluster data.

The paper is structured as follows: In Sect. 4.2 we describe our selection criteria and the resulting sample. In Sect. 4.3 we describe the X-ray and near-infrared data preparation and analysis. In Sect. 4.4 we produce the X-ray luminosity function of various sub-groups of galaxies. In Sect. 4.5 we study the origin of the plausible ultra-luminous X-ray sources (ULXs) in our sample, and their correlation with the age. In Sect. 4.6 we discuss the correlation of the LMXB population with the stellar mass, the stellar age and the globular clusters. Sect. 4.7 is our discussion.

4.2 The sample

Our goal is to build the largest possible sample covering the widest possible range of the stellar age. The size of the sample, however, is limited by the content of the *Chandra* archive and by the published age determinations. Our sample selection criteria are the following. Firstly we selected all early-type (E/S0) galaxies available in the *Chandra* archive. We cross-correlated this list with publications on the stellar age determinations, leaving only galaxies for which reliable age determinations are available (see below). In the remaining galaxies we selected only the ones located within the distance ~ 25 Mpc – this ensures a source detection sensitivity of better than $5 \cdot 10^{37}$ erg/s in less than 150 ksec of *Chandra* observation. Then we chose massive systems with $L_K > 5 \cdot 10^{10} L_{K,\odot}$ to guarantee the presence of a statistically meaningful number of LMXBs ($\gtrsim 20$) above the *Chandra* sensitivity limit. Note that the selection of galaxies based on the number of detected sources (instead of the K-band luminosity) could have introduced a bias in our sample. Finally, we excluded galaxies with ongoing or very recent star formation since the stellar content in such galaxies is likely to be inhomogeneous.

In total we selected 20 galaxies with the integrated *K*-band luminosity ranging from $\sim 8 \cdot 10^{10}$ to $4 \cdot 10^{11} L_{K,\odot}$. The main properties of these galaxies are listed in Table 4.1 and 4.2. The *Chandra* detection sensitivity (L_{lim}), which is defined as the 0.6 incompleteness level (Sect. 4.3.3) of LMXBs in the study field (Sect. 4.3.1),

Table 4.1: The list of our galaxy sample I.

Galaxy	Type	Distance (Mpc)	N_{H} (10^{20} cm^{-2})	L_{K} ($10^{10} L_{\text{K},\odot}$)	M_*/L_{K} ($M_{\odot}/L_{\text{K},\odot}$)
(1)	(2)	(3)	(4)	(5)	(6)
N720	E5	24.1	1.54	16.28	0.86
N821	E6	24.1	6.39	9.12	0.82
N1052	E4	19.4	3.07	8.94	0.80
N1380	SA0	17.6	1.31	12.57	0.81
N1404	E1	21.0	1.36	18.73	0.85
N3115	S0	9.7	4.32	9.43	0.83
N3379	E1	10.6	2.75	7.92	0.83
N3585	E6	20.0	5.58	18.92	0.77
N3923	E4-5	22.9	6.21	29.90	0.82
N4125	E6	23.9	1.84	23.49	0.80
N4278	E1-2	16.1	1.77	7.87	0.78
N4365	E3	20.4	1.62	20.86	0.85
N4374	E1	18.4	2.60	24.94	0.83
N4382	SA0	18.5	2.52	27.06	0.76
N4472	E2	16.3	1.66	41.88	0.85
N4552	E0-1	15.3	2.57	10.82	0.83
N4636	E0-1	14.7	1.81	13.24	0.81
N4649	E2	16.8	2.20	32.44	0.85
N4697	E6	11.7	2.12	8.82	0.77
N5866	SA0	15.3	1.46	9.47	0.72

(1) – Galaxy name. (2) – Galaxy morphology type. (3) – Distance from surface brightness fluctuation (Tonry et al. 2001). (4) – Galactic column density (Dickey & Lockman 1990). (5) – Total K_{S} -band luminosity calculated from the total K_{S} -band magnitude from 2MASS Large Galaxy Atlas (Jarrett et al. 2003) and the distance adopted in this paper. (6) – K_{S} -band mass-to-light ratios derived from Bell & de Jong (2001), with $B - V$ colors from RC3 catalog (de Vaucouleurs et al. 1991).

Table 4.2: The list of our galaxy sample II.

Galaxy	r_e (arcmin)	D25 ($2a, 2b, \theta$)	M_V (mag)	N_{GC}	S_N
(1)	(2)	(3)	(4)	(5)	(6)
N720	1.20	4.7', 2.4', 140°	-21.74	660 ± 190 ^a	1.33 ± 0.38
N821	1.66	2.6', 1.6', 25°	-21.12	320 ± 45 ^b	1.14 ± 0.16
N1052	1.12	3.0', 2.1', 120°	-21.00	400 ± 45 ^c	1.59 ± 0.18
N1380	1.32	4.8', 2.3', 7°	-21.23	560 ± 30 ^d	1.81 ± 0.10
N1404	0.79	3.3', 3.0', 162.5°	-21.58	725 ± 145 ^e	1.69 ± 0.34
N3115	1.07	7.2', 2.5', 40°	-21.13	630 ± 150 ^f	2.22 ± 0.53
N3379	1.17	5.4', 4.8', 67.5°	-19.95	270 ± 69 ^g	2.84 ± 0.72
N3585	1.20	4.7', 2.6', 107°	-21.76	–	0.50 ± 0.15 ^h
N3923	1.66	5.9', 3.9', 50°	-22.11	2494 ± 286 ⁱ	3.57 ± 0.41
N4125	1.95	5.8', 3.2', 82.5°	-22.13	–	1.30 ± 0.50 ^h
N4278	1.15	4.1', 3.8', 27.5°	-20.96	1300 ± 300 ^f	5.35 ± 1.23
N4365	1.66	6.9', 5.0', 40°	-22.01	2511 ± 1000 ^j	3.95 ± 1.57
N4374	1.70	6.5', 5.6', 135°	-22.25	4301 ± 1201 ^k	5.39 ± 1.50
N4382	1.82	7.1', 5.5', 12.5°	-22.23	1110 ± 181 ^k	1.43 ± 0.23
N4472	3.47	10.2', 8.3', 155°	-22.68	7813 ± 830 ^k	6.61 ± 0.70
N4552	0.98	5.1', 4.7', 150°	-21.29	984 ± 198 ^k	2.99 ± 0.60
N4636	2.95	6.0', 4.7', 150°	-21.33	4200 ± 120 ^l	12.38 ± 0.35
N4649	2.29	7.4', 6.0', 105°	-22.38	4745 ± 1099 ^k	5.32 ± 1.23
N4697	2.40	7.2', 4.7', 70°	-21.16	1100 ± 400 ^m	3.78 ± 1.37
N5866	1.35	4.7', 1.9', 128°	-20.93	400 ± 100 ⁿ	1.69 ± 0.42

(1) – Galaxy name. (2) – Effective radius from B -band photometry in RC3 catalog. (3) – D25 region of major diameter ($2a$), minor diameter ($2b$), and position angle (θ) from RC3 catalog. For NGC 1404, NGC 3379, NGC 4125, NGC 4278, NGC 4382, and NGC 4552 the position angle is taken from K_S -band image. (4) – Absolute V -band magnitude calculated from m_V from RC3. (5) – Total number of GCs taken from literature. References – ^aKissler-Patig et al. (1996); ^bSpitler et al. (2008); ^cForbes et al. (2001); ^dKissler-Patig et al. (1997); ^eForbes et al. (1998); ^fHarris (1991); ^gRhode & Zepf (2004); ⁱSikkema et al. (2006); ^jForbes (1996); ^kPeng et al. (2008); ^lDirsch et al. (2005); ^mDirsch (1996); ⁿCantiello et al. (2007). (6) – The globular cluster specific frequency calculated from total number of GCs and total absolute V -band magnitude, except for two galaxies which are local S_N taken from ^hHumphrey (2009).

ranges from $\sim 4 \cdot 10^{36}$ to 10^{38} erg/s (Table 4.4). This ensures enough statistics of the point source number in each galaxy.

4.2.1 The stellar age

The most accurate and widely used method of the age determination of elliptical galaxies is the spectroscopic estimator, which compares observed strength of the absorption lines of age-sensitive elements with predictions from the simple stellar population (SSP) synthesis models. A number of such measurements for different galaxy samples are published in the literature, e.g., Trager et al. (2000); Kuntschner et al. (2001); Terlevich & Forbes (2002); Caldwell et al. (2003); Thomas et al. (2005); Denicoló et al. (2005); Sánchez-Blázquez et al. (2006); Annibali et al. (2007); Gallagher et al. (2008). What all these measurements have in common is that they analyzed the spectrum of the very small central region of the galaxy, usually corresponding to $r_e/8$, where r_e is the effective radius of the galaxy. As LMXBs are rare objects, their numbers inside $r_e/8$ detected in a typical *Chandra* observation of a typical galaxy are by far insufficient for any statistically meaningful analysis. On the other hand, in order to increase their numbers, LMXBs are collected from the region which size is comparable with the D25 diameter. Moreover, to avoid complications due to the central (weak) AGN, centrally peaked diffuse emission and source confusion, the central region of the size of \sim few arcsec is usually excluded from the X-ray point sources analysis. Thus, the LMXBs and age measurements are inevitably performed geometrically different, sometimes barely overlapping regions of the galaxy. Obviously, such analysis requires an assumption of homogeneity of the stellar population, which may not be fulfilled in all the cases.

In addition, there is a discrepancy (sometimes large) between different measurements. This discrepancy can have different origins. It may be the consequence of the complexity of the task, resulting from the differences in particular methods used by different authors, for example, difference in the procedure of correcting for the ionized gas emission, in the choice of absorption lines used for fitting or in the libraries of stellar population synthesis models. In some cases, these discrepancies may also be a consequence of the complexity of the stellar populations in the central regions of some galaxies.

It is known that among different factors contamination by the gas emission is one of the most important. Therefore for galaxies with more than one measurement, we chose the ones which treated this issue in a more rigorous way. With this in mind, we prioritized the age determination studies in the following order: 1) Annibali et al. (2007), 2) Sánchez-Blázquez et al. (2006), 3) Denicoló et al. (2005) and 4) Terlevich & Forbes (2002). These 4 papers present age determinations for all the 20 galaxies in our sample. The age measurements are summarized in Table 4.3, which for each galaxy the adopted age is listed.

4 *LMXB dependence on the stellar age*

Table 4.3: Different measurements of the galaxy age.

Galaxy	Age1 (Gyr)	Age2 (Gyr)	Age3 (Gyr)	Age4 (Gyr)	Adopted age (Gyr)
^Y N720			$3.0^{+0.5}_{-4.3}$	3.4	$3.0^{+0.5}_{-4.3}$
^Y N821		5.2 ± 1.5	$4.0^{+1.7}_{-3.5}$	7.2	5.2 ± 1.5
N1052	14.5 ± 4.2		$2.9^{+0.4}_{-8.8}$		14.5 ± 4.2
^Y N1380	4.4 ± 0.7				4.4 ± 0.7
^Y N1404				5.9	5.9
N3115		8.4 ± 1.1	$2.6^{+0.0}_{-0.6}$		8.4 ± 1.1
N3379		8.2 ± 1.1	$10.9^{+2.6}_{-2.8}$	9.3	8.2 ± 1.1
^Y N3585				3.1	3.1
^Y N3923			$2.6^{+0.5}_{-0.6}$		$2.6^{+0.5}_{-0.6}$
^Y N4125			$5.9^{+2.5}_{-3.0}$		$5.9^{+2.5}_{-3.0}$
N4278		12.5 ± 1.2		10.7	12.5 ± 1.2
N4365		7.9 ± 1.2	$3.6^{+3.7}_{-2.3}$		7.9 ± 1.2
N4374	9.8 ± 3.4	11.3 ± 1.3	$3.8^{+1.1}_{-2.7}$	11.8	9.8 ± 3.4
^Y N4382				1.6	1.6
N4472		9.6 ± 1.2		8.5	9.6 ± 1.2
^Y N4552	6.0 ± 1.4	12.4 ± 1.2		9.6	6.0 ± 1.4
N4636	13.5 ± 3.6	10.3 ± 1.3			13.5 ± 3.6
N4649		16.9 ± 2.3		11.0	16.9 ± 2.3
N4697	10.0 ± 1.4	5.9 ± 1.2		8.2	10.0 ± 1.4
^Y N5866				1.8	1.8

The order of ages are based on the priority of selection: 1 – Annibali et al. (2007), 2 – Sánchez-Blázquez et al. (2006), 3 – Denicoló et al. (2005), 4 – Terlevich & Forbes (2002). The measurements are in the central $r_e/8$ region. Galaxies marked by “Y” are young galaxies studied in Sect. 4.4.3, while the rest are relatively old.

4.2.2 The globular cluster content

To characterize the globular cluster content of a galaxy we use the globular cluster specific frequency (S_N), which is conventionally defined by the relation: $S_N = N_{GC}10^{0.4(M_V+15)}$ (Harris 1991). As this parameter is sensitive to the assumed distance to the galaxy, the sensitivity limit and the completeness of the optical data, we collected the most accurate measurements of the total number of GCs (N_{GC}) in our galaxies, and then computed S_N with the distances used in this paper. For two galaxies, NGC 3585 and NGC 4125, N_{GC} were not available and we used the local S_N from Humphrey (2009) as an approximation to its global value. All values of S_N are listed in Table 4.2.

4.3 Data analysis

4.3.1 Data preparation and source detection

Chandra observations of our sample galaxies are listed in Table 4.4. We reduced the data following the instructions in Sect. 2.1.1, with CIAO version 4.2 and CALDB version 4.2.1. The references used for correcting offsets between X-ray observations are marked with an asterisk in Table 4.4. In this study obtaining absolute Astrometry is unnecessary since we do not plan to correlate our X-ray source lists with any optical source list. The energy range, as usual, was limited to 0.5-8.0 keV.

To detect point sources we used CIAO task *wavdetect* with the parameters listed in Sect. 2.1.2. To avoid the source crowding problem and the bias of the incompleteness of LMXBs in the galaxy center we excluded the central $a = 5''$ ellipse region (with the eccentricity and position angle following D25). We define the region outside the central $5''$, inside D25 as the study field throughout this paper. The total number of point sources detected in the study field is listed in Table 4.5. To estimate the source counts and luminosities we followed the instructions in Sect. 2.1.3. We listed the faintest source detected in each galaxy in Table 4.4 and the total number of point sources above L_{lim} in Table 4.5.

4.3.2 The cosmic X-ray background sources

We used the full band (0.5-10 keV) $\log(N)$ - $\log(S)$ distribution of cosmic X-ray background (CXB) sources from Georgakakis et al. (2008) and converted the flux to the 0.5-8 keV band, assuming a power-law spectrum with a photon index of 1.4. The total number of CXB sources among all detected point sources, and point sources above L_{lim} in the study field are listed in Table 4.5 (The model was corrected by the incompleteness function of CXB sources derived in Sect. 4.3.3). In most galaxies CXB sources contribute less than 15% of the total X-ray population, while in NGC 3379 and NGC 4382 the contribution is a bit higher (25-30%), however the essential statistics sustains.

4 LMXB dependence on the stellar age

Table 4.4: *Chandra* observations.

Galaxy (1)	Observation ID (2)	Exposure (3)	L_{\min} (4)	L_{\lim} (5)
N720	492,7062,7372*,8448,8449	138.8	2.7	7.2
N821	4006,4408,5691,5692,6310, 6313*,6314	212.9	1.3	2.8
N1052	5910	59.2	3.1	6.3
N1380	9526	41.6	3.9	6.1
N1404	2942,4174*,9798,9799	114.5	2.4	11.7
N3115	2040,11268,12095*	153.2	0.34	0.70
N3379	1587,7073*–7076	337.0	0.06	0.42
N3585	2078,9506*	94.7	2.3	4.1
N3923	1563,9507*	102.1	2.6	6.3
N4125	2071	64.2	3.0	8.9
N4278	4741,7077–7081*	470.8	0.32	0.88
N4365	2015*,5921–5924,7224	195.8	1.0	2.5
N4374	803,5908*,6131	115.5	0.84	4.9
N4382	2016	39.7	3.5	6.3
N4472	321*,322,11274	89.6	0.58	5.6
N4552	2072	54.4	1.3	4.5
N4636	323,324,3926,4415*	209.8	0.13	3.9
N4649	785,8182*,8507	108.0	2.1	6.8
N4697	784,4727–4730*	193.0	0.41	0.83
N5866	2879	33.7	2.1	4.7

(1) – Galaxy name. (2) – *Chandra* observation ID. (3) – The total exposure time of *Chandra* observations. (4) and (5) – The 0.5-8 keV luminosity of the faintest source detected, and the 0.6 incompleteness level of LMXBs in the study field. The luminosity is in the units of 10^{37} erg/s.

As well known, the CXB source density is subject to field-to-field variations due to the cosmic variance. These variations limit the accuracy of the CXB level predictions based on the source counts in selected extragalactic fields to $\sim 10 - 30\%$, depending on the solid angle. As discussed in Sect. 4.5, the CXB contribution is relatively unimportant everywhere except for the bright end of the luminosity function, where the cosmic variance becomes the major limiting factor in our analysis.

4.3.3 X-ray incompleteness correction

The X-ray incompleteness functions of LMXBs and CXB sources were produced following Sect. 2.1.5. To estimate the incompleteness-corrected number of LMXBs in the study field in each galaxy, we did incompleteness correction for the number of all resolved point sources, assuming $K(L)$ for the field LMXBs, then subtracted the corresponding number of CXB sources, which is implemented in equation:

$$N_{\text{LMXB}} = \sum_{L_i > L_{\text{min}}}^{L_{\text{max}}} \frac{1}{K_{\text{LMXB}}(L_i)} - \int_{L_{\text{min}}}^{L_{\text{max}}} 4\pi D^2 \frac{dN_{\text{CXB}}}{dL} \frac{K_{\text{CXB}}(L)}{K_{\text{LMXB}}(L)} dL, \quad (4.1)$$

where $4\pi D^2 dN_{\text{CXB}}/dL$ equals to dN_{CXB}/dS , which is the $\log(N) - \log(S)$ distribution of the CXB sources. We listed the total number of CXB subtracted, incompleteness corrected LMXBs above L_{lim} in Table 4.5.

4.3.4 Near-infrared data analysis

We calculated the stellar mass in the study field, using the K_S -band luminosities as described in Sect. 2.2. Most images are background subtracted, except for NGC 821, that we obtained the background from adjacent regions. We also removed the contamination of bright fore/background point sources from images visually. We listed the derived K_S -band mass-to-light ratios in Table 4.1, and the stellar masses in Table 4.5.

4.4 The X-ray luminosity function of LMXBs

4.4.1 CXB contribution

Fig. 4.1 shows the combined luminosity distribution of all X-ray compact sources detected within the study fields of galaxies along with the predicted distribution of the CXB sources. It shows that the CXB contribution is relatively unimportant below $\log(L_X) = 39$, where the background AGN account for approximately 10% of the observed compact sources.

Due to quick declining of the shape of the LMXB XLF at $\log(L_X) \sim 38.5 - 39$, accurately accounting for the CXB contribution becomes crucial at $\log(L_X) \gtrsim 39$. There is an apparent tail of the observed source counts in this luminosity

4 LMXB dependence on the stellar age

Table 4.5: Statistics of point sources in the study field.

Galaxy	N_X^{total}	$N_{\text{CXB}}^{\text{total}}$	$N_X^{L_{\text{lim}}}$	$N_{\text{CXB}}^{L_{\text{lim}}}$	$N_{\text{LMXB}}^{L_{\text{lim}}}$	L_K	M_*
(1)	(2)	(3)	(4)	(5)	(6)	(7)	(8)
N720	79	5.9	60	4.8	60.8	14.39	12.37
N821	39	3.3	38	3.1	36.0	7.02	5.76
N1052	41	2.5	35	2.2	35.4	7.42	5.93
N1380	36	3.9	28	3.4	28.0	10.99	8.90
N1404	33	3.6	18	2.5	17.9	15.14	12.87
N3115	99	11.1	89	10.2	82.8	8.51	7.06
N3379	95	23.4	87	22.9	65.8	6.89	5.72
N3585	59	6.1	56	5.8	53.9	15.73	12.11
N3923	105	10.8	83	9.8	89.6	26.36	21.61
N4125	42	8.2	27	6.6	24.2	20.98	16.78
N4278	177	16.3	160	14.9	154.2	6.71	5.24
N4365	244	23.9	213	22.5	201.1	18.87	16.04
N4374	133	18.1	88	13.9	91.5	22.33	18.53
N4382	52	13.5	44	12.3	33.1	25.14	19.11
N4472	238	26.3	171	24.0	171.6	39.71	33.76
N4552	94	10.4	68	7.6	70.7	9.07	7.52
N4636	123	12.2	82	9.1	83.6	11.39	9.22
N4649	236	15.0	149	10.7	168.5	28.97	24.62
N4697	120	22.4	107	21.4	85.9	7.96	6.13
N5866	29	3.1	23	2.7	21.5	8.45	6.09
Total	2074	240.0	1626	210.4	1576.1	312.0	255.4

(1) – Galaxy name. (2) and (4) – Number of all resolved X-ray point sources and sources brighter than L_{lim} . (3) and (5) – Predicted number of CXB sources among (2) and (4). (6) – Total number of LMXBs above L_{lim} after incompleteness correction and background subtraction. (7) and (8) – Total K_S -band luminosity and stellar mass (in units of $10^{10} L_{K,\odot}$ and $10^{10} M_\odot$) in the study field.

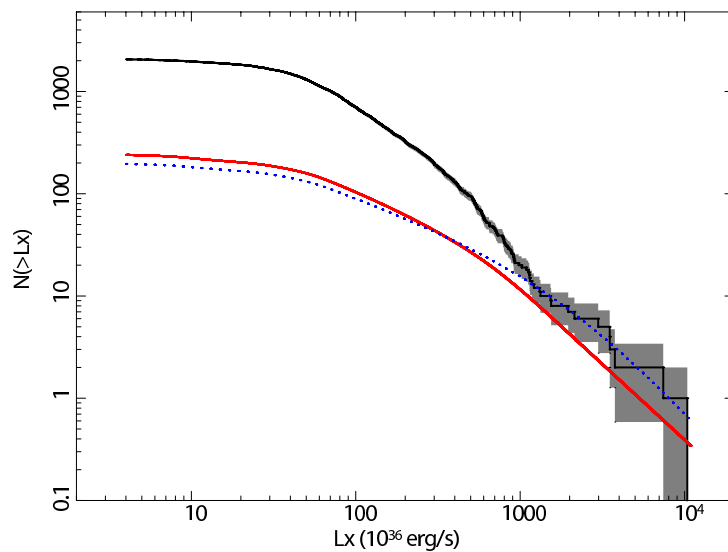


Figure 4.1: The observed cumulative distribution of all resolved point sources in all galaxies. The distribution is not corrected for incompleteness or the contribution of CXB sources. The shaded area shows 1σ Poissonian uncertainty. The thick solid and dotted lines show the predicted distribution of CXB sources based on the $\log(N) - \log(S)$ from Georgakakis et al. (2008) and Moretti et al. (2003) respectively.

range, which slope is similar to the slope of the predicted distribution of CXB sources. Its normalization, however, is somewhat higher than predicted by the CXB $\log(N) - \log(S)$ from Georgakakis et al. (2008). Quantitatively, we detected 20 sources above 10^{39} erg/s, while 11.6 background AGN in these fields is predicted based on Georgakakis et al. (2008). The Poissonian predicts a moderately low probability of $\sim 1.6 \cdot 10^{-2}$ for such a deviation solely due to random fluctuations. We also checked the predictions of the CXB $\log(N) - \log(S)$ determined by Moretti et al. (2003) and found that it can fully account for the observed bright sources, as shown by the dotted line in Fig. 4.1. In computing this prediction, we used the soft band (0.5-2 keV) counts and converted them to the 0.5 – 8 keV band, as described in Zhang et al. (2011). Comparing the two predictions, we should mention that the more recent work of Georgakakis et al. (2008) is based on a larger sample of sources detected in a larger number of *Chandra* surveys, and its results are in good agreement with another recent study by Kim et al. (2007). Moreover, converting the soft band flux from Moretti et al. (2003) into 0.5-8 keV highly depends on the assumed spectrum of CXB sources, for example, changing the photon index from 1.4 to 1.9 makes ~ 1.5 times of difference. Thirdly, the numbers of bright sources detected outside the D25 region of galaxies tend to be in a better agreement with the prediction of the $\log(N) - \log(S)$ by Georgakakis et al. (2008) (see below). For this reason we decided to accept Georgakakis et al. (2008) as our default CXB model. The origin of the bright sources will be further discussed in Sect. 4.5.

4.4.2 Corrected luminosity functions

The CXB subtracted and incompleteness corrected cumulative X-ray luminosity function (XLF) of compact X-ray sources in each galaxy are plotted in Fig. 4.2. As low-mass X-ray binaries are nearly the only type of compact X-ray sources in early-type galaxies capable of emitting at the $\log(L_X) \gtrsim 36$ luminosity level, the distributions shown in Fig. 4.2 can be regarded as luminosity functions of low-mass X-ray binaries in these galaxies. The XLFs have been normalized to unit stellar mass in the study field. It is clear that all the XLFs have a similar shape, which is broadly consistent with the average XLF of low-mass X-ray binaries in nearby galaxies obtained by Gilfanov (2004) (plotted with the thick line in the figure). On the other hand, a notable scatter of more than a factor of two exists for the normalization, which is a manifestation of the scatter in the LMXB - stellar mass relation, as discussed below.

To construct combined XLF of all galaxies with different detection sensitivity, we followed the method described in Zhang et al. (2011). The cumulative and differential forms of our XLF are plotted in Fig. 4.3. We fitted the combined XLF

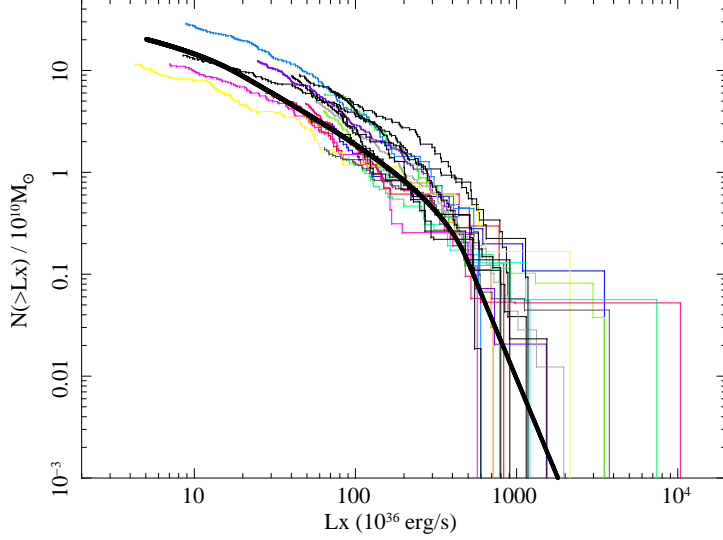


Figure 4.2: Cumulative XLFs of low-mass X-ray binaries in galaxies of our sample. The luminosity functions are CXB subtracted and incompleteness corrected, and normalized to the stellar mass of the host galaxy. They are plotted above corresponding L_{lim} of each galaxy. The solid line is the average XLF of LMXBs in nearby galaxies from Gilfanov (2004).

with the template introduced in Gilfanov (2004):

$$\frac{dN}{dL_{36}} = \begin{cases} K_1 (L_{36}/L_{b,1})^{-\alpha_1}, & L_{36} < L_{b,1} \\ K_2 (L_{36}/L_{b,2})^{-\alpha_2}, & L_{b,1} < L_{36} < L_{b,2} \\ K_3 (L_{36}/L_{\text{cut}})^{-\alpha_3}, & L_{b,2} < L_{36} < L_{\text{cut}} \\ 0 & L_{36} > L_{\text{cut}} \end{cases} \quad (4.2)$$

where $L_{36} = L_X/10^{36}$ erg/s and normalizations $K_{1,2,3}$ are related by:

$$\begin{aligned} K_2 &= K_1 (L_{b,1}/L_{b,2})^{\alpha_2}, \\ K_3 &= K_2 (L_{b,2}/L_{\text{cut}})^{\alpha_3}. \end{aligned}$$

The value of the high luminosity cut-off was fixed at $L_{\text{cut}} = 5 \cdot 10^4$. We performed Maximum-likelihood fitting to the unbinned data. Our best-fit parameters are: $\alpha_1 = 1.00 \pm 0.09$, $\alpha_2 = 2.08^{+0.07}_{-0.06}$, $\alpha_3 = 3.67^{+1.06}_{-0.55}$, $L_{b,1} = 53^{+4.6}_{-4.2}$ and $L_{b,2} = 582^{+107}_{-76}$. The normalization is $K_1 = 1.1 \pm 0.3$ per $10^{11} M_{\odot}$.

The combined XLF obtained in this study is broadly consistent with the average LMXB XLF obtained by Gilfanov (2004) (cf. dotted line in Fig. 4.3). The XLF of the sources in our sample appears to be somewhat flatter in the bright end of $\log(L_X) \gtrsim 38.5$, having more luminous sources. The tail of the very bright sources with $\log(L_X) \gtrsim 39$ is discussed in Sect. 4.5.

4 LMXB dependence on the stellar age

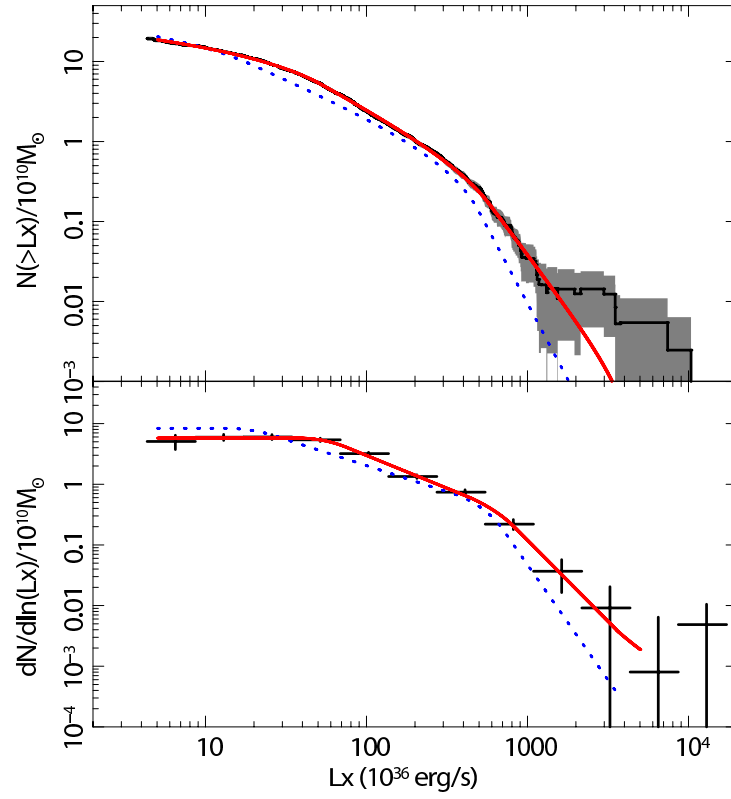


Figure 4.3: The combined luminosity distribution of LMXBs in our sample. The distributions are CXB subtracted and incompleteness corrected, as described in the text. The shaded area in the upper panel indicates the 1σ Poissonian uncertainty. The solid lines show the best-fit model with two breaks, the dotted lines show the average LMXB XLF from Gilfanov (2004). See Sect. 4.5 for the discussion and caveats of the bright luminosity tail.

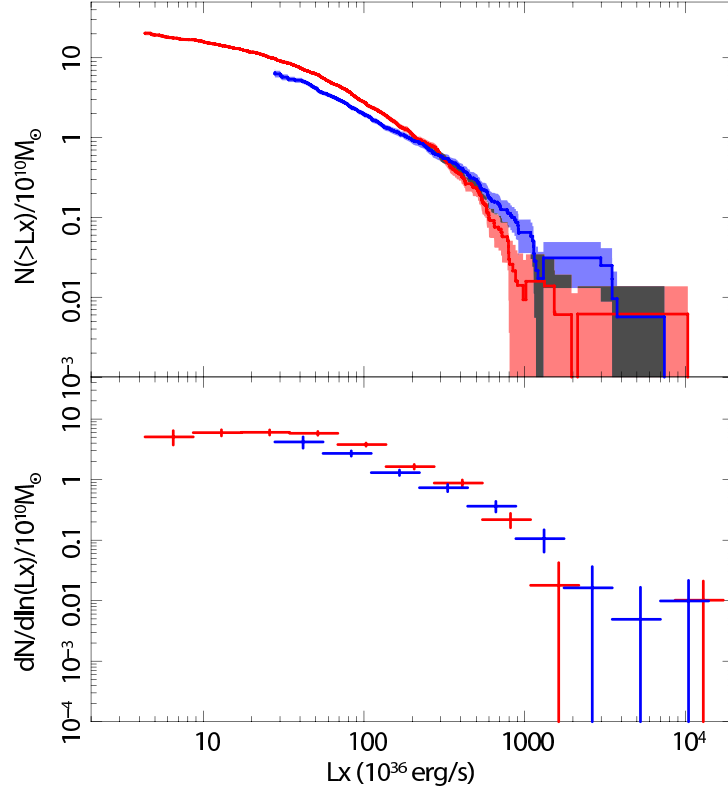


Figure 4.4: The X-ray luminosity functions of LMXBs in the young (blue histogram) and old (red) galaxies. The shaded areas in the upper panel shows the 1σ Poissonian uncertainty.

4.4.3 Young and old galaxies

In order to investigate the age dependence of the LMXB populations, we divided the galaxies into relatively young (<6 Gyr) and old (>6 Gyr) sub-groups. Each group contains 10 galaxies which are marked correspondingly in Table 4.3. The study regions in young and old galaxies cover a total solid angle of 125.9 and 251.6 arcmin² respectively, with a total stellar mass of 1.24 and $1.32 \cdot 10^{12} M_{\odot}$.

We constructed the combined XLF of each group and have them plotted in Fig. 4.4. In general the old galaxies have deeper *Chandra* observations which have reached a sensitivity of $5 \cdot 10^{36}$ erg/s, while the young group has a sensitivity of few times 10^{37} erg/s. The overall XLF shape of the young galaxies is flatter than that of the old ones, i.e. there are fewer faint and more bright sources in the younger galaxies. This behavior is in agreement with findings of Kim & Fabbiano (2010).

4 LMXB dependence on the stellar age

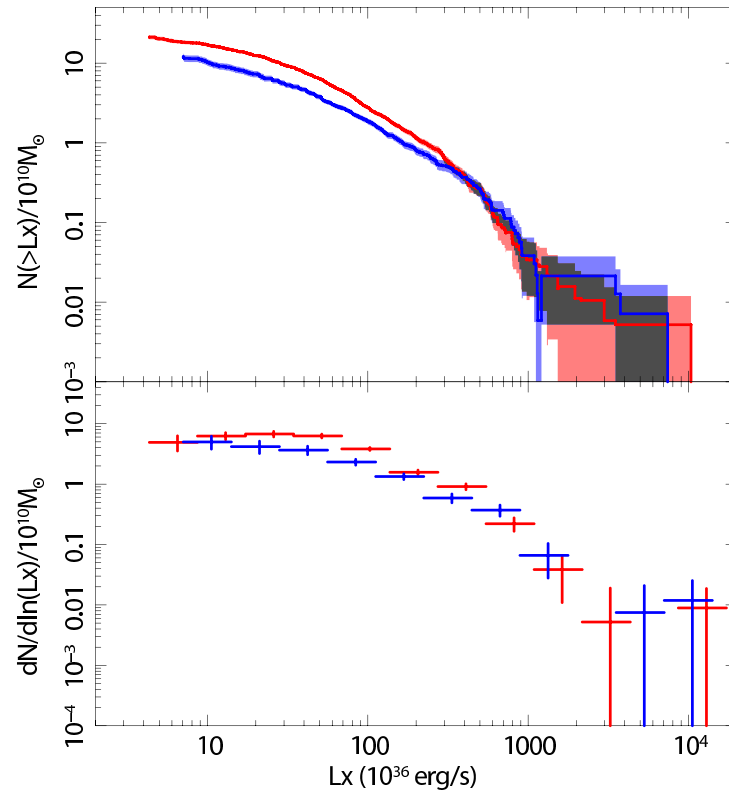


Figure 4.5: The X-ray luminosity functions of LMXBs in galaxies with high (red histogram) and low (blue) globular cluster content (see text for details). The shaded areas in the upper panel shows the 1σ Poissonian uncertainty.

4.4.4 Galaxies with high and low GC content

As X-ray binaries in globular clusters and in the field have different origin, ideally, they should be separated from each other when studying the dependence of the LMXB population on the stellar age. However, due to the limitations of the optical data, we have no possibility to directly identify and remove LMXBs located in globular clusters. But we can investigate the effect of the globular cluster population of the galaxy from its total LMXB content. To characterize the former we use the globular cluster specific frequency (S_N), introduced earlier in this chapter.

The value of $S_N = 2.5$ divides our sample into two halves and we used it as a boundary to separate globular cluster richer and poorer galaxies. The resulting XLFs are shown in Fig. 4.5. As expected (from the age dependence of the XLF and the general correlation between age and S_N), the XLF of galaxies with higher globular cluster content is steeper than the ones with lower S_N . However, they appear to be rather consistent at the bright end with $\log(L_X) \gtrsim 38.5 - 39$.

4.5 The nature of the luminous X-ray sources

In total, we detected 20 sources above 10^{39} erg/s. Subtracting from this number the 11.6 background AGN predicted from the Georgakakis et al. (2008) CXB $\log(N) - \log(S)$, we obtained that $\sim 8 - 9$ sources should be luminous LMXBs in the galaxies from our sample. Similarly, for $L_X > 2 \cdot 10^{39}$ erg/s we obtained $\sim 2 - 3$ LMXBs (7 observed, 4.2 predicted). Assuming Poissonian distribution, these numbers correspond to moderately low probabilities of being a result of pure statistical fluctuations: $\sim 1.6 \cdot 10^{-2}$ and 0.13 for the two luminosity ranges correspondingly. Thus, the statistical significance of the excess of the number of luminous sources above the predicted number of background AGN is between moderate (for sources with $L_X > 10^{39}$ erg/s) and low (for sources with $L_X > 2 \cdot 10^{39}$ erg/s).

However, it is well known that the CXB source counts produce somewhat different results in different sky fields due to the cosmic variance. The amplitude of these variations depends primarily on the considered angular scales. For this reason, results of extragalactic surveys should be used with some caution in predicting the number of background AGN in individual fields. On one hand, we do not expect this effect to be particularly strong in the combined LMXB XLFs shown in Figs. 4.3 and 4.4 as we combined the data of 20 galaxies distributed over the extragalactic sky. However, the slope of the bright tail of the luminosity distribution in Fig. 4.1 is identical to the slope of the CXB $\log(N) - \log(S)$. The strong slope change in the CXB subtracted XLF at $\log(L_X) \sim 39$, where the CXB contribution becomes significant (Fig. 4.3), are highly suggestive that the majority of the sources with $\log(L_X) \gtrsim 39$ may be background AGN.

In order to investigate the factor of cosmic variance, we checked the source numbers in the background regions outside the study fields but within $10' \times 10'$ of the *Chandra* FOV. In total 38 sources with $\log(L_X) > 39$ were detected, while

the CXB $\log(N) - \log(S)$ of Georgakakis et al. (2008) predicts 47.8 background AGN. These two numbers are consistent within $\sim 1.5\sigma$ and suggest that the CXB prediction from Georgakakis et al. (2008) is applicable to the combined data of our sample.

For further confirmation we produced a stacked radial source density profile of sources in all galaxies. For each source, its distance to the center of the galaxy was determined in units of the D25 radius. From this analysis we excluded the four galaxies having the largest angular extent (NGC 4472, NGC 4649, NGC 4697 and NGC 4374) in order to be capable of computing the profile to larger radii. The resulting profiles in different luminosity ranges are plotted in Fig. 4.6. In each panel we plot de Vaucouleurs profile (de Vaucouleurs 1948). We added to the de Vaucouleurs profile the constant CXB source density, calculated according to Georgakakis et al. (2008). The upper panel shows the radial distribution of moderately luminous sources with $L_X > 10^{38}$ erg/s and demonstrates that their radial distribution is well described by the $r^{1/4}$ de Vaucouleurs law. Note that sources with $\log(L_X) > 38$ are complete in our sample. For sources brighter than 10^{39} erg/s and $2 \cdot 10^{39}$ erg/s (middle and lower panels in the figure), poor statistics makes the results consistent both with the de Vaucouleurs profile, and a flat CXB distribution.

Furthermore, we checked the 20 sources detected with $L_X > 10^{39}$ erg/s individually, looking for their identifications in the NASA Extragalactic Database. The results are presented in Table 4.6. In the table, we list young and old galaxies separately. Among the 20 sources 13 are detected in the young galaxies and 7 in the old ones, with the CXB sources predictions being 5.6 and 6.0 respectively. Taken at the face value, this may suggest that young group has significantly more ULXs (~ 7) than the old group (~ 1). To crosscheck we tried to find the properties of all the sources from NED. 8 of them have optical counterparts – 3 are confirmed to be background quasars, 1 is matched with a background galaxy, and 4 are found in globular clusters. The brightest 3 ULXs ($> 2 \cdot 10^{39}$ erg/s) are all found in the young galaxies.

Thus, in our sample of 20 early-type galaxies we have detected 20 luminous sources with $L_X > 10^{39}$ erg/s, of which $\sim 8 - 9$ may be LMXBs. According to the definition, these sources can be classified as ultra-luminous X-ray sources (ULXs). In the view of the fact that ULXs are believed to be associated with star-forming environments, reliable detection of ULXs in early-type galaxies may be of considerable importance for our understanding of their nature. The number of luminous sources in old galaxies is consistent with the CXB prediction (7 observed, 6 predicted) and their LMXB XLF appears to be entirely normal. The young galaxies, however, may have a small sub-population of luminous sources, with luminosities exceeding 10^{39} erg/s and, possibly, reaching $\sim \text{few} \times 10^{39}$ erg/s. However, the statistical significance of this result is rather low and a further increase of the sample is needed before a reliable conclusion can be made. A possible alternative way is to prove the association of some of the ultra-luminous sources with the galaxies using astronomical methods.

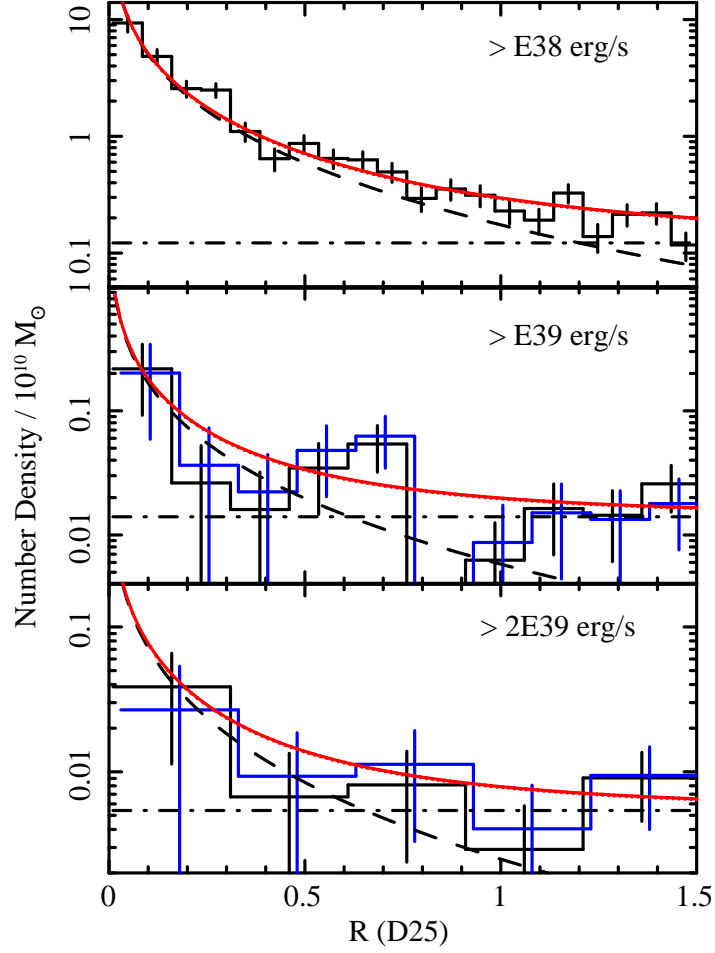


Figure 4.6: The radial density profiles of stacked X-ray sources in different luminosity range for all galaxies except for NGC 4472, NGC 4649, NGC 4697 and NGC 4374. The blue histogram refers to young galaxies. The dashed line following $r^{1/4}$ law represents the K -band density profile with arbitrary normalization, the dash-dotted line is the CXB level and the solid line is the sum of K -band density and the CXB.

4 LMXB dependence on the stellar age

Table 4.6: Sources brighter than 10^{39} erg/s in our sample.

Galaxy	RA(J2000)	DEC(J2000)	Luminosity	opt.
Young Galaxies				
N720	+01:53:01.12	-13:44:19.53	1.15 ± 0.06	–
N1380	+03:36:26.56	-34:56:58.96	1.09 ± 0.09	–
	+03:36:25.25	-34:59:18.09	3.51 ± 0.04	–
N1404	+03:38:51.99	-35:35:59.93	1.14 ± 0.07	–
	+03:38:54.78	-35:35:00.96	1.21 ± 0.07	–
N3923	+11:50:58.65	-28:49:13.16	1.31 ± 0.08	–
	+11:51:09.54	-28:48:00.67	2.98 ± 0.12	–
	+11:51:06.22	-28:46:49.91	3.50 ± 0.13	QSO
N4125	+12:08:07.46	+65:10:28.61	7.41 ± 0.23	–
N4382	+12:25:20.32	+18:13:01.41	1.12 ± 0.09	–
	+12:25:17.17	+18:13:46.52	3.76 ± 0.18	QSO
N4552	+12:35:45.77	+12:33:02.46	1.14 ± 0.06	cl
	+12:35:41.22	+12:34:51.43	1.18 ± 0.06	cl
Old Galaxies				
N3379	+10:47:50.01	+12:34:56.77	2.14 ± 0.03	cl
N4365	+12:24:26.36	+07:16:53.55	1.53 ± 0.05	–
N4374	+12:25:11.92	+12:51:53.81	10.38 ± 0.16	QSO
N4472	+12:29:41.00	+07:57:44.46	1.96 ± 0.08	–
	+12:29:34.46	+07:58:51.63	1.33 ± 0.06	G
	+12:29:42.33	+08:00:07.96	1.02 ± 0.05	cl
N4649	+12:43:46.90	+11:32:34.19	1.54 ± 0.06	–

Columns are the host galaxy, coordinates, luminosity in units of 10^{39} erg/s and the optical counterpart from NED (QSO: Quasi-stellar object, cl: globular cluster, G: galaxy).

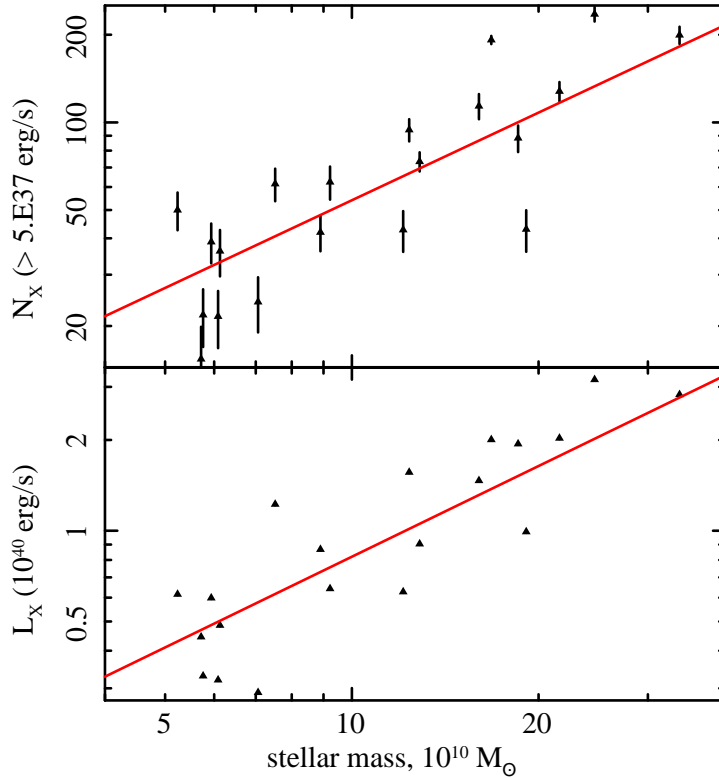


Figure 4.7: Relation of the total number (upper panel) and luminosity (lower panel) of LMXBs in the study field with the stellar mass.

4.6 The LMXB – stellar mass relation

In this section we revisit the scaling relation of LMXBs to the stellar mass. The total number and collective luminosity of LMXBs in the study field above $5 \cdot 10^{37}$ erg/s (Eq.(4.1)) for all the galaxies were computed and correlated with the corresponding stellar mass in Fig. 4.7. The combined XLF of our sample gives the corresponding values of $N_X = 54.0$ and $L_X = 8.2 \cdot 10^{39}$ erg/s per $10^{11} M_\odot$, which is ~ 1.4 times of what is from Gilfanov (2004) – 37.8 and $5.8 \cdot 10^{39}$ erg/s. We estimated the average LMXB - stellar mass relation from the best-fit XLF of the combined sample (Sect. 4.4), which are shown with the solid lines in the figure. The *rms* dispersion in logarithmic scale of the data around the model is 0.19 dex for N_X and 0.16 dex for L_X .

As we have mentioned, the scatter can be related to the difference in the stellar age. Another factor may be the large fraction of dynamically formed GC-LMXBs in the galaxies, which numbers do not directly correlate with the stellar mass. In the next section we will study the significance of these two factors.

4 LMXB dependence on the stellar age

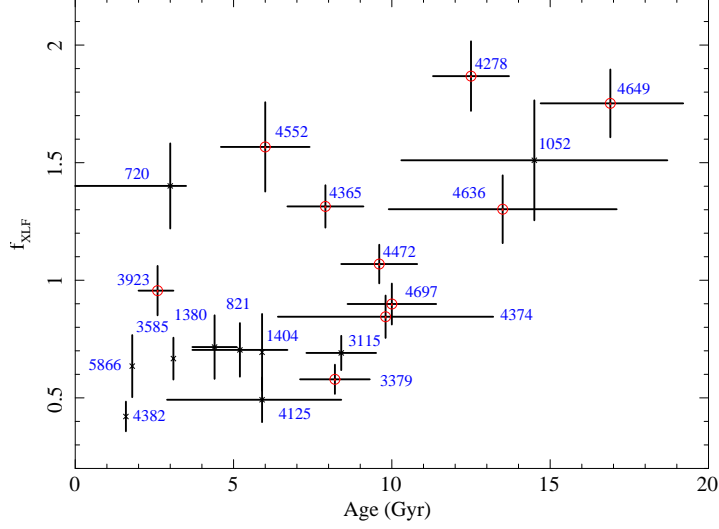


Figure 4.8: Correlation of the normalization of the XLF, f_{XLF} (Eq. 4.3), with the stellar age. Circles mark galaxies with a larger S_N (>2.5).

4.6.1 Correlation of LMXBs with the age and the GC content

To describe the number of LMXBs per unit stellar mass in each galaxy, we introduced a quantity f_{XLF} , which is the XLF normalization computed from the number of resolved LMXBs above L_{lim} , assuming the average XLF shape (Sect. 4.4), and normalized to the stellar mass:

$$f_{\text{XLF}} = \frac{N_{\text{X}}^{L_{\text{lim}}} - N_{\text{CXB}}^{L_{\text{lim}}}}{M_* \times \int_{L_{\text{lim}}} F(L) K_{\text{LMXB}}(L) dL}, \quad (4.3)$$

where $N_{\text{X}}^{L_{\text{lim}}}$ and $N_{\text{CXB}}^{L_{\text{lim}}}$ are the numbers of detected X-ray sources and predicted CXB sources (Table 4.5), $F(L)$ the best-fit differential XLF and $K_{\text{LMXB}}(L)$ the incompleteness function of LMXBs in the given galaxy. Using this description for the relative excess/deficit of LMXBs is strongly under the assumption that the XLF shape of LMXBs in each galaxy is the same, however, it benefits in statistics by guaranteeing the largest number of LMXBs involved in the calculation.

We plotted the correlation of f_{XLF} with the stellar age in Fig. 4.8. There is a clear trend that f_{XLF} increases with the stellar age. f_{XLF} for the oldest galaxy NGC 4649 is more than 4 times of that for the youngest galaxy NGC 4382. Using the Spearman Rank-Order Correlation test we got a correlation coefficient $r_s = 0.57$, which corresponds to a two-sided p -value of 0.009 in student's t -distribution, which indicates a moderately strong correlation. There is rather large scatter in the plot – some young galaxies can also have large values of f_{XLF} (e.g. NGC 720 and NGC 4552). Contamination of GC-LMXBs may be part of the reason, since

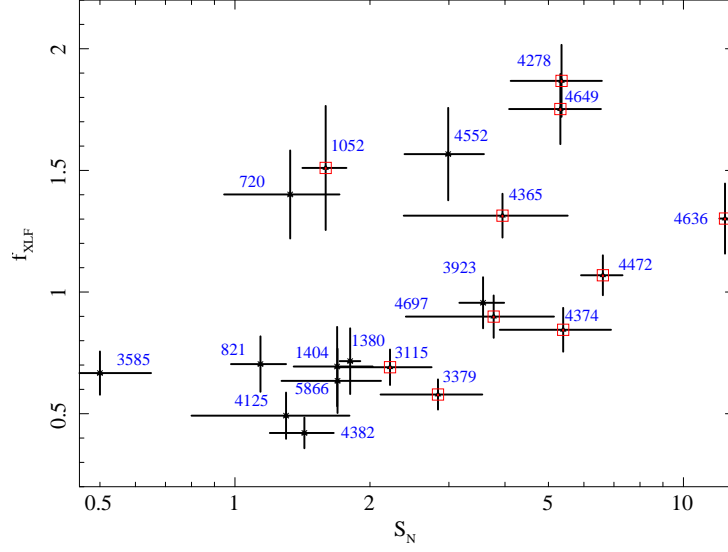


Figure 4.9: Correlation of f_{XLF} with the specific frequency of GC. Squares mark the old galaxies (stellar age > 6 Gyr), while the rest are young.

some of such galaxies (NGC 4552, NGC 4365 and NGC 4278) have high values of S_N .

The average values of f_{XLF} are 0.74 ± 0.07 for the young sample and 1.04 ± 0.06 for the old sample. The total number of LMXBs per unit stellar mass above $5 \cdot 10^{37}$ erg/s in the young sample is 4.18 ± 0.27 , which is $\sim 2/3$ of that in the old (6.27 ± 0.26). The prediction from the average XLF is 5.4.

The correlation of f_{XLF} with S_N is plotted in Fig. 4.9. Despite notable scatters these two parameters are correlated with the Spearman's test of $r_s = 0.53$ and the associated probability of $p = 0.017$. The specific number of sources f_{XLF} increases with S_N , which is consistent with previous results, for example with Boroson et al. (2011). Boroson et al. (2011) suggested that at least part of the scatter in this correlation may due to the uncertainty in S_N , which can also be our case. Besides, we noticed that some most largely dispersed galaxies have older stellar age (NGC 1052, NGC 4649 and NGC 4278). Similar to how S_N affects the LMXB - age correlation, age also impacts the LMXB - S_N correlation.

Finally, Fig. 4.10 shows that there is strong correlation between S_N and the stellar age (Spearman test results are $r_s = 0.63$ and $p = 0.003$). This is not unexpected as more GCs are expected in older galaxies, since more massive clusters are formed in larger star bursts at larger redshifts (Bastian 2008). A significant fraction of these will survive through the following evolution of the galaxy (Fall & Zhang 2001). Existence of such a correlation must be taken into account when interpreting the dependence of the LMXB population on the stellar age and the globular cluster content of the galaxy.

4 LMXB dependence on the stellar age

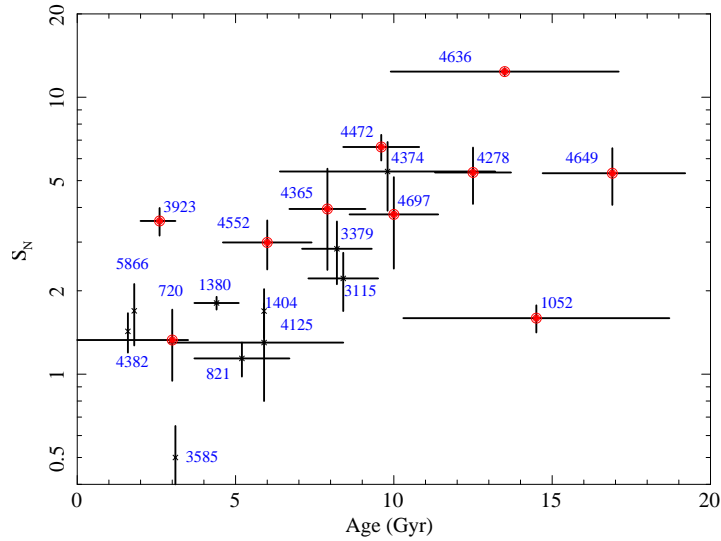


Figure 4.10: Correlation of the GC specific frequency with the stellar age. Filled circles mark galaxies with larger f_{XLF} .

4.7 Discussion

The main goal of this paper is to study the dependence of the population of low-mass X-ray binaries on the stellar age. To this end, we have collected 20 nearby early-type galaxies which were observed by *Chandra* to sufficient depth and had the stellar age measured. We have found a correlation between the specific number (per unit stellar mass) of LMXBs and the stellar age. This correlation is shown in Fig. 4.8 which demonstrates that in general older galaxies possess more LMXBs than the younger ones. We also found clear evolution of the X-ray luminosity function with the age. The younger galaxies tend to have more bright sources and fewer faint sources than the old galaxies.

The main difficulty of this study is the uncertainties and limitations of the stellar age determinations. These uncertainties are the reason for the discrepancy between the values of the stellar age determined by different authors. Secondly, the age measurements used in this paper refer to the central few arcsec of the galaxy ($r_e/8$). Although the stellar content in elliptical galaxies is expected to be more uniform than in late-type galaxies, inhomogeneities are known to exist and in some cases are known to be rather large. In order to increase the number of sources, the X-ray measurements are carried out over a much larger region of the galaxy than where the age was determined. This may introduce significant contamination to the LMXB – age correlation produced in this paper. Nevertheless, this is the first study of this kind and it is unlikely that spatially resolved age measurements for any meaningful number of galaxies will become available in the near future.

Therefore, we consider this risk worth taking and justified.

To investigate this further, we collected from the literature the results of long-slit spectroscopy of galaxies in our sample. We have found that some galaxies may have more complicated structure of the stellar population than a single-aged population, and that the true stellar ages may be different from the values used in this paper. We discuss these results below galaxy by galaxy. NGC 720 was found to form by a merger of an old (13-5 Gyr) small-scale spheroid and a younger (5-2.5 Gyr) large-scale disk component (Rembold et al. 2005). Thus the average stellar age of NGC 720 should be older than 3 Gyr used in this paper. In NGC 821 the central stellar population was found to be young (~ 4 Gyr), while the age increases outwards and reaches 12 Gyr at one effective radius (Proctor et al. 2005). Thus the average age is likely to be older than 5 Gyr. NGC 4125 was found to experience a recent dissipational merger event, thus young stellar population quite possibly exists in the galaxy (Pu et al. 2010). And NGC 4365 is very much likely to be older than 7.9 Gyr, that the decoupled core and the main body of the galaxy was found to have the same age of ~ 14 Gyr (Davies et al. 2001). With these results, in Fig. 4.8 the data point of NGC 720, NGC 821 and NGC 4365 may shift to the right, while NGC 4125 may shift to the left.

Both the stellar age and the globular cluster content of the galaxy are known to affect its LMXB population. Existence of a clear correlation between these two quantities does not allow to separate the effects of these two factors. Furthermore, the populations of the dynamically formed systems in globular clusters are also obviously age-dependent, but their age dependence is different from the field LMXBs, due to different formation mechanism and evolution histories. The lack of the statistically complete globular cluster lists for the majority of the galaxies in our sample did not allow us to identify and separate the LMXBs associated with globular clusters and to study the age dependence in the populations of primordial LMXBs and the dynamically formed systems. This limitation is gradually diminished as more and more high quality optical studies of the globular cluster populations in nearby galaxies become available.

5 Conclusions

We have studied the environmental dependence of populations of low-mass X-ray binaries (LMXBs) in early-type galaxies. This includes dependence on the stellar density (e.g. globular clusters and galactic nuclei vs. field), velocity dispersion (globular clusters vs. galactic nuclei) and the age of the stellar population. The study is based on *Chandra* X-ray and 2MASS near-infrared data, as well as the results of HST and ground based optical observations. Our analysis has reached an accuracy far greater than what has been achieved previously, and has extended the luminosity range accessible for quantitative analysis to the luminosity of $\sim 10^{35}$ erg s $^{-1}$, unprecedented for LMXB studies in external galaxies.

Based on a sample of ~ 25 galaxies containing ~ 3000 compact X-ray sources we found that the luminosity distributions of LMXBs in different stellar environments are all different. LFs of globular cluster and field LMXBs differ throughout the entire luminosity range. The fraction of faint ($\log(L_X) < 37$) sources among the former is ~ 4 times smaller than the sources among the latter. The LF of dynamically formed sources in the nucleus of M31 is similar to that of globular cluster sources at the faint end but differs at the bright end, with the M31 nucleus hosting significantly fewer bright sources. The luminosity function of LMXBs in young galaxies has a flatter slope than in older galaxies, i.e. younger galaxies tend to host more bright sources. We also found a correlation of the specific frequency of LMXBs (per unit stellar mass) with the age of the host galaxy and its globular cluster content, that older galaxies having more numerous source populations.

The difference of the luminosity functions of globular cluster and field X-ray binaries presents a challenge for the scenario that all the LMXBs were formed in GCs, and later expelled to the field due to dynamical interactions or the globular cluster destruction. The deficit of faint X-ray sources in globular clusters may be explained as a result of a larger fraction of helium-accreting X-ray binaries in them, produced in the collisions of neutron stars with red giants. Due to the larger ionization temperature of helium, the helium-accreting systems become transient sources at low luminosities with ~ 20 times higher critical mass accretion rate. Low-mass X-ray binaries in globular clusters and in the nucleus of M31 have similar dynamical formation histories. However, ~ 10 - 20 times higher stellar velocity dispersion in the galactic nuclei modifies the relative contributions of different dynamical formation channels, making the tidal captures of low mass stars ($< 0.3M_\odot$) the dominant one. The flatter XLFs in younger galaxies reflect the different properties of the X-ray binary populations in younger galaxies, characterized by a different mass distribution of the donor stars and different distributions of the binary system orbital parameters.

5 Conclusions

The correlation of the specific frequency of LMXBs with the characteristic age of the host galaxy is a result of the intrinsic age dependence of the numbers of X-ray binaries combined with the richer globular cluster populations in older galaxies, resulting in higher contribution of sources dynamically formed in globular clusters. This dependence explains a part of the scatter observed in the scaling relations for low-mass X-ray binaries.

In addition, this investigation produced high quality luminosity distributions of low-mass X-ray binaries in different astrophysical environments. These results will facilitate quantitative comparison with theoretical predictions and provide input for verification of population synthesis models.

Bibliography

- Angelini, L., Loewenstein, M., & Mushotzky, R. F. 2001, *ApJ*, 557, L35
- Annibali, F., Bressan, A., Rampazzo, R., Zeilinger, W. W., & Danese, L. 2007, *A&A*, 463, 455
- Bastian, N. 2008, *MNRAS*, 390, 759
- Bell, E. F. & de Jong, R. S. 2001, *ApJ*, 550, 212
- Bogdán, Á. & Gilfanov, M. 2010a, *A&A*, 512, A16+
- . 2010b, *MNRAS*, 405, 209
- Bordas, P., Kuulkers, E., Alfonso-Garzón, J., et al. 2010, *The Astronomer's Telegram*, 2919, 1
- Boroson, B., Kim, D.-W., & Fabbiano, G. 2011, *ApJ*, 729, 12
- Brassington, N. J., Fabbiano, G., Kim, D., et al. 2008, *ApJS*, 179, 142
- . 2009, *ApJS*, 181, 605
- Buta, R. & McCall, M. L. 2003, *AJ*, 125, 1150
- Buta, R. J. & McCall, M. L. 1983, *MNRAS*, 205, 131
- Caldwell, N., Rose, J. A., & Concannon, K. D. 2003, *AJ*, 125, 2891
- Cantiello, M., Blakeslee, J. P., & Raimondo, G. 2007, *ApJ*, 668, 209
- Chandar, R., Ford, H. C., & Tsvetanov, Z. 2001, *AJ*, 122, 1330
- Clark, G. W. 1975, *ApJ*, 199, L143
- Davies, R. L., Kuntschner, H., Emsellem, E., et al. 2001, *ApJ*, 548, L33
- de Vaucouleurs, G. 1948, *Annales d'Astrophysique*, 11, 247
- de Vaucouleurs, G., de Vaucouleurs, A., Corwin, Jr., H. G., et al. 1991, *Third Reference Catalogue of Bright Galaxies* (Springer)
- Denicoló, G., Terlevich, R., Terlevich, E., Forbes, D. A., & Terlevich, A. 2005, *MNRAS*, 358, 813

Bibliography

- Dickey, J. M. & Lockman, F. J. 1990, *ARA&A*, 28, 215
- Dirsch, B. 1996, Master's thesis, Master Thesis, University of Bonn (1996)
- Dirsch, B., Schuberth, Y., & Richtler, T. 2005, *A&A*, 433, 43
- Dubus, G., Lasota, J.-P., Hameury, J.-M., & Charles, P. 1999, *MNRAS*, 303, 139
- Fabian, A. C., Pringle, J. E., & Rees, M. J. 1975, *MNRAS*, 172, 15P
- Fall, S. M. & Zhang, Q. 2001, *ApJ*, 561, 751
- Ferrarese, L., Mould, J. R., Stetson, P. B., et al. 2007, *ApJ*, 654, 186
- Fingerhut, R. L., McCall, M. L., De Robertis, M., et al. 2003, *ApJ*, 587, 672
- Forbes, D. A. 1996, *AJ*, 112, 954
- Forbes, D. A., Georgakakis, A. E., & Brodie, J. P. 2001, *MNRAS*, 325, 1431
- Forbes, D. A., Grillmair, C. J., Williger, G. M., Elson, R. A. W., & Brodie, J. P. 1998, *MNRAS*, 293, 325
- Fragos, T., Kalogera, V., Belczynski, K., et al. 2008, *ApJ*, 683, 346
- Freedman, W. L., Hughes, S. M., Madore, B. F., et al. 1994, *ApJ*, 427, 628
- Gallagher, J. S., Garnavich, P. M., Caldwell, N., et al. 2008, *ApJ*, 685, 752
- Georgakakis, A., Nandra, K., Laird, E. S., Aird, J., & Trichas, M. 2008, *MNRAS*, 388, 1205
- Gilfanov, M. 2004, *MNRAS*, 349, 146
- Grimm, H.-J., Gilfanov, M., & Sunyaev, R. 2002, *A&A*, 391, 923
- . 2003, *MNRAS*, 339, 793
- Harris, W. E. 1991, *ARA&A*, 29, 543
- . 1996, *AJ*, 112, 1487
- Harris, W. E. 2001, in *Saas-Fee Advanced Course 28: Star Clusters*, ed. L. Labhardt & B. Binggeli, 223–+
- Heinke, C. O., Altamirano, D., Cohn, H. N., et al. 2010, *ApJ*, 714, 894
- Hills, J. G. 1976, *MNRAS*, 175, 1P
- Humphrey, P. J. 2009, *ApJ*, 690, 512
- Humphrey, P. J. & Buote, D. A. 2008, *ApJ*, 689, 983

- Irwin, J. A. 2005, *ApJ*, 631, 511
- Jarrett, T. H., Chester, T., Cutri, R., Schneider, S. E., & Huchra, J. P. 2003, *AJ*, 125, 525
- Jordán, A., McLaughlin, D. E., Côté, P., et al. 2007a, *ApJS*, 171, 101
- Jordán, A., Sivakoff, G. R., McLaughlin, D. E., et al. 2007b, *ApJ*, 671, L117
- . 2011, in preparation
- Juett, A. M. 2005, *ApJ*, 621, L25
- Kim, D., Fabbiano, G., Brassington, N. J., et al. 2009, *ApJ*, 703, 829
- Kim, D.-W. & Fabbiano, G. 2010, *ApJ*, 721, 1523
- Kim, M., Wilkes, B. J., Kim, D.-W., et al. 2007, *ApJ*, 659, 29
- Kissler-Patig, M., Richtler, T., & Hilker, M. 1996, *A&A*, 308, 704
- Kissler-Patig, M., Richtler, T., Storm, J., & della Valle, M. 1997, *A&A*, 327, 503
- Kraft, R. P., Nolan, L. A., Ponman, T. J., Jones, C., & Raychaudhury, S. 2005, *ApJ*, 625, 785
- Kundu, A., Maccarone, T. J., & Zepf, S. E. 2002, *ApJ*, 574, L5
- . 2007, *ApJ*, 662, 525
- Kundu, A. & Whitmore, B. C. 2001, *AJ*, 121, 2950
- Kuntschner, H., Lucey, J. R., Smith, R. J., Hudson, M. J., & Davies, R. L. 2001, *MNRAS*, 323, 615
- Lehmer, B. D., Brandt, W. N., Alexander, D. M., et al. 2007, *ApJ*, 657, 681
- Minniti, D., Rejkuba, M., Funes, J. G., & Akiyama, S. 2004, *ApJ*, 600, 716
- Moretti, A., Campana, S., Lazzati, D., & Tagliaferri, G. 2003, *ApJ*, 588, 696
- Paczyński, B. 1971, *ARA&A*, 9, 183
- Peacock, M. B., Maccarone, T. J., Knigge, C., et al. 2010, *MNRAS*, 402, 803
- Peng, E. W., Jordán, A., Côté, P., et al. 2008, *ApJ*, 681, 197
- Perelmuter, J.-M., Brodie, J. P., & Huchra, J. P. 1995, *AJ*, 110, 620
- Postnov, K. A. & Kuranov, A. G. 2005, *Astronomy Letters*, 31, 7
- Proctor, R. N., Forbes, D. A., Forestell, A., & Gebhardt, K. 2005, *MNRAS*, 362, 857

Bibliography

- Pu, S. B., Saglia, R. P., Fabricius, M. H., et al. 2010, *A&A*, 516, A4+
- Rembold, S. B., Pastoriza, M. G., & Bruzual, G. 2005, *A&A*, 436, 57
- Rhode, K. L. & Zepf, S. E. 2004, *AJ*, 127, 302
- Sánchez-Blázquez, P., Gorgas, J., Cardiel, N., & González, J. J. 2006, *A&A*, 457, 809
- Sarazin, C. L., Kundu, A., Irwin, J. A., et al. 2003, *ApJ*, 595, 743
- Schroder, L. L., Brodie, J. P., Kissler-Patig, M., Huchra, J. P., & Phillips, A. C. 2002, *AJ*, 123, 2473
- Shtykovskiy, P. & Gilfanov, M. 2005, *MNRAS*, 362, 879
- Sikkema, G., Peletier, R. F., Carter, D., Valentijn, E. A., & Balcells, M. 2006, *A&A*, 458, 53
- Sivakoff, G. R., Jordán, A., Sarazin, C. L., et al. 2007, *ApJ*, 660, 1246
- Skrutskie, M. F., Cutri, R. M., Stiening, R., et al. 2006, *AJ*, 131, 1163
- Spitler, L. R., Forbes, D. A., Strader, J., Brodie, J. P., & Gallagher, J. S. 2008, *MNRAS*, 385, 361
- Stanek, K. Z. & Garnavich, P. M. 1998, *ApJ*, 503, L131+
- Terlevich, A. I. & Forbes, D. A. 2002, *MNRAS*, 330, 547
- Thomas, D., Maraston, C., Bender, R., & Mendes de Oliveira, C. 2005, *ApJ*, 621, 673
- Tonry, J. L., Dressler, A., Blakeslee, J. P., et al. 2001, *ApJ*, 546, 681
- Trager, S. C., Faber, S. M., Worthey, G., & González, J. J. 2000, *AJ*, 119, 1645
- van den Heuvel, E. P. J. 1992, in *X-Ray Binaries and the Formation of Binary and Millisecond Radio Pulsars*, 233–256
- Verbunt, F. 1987, *ApJ*, 312, L23
- Verbunt, F. & van den Heuvel, E. P. J. 1995, in *X-ray Binaries*, ed. W. H. G. Lewin, J. van Paradijs, & E. P. J. van den Heuvel, 457–494
- Voss, R. & Gilfanov, M. 2006, *A&A*, 447, 71
- . 2007a, *A&A*, 468, 49
- . 2007b, *MNRAS*, 380, 1685
- Voss, R., Gilfanov, M., Sivakoff, G. R., et al. 2009, *ApJ*, 701, 471

White, N. E. & Angelini, L. 2001, ApJ, 561, L101

White, III, R. E., Sarazin, C. L., & Kulkarni, S. R. 2002, ApJ, 571, L23

Woodley, K. A., Raychaudhury, S., Kraft, R. P., et al. 2008, ApJ, 682, 199

Zhang, Z., Gilfanov, M., Voss, R., et al. 2011, A&A, 533, A33+

Acknowledgements

I appreciate the four years time working in the high energy group at MPA. Thank Prof. Rashid Sunyaev offering me the chance.

My deepest appreciation goes to my supervisor Dr. Marat Gilfanov, that he has spent so much effort to supervise me. Thank his support, patience and trust.

I wish to thank Rasmus Voss for helping me so much with programming. Also thank his code to calculate the luminosity of X-ray point source and the *Chandra* detection sensitivity.

I appreciate Akós Bogdán. I have got a lot of fun and support from him. Thank him making me feel excellent.

Thank Michael Fink, Stefano Mineo, Andrew Cooper, Diederik Kruijssen, Alexander Kolodzig, Pablo Cassatella and Quentin for their sincere friendship and help.

I have met so many nice Chinese friends in Munich. Without them life would be much more difficult. I would like to thank Xiaoling, Chen Hui, Zhang Yang, Wang Lan, Guo Qi, Li Dong, Wang Jing, Zhou Jie and Feng Lu for taking me accompany. Thank Wenting, my little friend who has helped me in the last most difficult months.

Thank my Mom, Dad and sister's love. My Mom's dream being an Astronomer has me accomplished (or started). Thanks for their understanding that I was so far from home for such a long time.

Finally I would like to thank Annop Wongwathanarat, for his support all around.

Curriculum Vitae

Name: Zhongli Zhang

Nationality: Chinese

Education

- 2008 - 2012 **Ph.D. Astrophysics**, Max Planck Institute for Astrophysics
Dissertation: The environment dependence of the population of low-mass X-ray binaries in early-type galaxies
Supervisor: Marat Gilfanov, Rashid Sunyaev
- 2005 - 2007 **Ms.c. Astrophysics**, Shanghai Jiao Tong University
Dissertation: Mass and dark matter distributions in galaxy groups with X-ray, radio and multi-photometric data
Supervisor: Haiguang Xu
- 2000 - 2004 **Bs.c. Physics**, Shanghai Jiao Tong University
Dissertation: X-ray point sources in early-type galaxy NGC 1407
Supervisor: Haiguang Xu

Publication (main)

- [1] Zhongli Zhang, Marat Gilfanov, Rasmus Voss, Gregory R. Sivakoff, Ralph P. Kraft, Nicola J. Brassington, Arunav Kundu, Andrés Jordán, & Craig Sarazin, "Luminosity Functions of LMXBs in Different Stellar Environments", 2011, *A&A*, 533, A33+
- [2] Zhongli Zhang, Marat Gilfanov, & Akós Bogdán, "Dependence of the LMXB population on the stellar age", in preparation
- [3] Zhongli Zhang, Haiguang Xu, Yu Wang, Tao An, Yueheng Xu, & Xiang-Ping Wu, "Probing the Mass Distributions in NGC 1407 and Its Associated Group with the X-Ray Imaging Spectroscopic and Optical Photometric and Line-Strength Indices Data", 2007, *ApJ*, 656, 805
- [4] Zhongli Zhang, & Haiguang Xu, "Chandra Observation of Point Sources in the X-Ray Elliptical Galaxy NGC 1407", 2004, *ChJAA*, 4, 221

